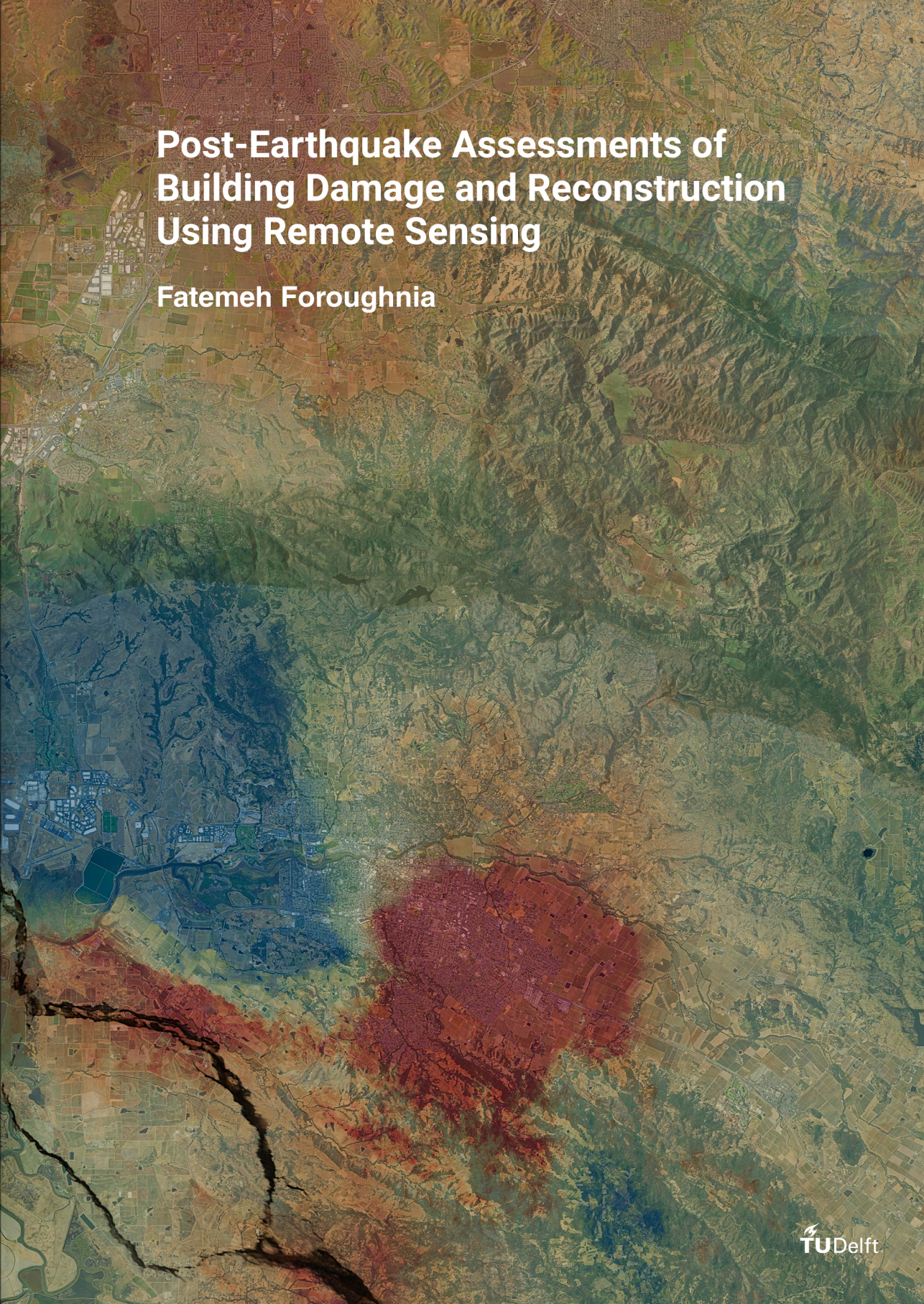

Post-Earthquake Assessments of Building Damage and Reconstruction Using Remote Sensing

Fatemeh Foroughnia

TU Delft

Propositions

accompanying the dissertation

Post-Earthquake Assessments of Building Damage and Reconstruction Using Remote Sensing

by

Fatemeh FOROUGHNIA

1. Moderate earthquake damage is not rare; it is rarely detected. (This thesis)
2. Large-scale post-earthquake field investigations are ineffective without prior Remote Sensing–based screening to guide inspection priorities. (This thesis)
3. Noise becomes a pattern when observed over time. (This thesis)
4. Understanding limitations is more valuable than extending capabilities.
5. Models and people both struggle when transferred without adaptation.
6. Productivity during a PhD is less determined by intelligence than by the ability to tolerate frustration.
7. Emotional resilience is harder to engineer than numerical stability.
8. The most difficult problems in a PhD are rarely technical.
9. Potential is constrained more by beliefs about ability than by ability itself.

These propositions are regarded as opposable and defendable, and have been approved as such by the promotors Dr. G. Gairdina and Prof. dr. K.G. Gavin.

POST-EARTHQUAKE ASSESSMENTS OF BUILDING DAMAGE AND RECONSTRUCTION USING REMOTE SENSING

POST-EARTHQUAKE ASSESSMENTS OF BUILDING DAMAGE AND RECONSTRUCTION USING REMOTE SENSING

Doctoral Dissertation

for the purpose of obtaining the degree of doctor
at Delft University of Technology
by the authority of the Rector Magnificus,
Prof.dr.ir. H. Bijl,
chair of the Board for Doctorates
to be defended publicly on
Monday, 9 November 2026 at 15:00

by

Fatemeh FOROUGHNIA

This dissertation has been approved by the promotors.

Composition of the doctoral committee:

Rector Magnificus,	chairperson
Dr. G. Giardina,	Delft University of Technology, *promotor*
Prof. dr. K.G. Gavin,	Delft University of Technology, *promotor*
Independent members:	
Prof. dr. M. Comes,	Delft University of Technology
Dr. R. Esposito,	Delft University of Technology
Dr. R.C. Lindenbergh,	Delft University of Technology
Prof. dr. J. Ninić,	Durham University, United Kingdom
Dr. V. Novelli,	Cardiff University, United Kingdom
Dr. P.-Y. Declercq,	Royal Belgian Institute of Natural Sciences, Belgium
Prof. dr. ir. S.C. Steele-Dunne,	Delft University of Technology, *reserve member*



Keywords: Earthquake; Building Damage; Building Reconstruction; Remote Sensing; Airborne LiDAR; SAR; MT-InSAR

Printed by: ProefschriftMaken

Cover by: Mohammad Binabaji, based on the ARIA (NASA JPL) displacement map of the 2014 South Napa earthquake.

Copyright © 2026 by F. Foroughnia

ISBN 978-94-6563-037-3

An electronic copy of this dissertation is available at
https://repository.tudelft.nl/.

To my family, for their endless support.

CONTENTS

Summary xi

Samenvatting xiii

Preface xvii

1. Introduction 1
1.1. General background . . . 2
1.2. Remote Sensing in post-earthquake building assessments . . . 3
1.3. Current challenges in Remote Sensing for damage and reconstruction assessment . . . 5
1.4. Objectives and research questions . . . 5
1.5. Methodological approach . . . 6
1.6. Research contributions . . . 9
1.7. Thesis outline . . . 10
References . . . 11

2. Quantitative Assessment of Earthquake-Induced Building Damage at Regional Scale Using LiDAR Data 17
2.1. Introduction . . . 18
2.2. Case study and datasets . . . 20
2.2.1. LiDAR data . . . 21
2.2.2. Building footprint dataset . . . 22
2.2.3. Field data . . . 22
2.3. Methodology . . . 23
2.3.1. Iterative Closest Point (ICP) . . . 24
2.3.2. Drifts and damage classification . . . 25
2.4. Results and discussion . . . 26
2.4.1. Ground-level displacements . . . 26
2.4.2. Building drifts and damage assessment . . . 28
2.5. Validation . . . 29
2.5.1. Ground displacement validation . . . 32
2.5.2. Building damage validation . . . 34
2.6. Conclusion . . . 36
References . . . 38

3. InSAR-Based Framework for Multi-Level Building Damage Classification After Earthquakes 43
3.1. Introduction . . . 44

3.2. Case studies . . . 46
3.2.1. The 2016 Central Italy earthquake events . . . 48
3.2.2. The 2015 Gorkha earthquake . . . 48
3.3. Datasets . . . 48
3.3.1. SAR images . . . 48
3.3.2. Building damage data . . . 49
3.3.3. Site-related datasets . . . 50
3.4. Methodology . . . 50
3.4.1. Data preparation . . . 51
3.4.1.1. InSAR displacement . . . 51
3.4.1.2. InSAR coherence . . . 54
3.4.1.3. Labelled damage and structural data preparation . . . 55
3.4.2. Region-specific learning . . . 55
3.4.2.1. Balanced Random Forest (BRF) classifier . . . 57
3.4.2.2. Overlapping categories . . . 58
3.4.2.3. Performance evaluation . . . 58
3.4.3. Combined learning . . . 59
3.5. Results . . . 60
3.5.1. Performance evaluation of region-specific learning . . . 60
3.5.2. Performance evaluation of combined learning . . . 67
3.6. Discussion . . . 74
3.7. Conclusion . . . 78
References . . . 81

4. Assessment of Post-Earthquake Building Reconstruction Based on MT-InSAR: The Nepal Case Study 87
4.1. Introduction . . . 88
4.2. Methodology . . . 90
4.2.1. Multi-Temporal Synthetic Aperture Radar Interferometry (MT-InSAR) 91
4.2.2. Persistent Scatterer (PS) differential analysis . . . 92
4.3. Case study and datasets . . . 95
4.3.1. Remote Sensing data . . . 95
4.3.2. Field data . . . 96
4.4. Results . . . 98
4.4.1. Grid-level analysis . . . 98
4.4.2. Building-level analysis . . . 100
4.4.3. Validation of building-level results . . . 101
4.5. Discussion . . . 104
4.6. Conclusion . . . 108
References . . . 110

5. Conclusions and recommendations 117
5.1. Answers to research questions . . . 118
5.2. Future research . . . 123

A. Supplementary material 125
A.1. Supplementary material for Chapter 3 126
A.2. Supplementary material for Chapter 4 131

Acknowledgements 135

List of Publications 137

Curriculum Vitæ 139

SUMMARY

Seismic events often cause extensive structural damage, ranging from partial impairment to complete collapse, with significant consequences for human safety and socio-economic stability. Reliable and timely assessment of such impacts is therefore essential during both short-term response and long-term recovery and reconstruction. After an earthquake, timely information on building damage is required to support emergency response and safety-related decisions. In the longer term, insight into reconstruction processes is essential for understanding recovery dynamics and supporting planning and resilience-building efforts. This creates a need for consistent regional building-level assessment across both phases.

Post-earthquake building assessment has traditionally relied on ground-based inspections, which can provide detailed and reliable structural information but are inherently constrained in spatial coverage, speed, and repeatability. These limitations are particularly critical for rapid assessment over large areas and repeated monitoring of long-term reconstruction. As a result, scalable approaches capable of supporting regional-scale assessment over time are required. Post-earthquake building assessment has increasingly relied on Remote Sensing (RS) technologies and data, including optical imagery, airborne Light Detection and Ranging (LiDAR), and spaceborne Synthetic Aperture Radar (SAR) observations. These technologies enable repeated, large-scale observations, supporting both short-term damage assessment and long-term reconstruction monitoring.

In short-term assessments of building damage, most existing RS-based methods rely on coarse damage representations, typically distinguishing between collapsed and non-collapsed buildings. These approaches primarily rely on roof-level observations or derived features from satellite imagery. While effective in identifying severe damage, these approaches fail to capture small-to-moderate damage, which affects much of the building stock and is critical for habitability assessment, repair prioritisation, and loss estimation. Therefore, a key unresolved challenge for short-term regional-scale building damage assessment is the effective integration of structural information to capture intermediate damage levels.

The assessment of long-term reconstruction has predominantly been addressed using optical satellite imagery, often through visual interpretation or bi-temporal change detection. Optical data can provide detailed information on surface conditions and reconstruction activities; however, practical constraints, such as cloud cover, variable illumination, and irregular acquisition schedules, limit the consistency and automation of long-term analyses. As a result, existing approaches struggle to provide systematic, building-level monitoring of reconstruction processes over extended periods and large regions.

The main aim of this thesis is to develop RS-based assessment methods for post-earthquake building damage at the regional scale by integrating RS-driven structural

information sensitive to varying degrees of seismic impact, while also developing RS-based methods for the long-term monitoring of reconstruction processes. This involved: (1) the development of automated RS–based methodologies using LiDAR and SAR data to quantify multi-level building damage beyond simple collapse detection; and (2) the development of a multi-temporal SAR–based differential analysis framework for consistent monitoring of post-earthquake reconstruction processes, overcoming the limitations of optical imagery and enabling building-level reconstruction states to be tracked across large regions and extended time periods.

For short-term assessment, this study developed displacement-driven RS methodologies to integrate physically meaningful structural information into regional-scale post-earthquake damage assessment. Because permanent building displacements directly reflect structural deformation and residual drift under seismic loading, they were adopted as the primary indicators of damage. Airborne LiDAR data acquired before and after earthquakes were aligned using Iterative Closest Point (ICP) registration to derive three-dimensional roof displacements. After removing ground motion effects, residual building displacements were converted into residual drift ratios and classified into damage levels using physically interpretable thresholds, ranging from negligible damage for drift ratios below 0.42% to moderate damage between 1% and 3.2%, and complete damage above 6.1%. In addition, spaceborne SAR data were processed using SAR Interferometry (InSAR) technique to retrieve displacement and coherence information, which were combined with building and site-related characteristics within a Machine Learning (ML) framework based on Random Forest (RF) classification. The LiDAR-based workflow, tested on the 2014 Napa Valley earthquake, showed good agreement with available field observations, supporting its ability to detect intermediate levels of damage. The InSAR-based framework was tested on the 2015 Nepal and 2016 Central Italy events, representing different seismic conditions, building stocks, and damage distributions. It achieved classification performance comparable to that of conventional seismic indicators while providing substantially broader spatial coverage and improved scalability for rapid post-event assessment.

For long-term assessment, the study developed a multi-temporal SAR-based framework for automated monitoring of post-earthquake reconstruction, building on the principle that changes in building stability are reflected in the temporal behaviour of radar scatterers. Time-series SAR data were processed using Multi-Temporal InSAR (MT-InSAR) to identify building-associated Persistent Scatterers (PSs) based on amplitude stability and temporal coherence. A two-stage differential analysis at the regional grid and building levels was then applied to detect systematic changes in scatterer stability associated with collapse, demolition, construction, and reconstruction. The framework was applied to post-earthquake reconstruction in Nepal following the 2015 Gorkha event, where it successfully revealed spatial patterns and temporal trajectories of reconstruction and showed strong agreement with field reconnaissance observations.

Together, these contributions provide complementary RS-based methodologies for regional-scale building assessment, spanning short-term post-earthquake damage assessment and long-term reconstruction monitoring. By advancing LiDAR-, InSAR-, and ML-based automated workflows, this work enables more efficient and scalable regional-scale assessments of multi-level building damage and post-earthquake reconstruction than conventional field-based approaches.

SAMENVATTING

Seismische gebeurtenissen veroorzaken vaak aanzienlijke structurele schade, variërend van gedeeltelijke beschadiging tot volledige instorting, met ingrijpende gevolgen voor de menselijke veiligheid en de sociaal-economische stabiliteit. Een betrouwbare en tijdige beoordeling van dergelijke gevolgen is daarom essentieel,zowel voor de kortetermijnrespons als voor herstel en wederopbouw op lange termijn. Na een aardbeving is tijdige informatie over gebouwschade noodzakelijk om noodhulp en veiligheidsgerelateerde besluitvorming te ondersteunen. Op langere termijn is inzicht in wederopbouwprocessen essentieel voor het begrijpen van hersteldynamieken en het ondersteunen van planning en maatregelen ter versterking van de weerbaarheid. Hierdoor ontstaat behoefte aan een consistente regionale beoordeling op gebouwniveau in beide fasen.

De beoordeling van gebouwschade na aardbevingen is traditioneel gebaseerd op inspecties ter plaatse. Deze kunnen gedetailleerde en betrouwbare structurele informatie opleveren, maar zijn inherent beperkt wat betreft de ruimtelijke dekking, de snelheid en de herhaalbaarheid. Deze beperkingen zijn met name kritisch voor snelle beoordelingen over grote gebieden en herhaalde monitoring van langetermijnprocessen van wederopbouw. Daarom zijn schaalbare benaderingen nodig die het mogelijk maken om regionale beoordelingen door de tijd heen uit te voeren. De beoordeling van gebouwschade na aardbevingen is steeds meer gebaseerd op Remote Sensing (RS)-technologieën en -gegevens, waaronder optische beeldvorming, LiDAR en satellietwaarnemingen met Synthetic Aperture Radar (SAR). Deze technologieën maken herhaalde waarnemingen op grote schaal mogelijk en ondersteunen daarmee zowel de kortetermijnbeoordeling van schade als de langetermijnmonitoring van de wederopbouw.

Bij kortetermijnbeoordelingen van gebouwschade maken de meeste bestaande RS-gebaseerde methoden gebruik van grove schadeclassificaties, waarbij doorgaans onderscheid wordt gemaakt tussen ingestorte en niet-ingestorte gebouwen. Deze benaderingen zijn voornamelijk gebaseerd op waarnemingen op dakniveau of op kenmerken die zijn afgeleid uit satellietbeelden. Hoewel deze methoden effectief zijn voor het identificeren van ernstige schade, slagen ze er niet in om lichte tot matige schade vast te leggen. Dergelijke schade treft een aanzienlijk deel van de gebouwenvoorraad en is cruciaal voor de beoordeling van de bewoonbaarheid, de prioritering van herstelmaatregelen en de raming van de verliezen. Een belangrijke, nog onopgeloste uitdaging voor de kortetermijnbeoordeling van gebouwschade op regionale schaal is daarom de effectieve integratie van structurele informatie om intermediaire schadeniveaus vast te kunnen stellen.

De beoordeling van langetermijnwederopbouw is voornamelijk uitgevoerd met behulp van optische satellietbeelden, vaak door middel van visuele interpretatie of bitemporele veranderingsdetectie. Optische gegevens kunnen gedetailleerde informatie verschaffen over de staat van de oppervlakte en over wederopbouwactiviteiten. Praktische beperkingen, zoals bewolking, variabele belichtingsomstandigheden en onregelmatige acquisitie-

schema's, beperken echter de consistentie en automatisering van langetermijnanalyses. Hierdoor zijn bestaande benaderingen onvoldoende in staat om wederopbouwprocessen systematisch op gebouwniveau te monitoren over langere perioden en in grote regio's.

Het hoofddoel van dit proefschrift is het ontwikkelen van RS-gebaseerde beoordelingsmethoden voor gebouwschade na aardbevingen op regionale schaal, door RS-afgeleide structurele informatie te integreren die gevoelig is voor verschillende niveaus van seismische impact, en tegelijkertijd RS-gebaseerde methoden te ontwikkelen voor de langetermijnmonitoring van wederopbouwprocessen. Dit omvatte: (1) de ontwikkeling van geautomatiseerde RS-gebaseerde methodologieën met behulp van LiDAR- en SAR-gegevens om gebouwschade op meerdere niveaus te kwantificeren en daarmee verder te gaan dan eenvoudige instortingsdetectie; en (2) de ontwikkeling van een multitemporeel SAR-gebaseerd differentieel analysekader voor consistente monitoring van wederopbouwprocessen na aardbevingen, waarmee de beperkingen van optische beeldvorming worden ondervangen en wederopbouwstatussen op gebouwniveau over grote regio's en langere tijdsperioden kunnen worden gevolgd.

Voor de kortetermijnbeoordeling ontwikkelde deze studie verplaatsingsgebaseerde RS-methodologieën om fysisch betekenisvolle structurele informatie te integreren in regionale beoordelingen van gebouwschade na aardbevingen. Omdat permanente gebouwverplaatsingen een directe weerspiegeling vormen van structurele vervorming en restdrift onder seismische belasting, werden deze gebruikt als primaire schade-indicatoren. Airborne LiDAR-gegevens die vóór en na aardbevingen waren verzameld, werden uitgelijnd met behulp van Iterative Closest Point (ICP)-registratie om driedimensionale dakverplaatsingen af te leiden. Na correctie voor de effecten van grondbeweging werden residuele gebouwverplaatsingen omgezet in residuele driftverhoudingen en met behulp van fysisch interpreteerbare drempelwaarden geclassificeerd in schadeniveaus, variërend van verwaarloosbare schade bij driftverhoudingen onder 0,42% tot matige schade tussen 1% en 3,2%, en volledige schade boven 6,1%. Daarnaast werden satellietgebaseerde SAR-gegevens verwerkt met behulp van InSAR-technieken om informatie over verplaatsing en coherentie te verkrijgen. Deze informatie werd gecombineerd met gebouw- en locatiegerelateerde kenmerken binnen een machine-learningkader gebaseerd op Random Forest (RF)-classificatie. De LiDAR-gebaseerde workflow, getest op de aardbeving in Napa Valley in 2014, vertoonde een goede overeenkomst met beschikbare veldwaarnemingen, wat het vermogen van de methode ondersteunt om intermediaire schadeniveaus te detecteren. Het InSAR-gebaseerde kader werd getest op de aardbevingen in Nepal in 2015 en in Centraal-Italië in 2016, die verschillende seismische omstandigheden, gebouwenbestanden en schadeverdelingen vertegenwoordigen. Het behaalde classificatieprestaties die vergelijkbaar waren met die van conventionele seismische indicatoren, terwijl het tegelijkertijd een aanzienlijk grotere ruimtelijke dekking en betere schaalbaarheid bood voor snelle beoordelingen na een aardbeving.

Voor de langetermijnbeoordeling ontwikkelde deze studie een multitemporeel SAR-gebaseerd kader voor de geautomatiseerde monitoring van wederopbouw na aardbevingen, gebaseerd op het principe dat veranderingen in de stabiliteit van gebouwen zich weerspiegelen in het temporele gedrag van radarscatterers. SAR-tijdreeksgegevens werden verwerkt met behulp van Multi-Temporal InSAR (MT-InSAR) om gebouwgerelateerde Persistent Scatterers (PS's) te identificeren op basis van amplitudestabiliteit en temporele

coherentie. Vervolgens werd een tweefasige differentiële analyse op regionaal raster- en gebouwniveau toegepast om systematische veranderingen in de stabiliteit van scatterers te detecteren die samenhangen met instorting, sloop, bouw en wederopbouw. Het kader werd toegepast op de wederopbouw in Nepal na de Gorkha-aardbeving van 2015, waarbij het met succes ruimtelijke patronen en temporele trajecten van de wederopbouw in kaart bracht en een sterke overeenkomst vertoonde met de veldwaarnemingen.

Gezamenlijk bieden deze bijdragen complementaire RS-gebaseerde methodologieën voor regionale beoordeling van gebouwen, die zowel de kortetermijnbeoordeling van gebouwschade na aardbevingen als de langetermijnmonitoring van de wederopbouw omvatten. Door geautomatiseerde workflows op basis van LiDAR, InSAR en machine learning verder te ontwikkelen, maakt dit onderzoek efficiëntere en beter schaalbare regionale beoordelingen van gebouwschade op meerdere niveaus en van wederopbouw na aardbevingen mogelijk dan conventionele veldgebaseerde benaderingen.

PREFACE

This dissertation presents the research I carried out between June 2021 and November 2025 at the Department of Geoscience and Engineering, Delft University of Technology. It focuses on utilising Earth Observation data from spaceborne satellites to study earthquakes, a topic that combines my long-standing fascination with Remote Sensing and my desire to contribute to understanding natural hazards.

My journey began during my bachelor's in Geomatics Engineering, where I first discovered Remote sensing and fell in love with the idea of observing the Earth without ever touching it. The mystery of radar and SAR data drew me in further during my master's program, when I worked on ground displacement analysis using SAR technology. TU Delft provided the ideal environment to deepen that curiosity and continue learning about SAR and Earth observation, while fostering growth as a researcher.

Working on SAR for earthquakes was both challenging and exciting. Through this work, I developed tools to evaluate the impact of earthquakes on buildings, practical outcomes I hope others will find useful.

This PhD journey was a true rollercoaster of learning and resilience. Living far from home, facing serious health challenges, witnessing the impact of wars on my homeland, and a long digital blackout in my country were among the most difficult experiences I faced along the way, but I was never alone. The support of my supervisors, colleagues, and my dear family and friends made everything possible. I am deeply grateful to everyone who was part of this journey.

Delft, March 2026
Fatemeh Foroughnia

List of Figures

1.1. Overview of the methodological structure of the thesis and the respective roles of the developed approaches in short-term damage assessment and long-term reconstruction monitoring. 7

2.1. Case study area, showing the regions covered by pre- and post-event LiDAR data. Red lines indicate fault ruptures [33]. The black polygons refer to building footprints, obtained from OpenStreetMap (OSM) [34] data layer and the Napa municipality [35]. 21
2.2. Distribution of yellow- and red-tagged buildings in the region of interest. . . 23
2.3. Flowchart of the proposed approach. 24
2.4. LiDAR-derived ground displacement maps in (a) X, (c) Y, and (e) Z directions. Figures (b), (d) and (f) show the corresponding maps where false correspondence pairs were removed (Section 2.3). 27
2.5. An example of the distribution of building roof points for (a) before and (b) after the ICP registration. Figures (c) and (d) are close-up views of before and after the ICP registration for one of the roof corners, shown by black rectangles in (a) and (b). 29
2.6. An example of a two-dimensional map of building roof Y displacements. Displacements of the ground points within a 4-m buffer around the buildings were used to estimate the residual building displacements. 30
2.7. Distribution of residual building displacements in (a) X and (b) Y directions for all buildings in the area of interest. The residual building displacements were obtained by subtracting the average ground displacements within a buffer of 4 m around each building. 30
2.8. Building damage map. Building damage levels are based on the residual drift ratios derived from LiDAR displacement measurements. 31
2.9. Distribution of building damage levels in the region of interest. 31
2.10. (a) In-situ right-lateral displacements along trace A, showing the maximum measured slip in the selected sites, rounded to the nearest cm [18] and (b) cross-sections along trace A. 32
2.11. Spatial profile of ground displacements along the cross-section number 10 shown in Figure 2.10b. The black dashed line indicates the fault rupture location. 33
2.12. Distribution of the 38 yellow-tagged buildings in the region of interest. . . . 35

3.1. Study areas and the distribution of building damage data for the (a) Central Italy and (b) Gorkha, Nepal earthquake events. Damge grades: DG0–DG1, No Damage; DG2–DG3, Moderate Damage; DG4–DG5, Severe Damage classes. 47

3.2. Flowchart of the proposed methodology. 52
3.3. Distribution of damage classes across different building typologies for (a) Amatrice, (b) Norcia, and (c) Nepal. 56
3.4. Comparison of metric scores for each damage class across (a) Amatrice, (b) Norcia, and (c) Nepal, with a separate model trained for each region. The square within each bar indicates the average performance over twenty tests, and the vertical error bars represent the standard deviation for each metric. The models were trained using InSAR-derived, site-related, and building features, employing hyperparameter tuning through nested cross-validation, combined with an One-vs-One (OvO) strategy and a Balanced Random Forest (BRF) classifier. 61
3.5. Comparison of average model performance across the three regions. For each region, the bars show the mean weighted Precision, Recall, and F1-Score (weighted by class sample sizes across all test iterations), along with Overall Accuracy (OA) and Kappa, both averaged across iterations. All metrics were computed using building, site-related, and InSAR-derived features, employing an OvO strategy and a BRF classifier. 63
3.6. Confusion matrices resulted from the best-performing model of region-specific learning for (a) Amatrice, (b) Norcia, and (c) Nepal. Rows represent the true damage classes, and columns represent the predicted damage classes. Diagonal cells indicate correctly classified samples, while off-diagonal cells indicate misclassifications between damage classes. Cell values show the number of samples assigned to each true–predicted class combination. 64
3.7. Feature importance maps resulted from the best-performing model in the region-specific learning for (a) Amatrice, (b) Norcia, and (c) Nepal. Each bar shows the importance scores of features used in the training process. 65
3.8. Comparison of overall metric scores for models trained using building and site features, combined either with conventional intensity/acceleration measures or with InSAR-derived features, for (a) Amatrice, (b) Norcia, and (c) Nepal. All models were developed using a BRF classifier, with hyperparameter optimisation performed through nested cross-validation and an OvO strategy. Recall, precision, and F1 scores are reported as macro-averaged across all classes. For Nepal, the InSAR-derived features include both mainshock and aftershock Line-of-Sight (LOS) displacements and coherence. 68
3.9. Comparison of performance metrics for each damage class obtained from the combined dataset. The square within each bar indicates the average performance over twenty tests, and the vertical error bars represent the standard deviation for each metric. The models were trained using InSAR-derived, site, and building features, with hyperparameter tuning through nested cross-validation, employing an OvO strategy and a BRF classifier. . . 69
3.10. Distribution of predicted and true damage classes obtained from the best-performing combined model for (a) the central Italy and (b) the Gorkha earthquake events 71

3.11. Confusion matrices of the best-performing model using the combined-learning approach, evaluated on (a) the complete combined test dataset, (b) the Central Italy subset, comprising the Amatrice and Norcia test samples, and (c) the Nepal test subset. All panels correspond to predictions from the same best-performing combined model. Rows represent the true damage classes, and columns represent the predicted damage classes. Diagonal cells indicate correctly classified samples, while off-diagonal cells indicate misclassifications between damage classes. Cell values show the number of samples assigned to each true–predicted class combination. 72
3.12. Feature importance map resulted from the best-performing model trained on the combined dataset. 73

4.1. Schematic representation of the PS differential analysis at grid and building levels. 92
4.2. Examples of grid-level differential analysis. In Example 1, 50% of points have disappeared in a denser grid cell due to reconstruction years after the earthquake. Example 2 shows an 80% point loss in Grid 1 compared to a 100% loss in Grid 2. In Example 3, 20% of points in Grid 1 and 80% in Grid 2 have disappeared. The analysis indicates greater changes in the denser Grid 1 for Example 1, while in Examples 2 and 3, the differential changes depend on the degree of point loss in each grid. 94
4.3. A view of the region of interest, highlighting the locations where field pictures were taken. The close-up image on the right-hand side of the figure shows the distribution of these field pictures within Kathmandu. Google satellite imagery is used as a background layer. 96
4.4. Temporal distribution of Cosmo–SkyMed (CSK) data images for the different time series before and after the earthquake. The number of PSs detected with Temporal Coherence higher than 0.7 is specified for each pair. 97
4.5. Results of PS differential analysis on the regional scale in Nepal from (a) Pair 1, (b) Pair 2, and (c) Pair 3. Different colour scales were used to highlight the concentration of changed areas on the maps separately. The black rectangles show areas with a high concentration of grid cells with extensive changes, linked with two main affected areas in 2015, one in Kathmandu and one in Bhaktapur. 99
4.6. Building-level PS differential results using Pair 3 across (a) two identified areas: (b) Kathmandu and (c) Bhaktapur. 101
4.7. Accuracy of the building-level results: (a) histogram showing the percentage of positive correlations between field pictures and buildings with over 50% changes per pair and (b) line graph showing the percentage of positive correlations between field pictures and buildings with more than 50% changes, based on varying numbers of post-event images for Kathmandu and Bhaktapur. 102
4.8. Distribution of the detected buildings, which were in agreement with field pictures for areas (a) Kathmandu and (b) Bhaktapur. 103

4.9. Examples of surveyed buildings from the 2022 EEFIT mission that correspond to buildings with over 50% change. In (a), Figures A, G, and H correspond to demolished buildings; B, C, and E show reconstructed buildings; and D and F show buildings under construction. (b) An example of a reconstructed building in Kathmandu, showing the building footprint, corresponding field pictures, and the percentage of PS loss. 104

A.1. LOS Displacement maps derived from InSAR processing using the GAMMA software within the ASF platform [1], after atmospheric correction. Panels (a) and (b) correspond to the Amatrice event, (c) and (d) to the Norcia event, and (e) and (f) to the Nepal earthquake. For each region, ascending and descending tracks are shown in the left and right columns, respectively. . . . 127
A.2. Pairwise relationships among key structural, site, and InSAR-derived features for the Amatrice dataset. Diagonal panels show the distribution of each individual feature, while off-diagonal panels show the pairwise relationships between features. Each panel is colour-coded by building damage level (No damage, Moderate, Severe). The numerical labels on the axes correspond to the following features: 1– Number of storeys, 2– Age, 3– Floor surface, 4– Slope, 5– Vs30, 6– Distance to the epicentre, 7– LOS descending, 8– LOS ascending, 9– Coherence descending, 10– Coherence ascending. . . 128
A.3. Pairwise relationships among key structural, site, and InSAR-derived features for the Norcia dataset. Diagonal panels show the distribution of each individual feature, while off-diagonal panels show the pairwise relationships between features. Each panel is colour-coded by building damage level (No damage, Moderate, Severe). The numerical labels on the axes correspond to the following features: 1– Number of storeys, 2– Age, 3– Floor surface, 4– Slope, 5– Vs30, 6– Distance to the epicentre, 7– LOS descending, 8– LOS ascending, 9– Coherence descending, 10– Coherence ascending. 129
A.4. Pairwise relationships among key structural, site, and InSAR-derived features for the Nepal dataset. Diagonal panels show the distribution of each individual feature, while off-diagonal panels show the pairwise relationships between features. Each panel is colour-coded by building damage level (No damage, Moderate, Severe). The numerical labels on the axes correspond to the following features: 1– Number of storeys, 2– Age, 3– Floor surface, 4– Slope, 5– Vs30, 6– Distance to the epicentre, 7– Main-shock LOS descending, 8– Main-shock LOS ascending, 9- After-shock LOS descending, 10- After-shock LOS ascending 11– Main-shock coherence descending, 12– Main-shock coherence ascending, 13– After-shock coherence descending, 14– After-shock coherence ascending. 130
A.5. Number of PSs per grid cell based on pre-event data: (a) histogram showing the frequency distribution and (b) box plot showing the variability of PS numbers (pre-event time series) per grid cell. The upper bound of the number of PSs (pre-event time series) used for grid-level analysis is 224. . . 131

A.6. Number of PSs per building footprint from the (a) pre-event and (b) post-event data (Post 3). 132

LIST OF TABLES

1.1. Comparison of the RS approaches adopted in this thesis. Differential LiDAR (Chapter 2) and InSAR (Chapter 3) are applied to short-term earthquake damage assessment, while MT-InSAR (Chapter 4) is applied to long-term reconstruction monitoring. 9

2.1. Offset measurements parallel to the fault rupture along the cross-sections represented in Figure 2.10b. 34

3.1. SAR imagery acquisition information for the earthquake regions shown in Figure 3.1. (M) and (A) refer to the Mainshock and Aftershock events in Gorkha, Nepal, respectively. 49
3.2. The distribution of buildings across damage levels for each study area. . . . 60

A.1. Upper bound values of building area distributions for each pair, used in the building-level analysis. 131
A.2. Number of buildings with over 50% change used for validation, categorised by pair and regions of interest. 132
A.3. Perpendicular and temporal baselines with Doppler Centroid (DC) differences for the time series of Post 2. 133

List of Abbreviations

AdF Adaptive Phase Filter.

ADI Amplitude Dispersion Index.

APS Atmospheric Phase Screen.

ASF Alaska Satellite Facility.

ASI Amplitude Stability Index.

BIM Building Information Modelling.

BRF Balanced Random Forest.

Cal OES California Governor's Office of Emergency Services.

CNNs Convolutional Neural Networks.

CRS Coordinate Reference System.

CSK Cosmo–SkyMed.

DaDO Database of Observed Damage.

DC Doppler Centroid.

DEM Digital Elevation Model.

DPM Damage Proxy Map.

DSM Digital Surface Model.

EEFIT Earthquake Engineering Field Investigation Team.

EERI Earthquake Engineering Research Institute.

EMS-98 European Macroseismic Scale 1998.

ESA European Space Agency.

GACOS Generic Atmospheric Correction Online Service.

GEO–CAN Global Earth Observation Catastrophe Assessment Network.

GIS Geographic Information System.

GPS Global Positioning System.

HAZUS Hazards U.S..

ICP Iterative Closest Point.

InSAR SAR Interferometry.

ITD Iterative Tropospheric Decomposition.

IW Interferometric Wide.

K-NN K-Nearest Neighbour.

LiDAR airborne Light Detection and Ranging.

LOS Line-of-Sight.

ML Machine Learning.

MMI Modified Mercalli Intensity.

MSE Mean Square Error.

MT-InSAR Multi-Temporal InSAR.

Mw moment magnitude.

NSET National Society for Earthquake Technology–Nepal.

OA Overall Accuracy.

OSM OpenStreetMap.

OvO One-vs-One.

PDAL Point Data Abstraction Library.

PGA Peak Ground Acceleration.

PGV Peak Ground Velocity.

PIV Particle Image Velocimetry.

PS Persistent Scatterer.

PSAs Pseudo-Spectral Accelerations.

PSC PS Candidate.

QGIS Quantum Geographic Information System.

RC Reinforced Concrete.

RF Random Forest.

RGB Red–Green–Blue.

RMSE Root Mean Square Error.

RS Remote Sensing.

SAR Synthetic Aperture Radar.

SLC Single Look Complex.

SVD Singular Value Decomposition.

SVMs Support Vector Machines.

TC Temporal Coherence.

TOPSAR Terrain Observation by Progressive Scans SAR.

USGS United States Geological Survey.

VHR Very High-Resolution.

VV Vertical–Vertical polarisation.

ZTD Zenith Total Delay.

1

INTRODUCTION

1.1. GENERAL BACKGROUND

Over the last decades, earthquakes have caused widespread destruction of buildings worldwide, resulting in significant loss of life and substantial economic damage [1]. From 2000 to 2020, earthquakes with magnitudes of 7.0 and above occurred almost every year and caused approximately 700,000 direct and indirect fatalities worldwide [2, 3]. In the early 2020s, several major earthquakes contributed tens of thousands of additional deaths, with reported fatalities reaching approximately 60,000–70,000 within just a few years [4–6].

A central component of earthquake impact assessment is the reliable evaluation of building damage, as a large proportion of earthquake-related casualties and losses result from structural failure and collapse [1, 7, 8]. Because such events can devastate large areas within a very short time, there is a critical need for rapid, regional-scale assessment of building damage to support post-disaster management [9]. In the immediate aftermath, timely information on the extent and distribution of damaged buildings is essential to support short-term response activities, including search-and-rescue operations [10], access restriction, and efficient allocation of resources, while reducing secondary risks associated with unstable structures [10–12]. Beyond the emergency phase, in the long term, systematic building-level assessments remain equally important for recovery and reconstruction, as they enable monitoring of repaired and rebuilt structures, tracking of reconstruction progress across affected regions. Such information can support authorities and recovery planners in making informed policy and resource allocation decisions to restore safe and resilient housing [13].

Traditional approaches to building assessment are typically carried out through on-site inspections [4, 14, 15], where engineers and surveyors examine damaged structures during post-earthquake field reconnaissance missions to classify their level of damage and assess their usability, or determine the extent of reconstruction required [4]. While such inspections can provide detailed and reliable information at the scale of individual buildings, they are inherently time-consuming and labour-intensive, particularly when assessments need to cover large affected regions, and are often limited to accessible areas [16–20]. Moreover, the assignment of damage levels during field inspections relies in part on the judgment and experience of individual inspectors, which can introduce subjectivity and inter-observer variability, particularly in the immediate aftermath of an earthquake, when assessments are conducted under severe time constraints and by personnel with varying levels of experience [21]. Because these assessments directly inform decisions on building safety and usability, uncertainty may lead inspectors to adopt precautionary or conservative classifications to avoid underestimating potential risks to occupants. Differences in inspector experience and judgement may also contribute to variation in classification, which is why standardised criteria and decision-support tools are needed to identify potentially inconsistent postings [22]. These limitations become particularly important in large-scale disasters, where thousands or even millions of buildings may require assessment. For example, following the Nepal earthquake of 2015, remote mountain villages remained inaccessible for weeks, delaying the delivery of both aid and assessments [23]. Consequently, there is a need for objective, reproducible, and spatially scalable approaches that can provide timely building-damage information over large affected areas and complement

conventional field inspections. In this context, rapid assessment refers to the ability to obtain building-damage information over large affected areas more rapidly than is possible through conventional building-by-building field inspection, rather than to a fixed operational processing time following an earthquake.

1.2. REMOTE SENSING IN POST-EARTHQUAKE BUILDING ASSESSMENTS

Remote Sensing (RS) techniques provide a powerful complement to traditional on-site reconnaissance. Through airborne or spaceborne platforms, RS enables systematic and frequent data acquisition over large affected regions, including areas where ground access may be difficult, while providing a relatively cost-effective means of obtaining spatially extensive observations [24–26]. Beyond improved spatial coverage and timeliness, RS also provides a more standardised basis for building assessment, as consistent observations and processing procedures can be applied across large areas of impact. This can reduce the influence of subjective expert judgement and inter-observer variability and improve the consistency and reproducibility of damage assessment. These characteristics make RS suitable for emergency mapping [27], large-scale structural assessment, and long-term monitoring. Over the past decades, this technique has been successfully applied to large-scale assessments, including urban areas where rapid detection is critical for organising emergency measures. Recent technological advances have further improved RS's ability to extract detailed damage information and support post-disaster recovery planning [28].

Existing RS-based methods for earthquake-induced building damage assessment generally rely on post-event classification or multi-temporal change-detection approaches. Classification-based approaches mainly use observations acquired after an event to identify and distinguish damaged from undamaged buildings [29, 30]. Change-detection approaches instead compare observations acquired before and after an earthquake to identify earthquake-induced changes in building characteristics, which can subsequently be associated with different damage levels. Commonly analysed characteristics include shape, referring to the observable geometry of a building or roof object; intensity, referring to the magnitude of the recorded signal at a given image pixel; and texture, referring to the spatial variation and relationships among neighbouring pixel values.

These approaches have been implemented using different RS data sources, primarily optical imagery, Synthetic Aperture Radar (SAR), and airborne Light Detection and Ranging (LiDAR), which are widely used for detecting building-level damage [12, 31–36].

Optical sensors acquire imagery in the visible and near-visible spectrum, producing representations that are broadly similar to human vision. Such data have been widely used for post-earthquake building damage detection via change-detection and classification approaches based on spectral, textural, contextual, and geometrical features [37]. For example, a Convolutional Neural Networks (CNNs) applied to a Very High-Resolution (VHR) QuickBird image enabled the identification of collapsed buildings following the 2010 Haiti earthquake [38]. Pre- and post-event optical imagery has also supported object-based change detection at the building level, where textural and colour

changes, combined with statistical similarity measures, were particularly effective in identifying damaged buildings [33]. In addition, optical imagery has been used to analyse reconstruction processes and urban recovery dynamics [39–41]. While optical data enable intuitive identification of ground features such as buildings [42], optical sensors rely on sunlight and clear-sky conditions [43]. These constraints limit their usefulness for timely post-disaster building assessment [25, 42].

SAR sensors have gained increasing attention in recent years and widespread application in post-earthquake assessment due to their ability to operate under all-weather conditions and during both day and night [25, 42]. The extensive spatial coverage and short revisit times of recent satellite constellations enable repeated observations of heavily affected regions and rapid data acquisition following disasters [12, 44]. Moreover, the availability of open-access SAR data further supports their timely and widespread application for regional-scale post-earthquake assessment [45, 46]. Both classification and change-detection approaches have been applied to SAR observations. Classification approaches have used statistical and textural characteristics of radar imagery, often in combination with Machine Learning (ML) methods. For instance, first- and second-order statistical features extracted from VHR TerraSAR-X imagery have been used to train ML classifiers for distinguishing damaged and intact buildings [47]. Similarly, statistical features derived from ALOS-2/PALSAR-2 imagery have been used with ML algorithms to map and classify damaged buildings [48].

Change-detection approaches using SAR have exploited temporal variations in features such as radar intensity and coherence [49–52]. Coherence is a measure of the stability of scatterers, such as buildings, and is defined by the spatial correlation between two SAR images. A reduction in coherence between pre- and post-event observations represents a loss of correlation and can indicate changes associated with earthquake-induced damage. Changes in these observations can be quantified using ratios, differences, or statistical measures, with thresholding or discriminant analysis subsequently used to distinguish damaged from undamaged areas. Pre-event Sentinel-1 time-series data have been used to forecast expected co-event coherence in the absence of damage, allowing anomalous coherence loss to be identified by comparison with observed co-event data [53]. Sequential coherence images have also been compared using simple and normalised differencing methods [54], and coherence changes have been combined with optical-derived spectral indices to identify damaged urban areas [55]. Although SAR images can be more challenging to interpret visually, numerous studies have successfully used them to detect building damage, ground displacement, and other earthquake-induced impacts [12, 18, 47, 49–52, 56, 57]. Together with the capacity of SAR for repeated observations over large areas under all-weather and day-and-night conditions, these capabilities make it particularly suitable for timely and large-scale post-earthquake assessments.

When available, LiDAR data provide valuable high-resolution information on building conditions, often surpassing the spatial detail offered by SAR. LiDAR systems generate three-dimensional point clouds that represent the Earth's surface with high precision [58]. For earthquake damage assessment, LiDAR has primarily been applied through multi-temporal change detection, in which pre- and post-event observations are compared to identify changes in building geometry. These precise measurements of the

terrain and structures allow the detection of changes in building geometry, roof collapse, or partial damage, primarily through the analysis of Digital Surface Models (DSMs) and height information [16, 58]. However, earthquake-related applications of LiDAR remain relatively limited compared with SAR, primarily due to the limited availability of pre- and post-event LiDAR acquisitions [16].

1.3. CURRENT CHALLENGES IN REMOTE SENSING FOR DAMAGE AND RECONSTRUCTION ASSESSMENT

Despite substantial progress in applying RS for post-earthquake building assessment, current RS-based approaches face several fundamental challenges. First, most existing methods rely primarily on two-dimensional observations of roofs or façades. While these observations are effective in identifying collapsed buildings, they provide only limited insight into slight-to-moderate damage and the underlying structural failure mechanisms. Many forms of damage do not produce clear changes in roof geometry or surface appearance, making them inherently difficult to detect using 2D imagery alone. As a result, current assessment methods often lack quantitative information reflecting the internal structural response of buildings to seismic loading. Damage processes involving internal structural cracks or permanent changes in structural behaviour may not be accompanied by visible surface changes, yet can substantially affect structural safety. The limited ability of existing RS approaches to capture such internal damage mechanisms restricts their effectiveness in identifying moderate and subtle forms of deterioration.

Second, most existing RS-based approaches for long-term reconstruction monitoring rely on manual interpretation or change detection from a small number of optical images acquired at discrete time points. These approaches are subject to several inherent challenges. Reconstruction typically proceeds gradually and unevenly across affected areas, meaning that changes observed between only a few acquisition dates may not reliably distinguish rebuilt structures from those that were never damaged. In addition, reliance on optical imagery introduces constraints related to cloud cover, illumination, and data availability, thereby limiting temporal continuity. Without dense and consistent time-series observations, it becomes difficult to attribute observed changes unambiguously to post-disaster reconstruction rather than to unrelated variations. Consequently, current methods often struggle to provide reliable and systematic information on long-term recovery processes at regional scales.

1.4. OBJECTIVES AND RESEARCH QUESTIONS

This thesis aims to develop regional-scale post-earthquake building assessment methods by using RS–derived structural information for short-term damage evaluation and multi-temporal observations for long-term reconstruction monitoring. In this thesis, regional-scale refers to spatially extensive assessments at approximately the city scale or larger, rather than at the level of several buildings. The term describes the spatial extent of the assessment and does not correspond to a specific administrative region. Specifically, the thesis aims to develop automated methodologies to quantify multi-level building damage beyond simple collapse detection and to systematically identify and

track post-earthquake reconstruction through changes in building-related radar signals. Together, these contributions support a consistent and scalable assessment of building performance from immediate damage to long-term reconstruction.

Accordingly, this thesis specifically addresses the following main research question:

How can RS support regional-scale assessment of earthquake-induced building damage in the short term and monitoring of post-earthquake reconstruction processes in the long term?

This question is addressed through the following sub-questions:

1. How can RS–derived indicators of structural response be used as physically interpretable measures of short-term earthquake damage?
2. How can LiDAR-based observations be used to quantify multi-level building damage at regional scales?
3. How can SAR-based features be employed to improve the detection and classification of multi-level building damage?
4. How can regional-scale damage assessment be achieved using SAR-based information when detailed ground-based seismic data are unavailable?
5. How can time-series SAR observations be systematically used to identify and monitor post-earthquake reconstruction processes?
6. How can RS-based observations support field investigations of post-earthquake building reconstruction at regional scales?

1.5. METHODOLOGICAL APPROACH

This thesis adopts a multi-stage RS–based methodological strategy to assess post-earthquake building conditions across different temporal phases, from short-term damage evaluation to long-term reconstruction monitoring. The methodological choices are guided by the physical relationship between earthquake-induced displacement and building deformation and reconstruction, while accounting for data availability and scalability at regional scales. Their application encompasses different building typologies across the case studies, with the LiDAR-based methodology evaluated specifically on predominantly timber-frame buildings, and the SAR-based methodologies applied to more diverse building stocks. Figure 1.1 provides an overview of the thesis's methodological structure, illustrating how the three developed methodologies address different phases of post-earthquake building assessment.

In the immediate aftermath of an earthquake, building damage is primarily manifested as permanent structural deformations resulting from the building's response to seismic loading. To quantify these effects, this thesis focuses on displacement-based indicators derived from RS observations. Displacement is considered a physically interpretable damage indicator because it represents the actual movement and deformation of a structure during and after earthquake shaking and can therefore be directly related

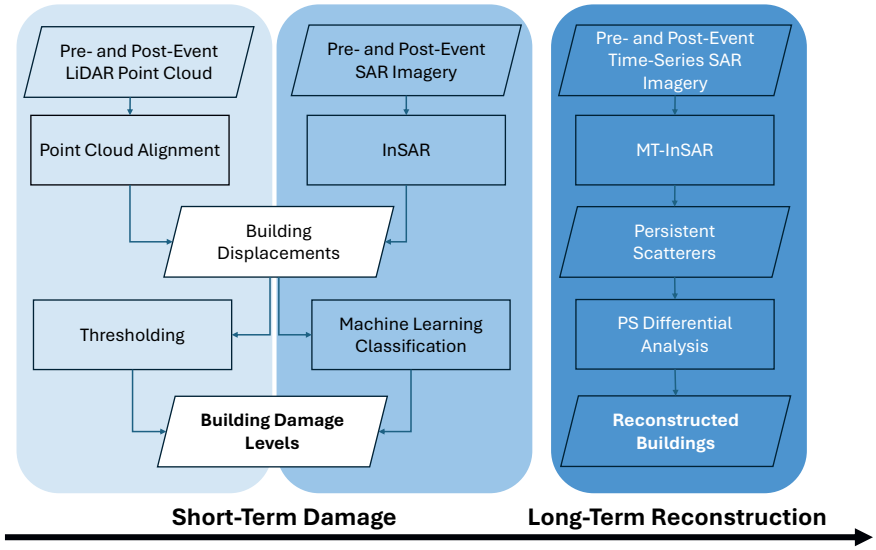

Figure 1.1.: Overview of the methodological structure of the thesis and the respective roles of the developed approaches in short-term damage assessment and long-term reconstruction monitoring.

to changes in its configuration, structural performance, and damage. Unlike purely image-based metrics, displacement-based indicators provide quantitative information on structural response, enabling the identification of damage levels that may not be visually apparent, particularly for slight-to-moderate damage. By integrating remotely observed displacement into post-earthquake assessment workflows, this research addresses the key limitation of existing approaches and establishes a more physically grounded basis for regional-scale damage evaluation.

To achieve this, two complementary displacement-based methodologies are developed. First, differential airborne LiDAR data are used to extract three-dimensional building displacements by comparing pre- and post-event point clouds. These displacements are translated into residual displacements and building-level drift ratios, calculated by normalising the maximum average horizontal residual roof displacement by the LiDAR-derived total building height, enabling quantitative, building-level damage assessment where high-resolution LiDAR data are available. Recognising the limited spatial and temporal availability of LiDAR data, a second methodology based on spaceborne SAR is also introduced to extend displacement-based damage assessment to regional scales. SAR Interferometry (InSAR)–derived displacement and coherence information are combined with structural and site-related features within an ML framework to enable scalable, multi-level (i.e. No damage, Moderate, Severe) damage classification in data-sparse environments. Post-earthquake field-assessed damage data serve as the target labels for model training and evaluation.

The methodological choices, therefore, reflect both the characteristics of the post-earthquake process and practical data considerations. For short-term damage assessment, pre- and post-event LiDAR provides detailed three-dimensional measurements of building deformation, while InSAR provides complementary displacement and coherence information with broader regional coverage. The use of both approaches reflects the limited spatial and temporal availability of pre- and post-event LiDAR data, rather than a preference for InSAR over LiDAR. Where suitable LiDAR data are available, it remains particularly valuable for accurate structural assessment; InSAR extends the approach to larger areas where such data are unavailable.

Long-term post-earthquake reconstruction represents a distinct assessment phase characterised by gradual changes in the built environment rather than immediate structural response. During this phase, building collapse, demolition, reconstruction, and rebuilding modify urban geometry, surface properties, and radar backscattering behaviour over time. These changes are not instantaneous but evolve progressively, making them particularly suitable for analysis using multi-temporal SAR observations. Owing to its capability for frequent, wide-area, and all-weather data acquisition, SAR enables continuous monitoring of reconstruction processes under diverse environmental conditions. Despite these advantages, the potential of SAR time-series data for systematic long-term reconstruction assessment has remained underexploited in existing studies.

To capture these dynamics, the thesis adopts a time-series–based reconstruction monitoring approach using Multi-Temporal InSAR (MT-InSAR). This choice reflects the gradual nature of reconstruction, which requires repeated observations to capture how building conditions evolve over time. Unlike a bi-temporal assessment, MT-InSAR exploits a series of observations to characterise temporal changes in the stability, persistence, and spatial distribution of building-related radar scatterers. These temporal patterns can reflect transitions associated with collapse, demolition, ongoing reconstruction, and completed rebuilding, enabling areas and individual buildings undergoing reconstruction to be identified and monitored over time. The approach is therefore explicitly tailored to the systematic, long-term monitoring of post-earthquake reconstruction.

These methodologies address complementary phases of the post-earthquake assessment timeline, with their main characteristics and respective roles summarised in Table 1.1. Each method addresses a specific phase of the disaster cycle and contributes complementary information relevant to disaster response and reconstruction monitoring. Their selection is primarily guided by the temporal characteristics of these phases: pre- and post-event LiDAR and InSAR observations are suited to capturing abrupt earthquake-induced changes for short-term damage assessment, whereas MT-InSAR exploits time-series observations to capture the gradual changes in building stability associated with long-term reconstruction. Data availability and scalability further influence the practical use of each technique. For example, the limited availability of pre- and post-event LiDAR motivates the complementary use of more widely available satellite SAR observations. Thus, even if all datasets were equally available, the distinction between methods for short-term damage assessment and long-term reconstruction monitoring would remain, although the different sensors could provide complementary information within each phase. Together, the methodologies enable a systematic

Table 1.1.: Comparison of the RS approaches adopted in this thesis. Differential LiDAR (Chapter 2) and InSAR (Chapter 3) are applied to short-term earthquake damage assessment, while MT-InSAR (Chapter 4) is applied to long-term reconstruction monitoring.

Characteristic	**Differential LiDAR**	**InSAR**	**MT-InSAR**
Observation	3D displacement	LOS displacement & coherence	Temporal scatterer stability
Temporal basis	Pre–post	Pre–post	Time series
Change captured	Abrupt	Abrupt	Gradual
Spatial capability	Survey-dependent coverage	Wide-area	Wide-area
Key strength	Detailed & accurate structural deformation	Scalable & frequent observations	Temporal evolution of buildings
Main limitation	Limited pre/post data availability & costly	LOS sensitivity & decorrelation	Requires sufficient observations

assessment of building conditions across different stages of post-earthquake response and reconstruction.

1.6. RESEARCH CONTRIBUTIONS

This thesis presents three methodological contributions that advance regional-scale post-earthquake building assessment and long-term reconstruction monitoring through:

- A displacement-based damage assessment methodology using LiDAR, which integrates three-dimensional point cloud differencing and structural engineering principles to derive physically interpretable indicators of building performance. This methodology establishes residual displacement and drift-based metrics as quantitative proxies for multi-level earthquake damage, enabling reliable identification of slight-to-moderate damage states that are often missed by image-based approaches.

- A scalable InSAR–ML framework for multi-level damage classification, which combines interferometric displacement and coherence measurements with building- and site-related characteristics within a physically interpretable ML classification scheme. By addressing class imbalance and regional variability, this framework demonstrates how satellite-based deformation data can support automated and scalable damage assessment across diverse seismic contexts.

- A multi-temporal SAR-based reconstruction monitoring methodology, which applies a two-stage differential Persistent Scatterer (PS) analysis at regional and building scales to systematically identify areas and individual buildings exhibiting substantial changes associated with post-earthquake reconstruction processes. This methodology establishes a new paradigm for long-term, weather-independent monitoring of post-earthquake reconstruction dynamics using SAR time series.

Together, these contributions demonstrate how LiDAR-, InSAR-, and MT-InSAR–based methodologies can be developed as complementary yet independent tools to address different phases of post-earthquake assessment. By grounding RS analysis in physically meaningful indicators of structural response and reconstruction, this thesis provides a coherent and scalable methodological foundation for quantitative damage evaluation and long-term reconstruction monitoring at regional scales.

1.7. THESIS OUTLINE

Chapter 2 presents a quantitative building damage assessment methodology based on differential LiDAR data. It focuses on damage classification using physically interpretable thresholding criteria, demonstrating the capability of high-resolution three-dimensional LiDAR point clouds to provide reliable indicators of earthquake-induced damage. The methodology is applied to the 2014 Napa Valley earthquake to demonstrate its capability for building-level and regional-scale classification of multiple damage states, highlighting the potential of high-resolution three-dimensional LiDAR data for quantitative post-earthquake damage assessment.

Chapter 3 extends the scope to a broader scale of short-term damage assessment. It introduces an InSAR-based multi-level damage classification framework, validated on the Central Italy (2016) and Gorkha (2015) case studies. It also examines the potential of InSAR measurements as alternatives to conventional seismic indicators, such as Peak Ground Velocity (PGV) and Peak Ground Acceleration (PGA), when ground-based data are limited. This chapter demonstrates whether InSAR displacements can serve as a reliable surrogate for the conventional measures while retaining physical interpretability.

Chapter 4 focuses on the evaluation of the long-term post-earthquake reconstruction process using MT-InSAR analysis. The chapter introduces a two-stage assessment strategy to identify reconstruction dynamics, such as completed reconstruction, ongoing construction, and demolition activities, providing a systematic view of regional-scale building reconstruction processes. The methodology is applied to the Nepal Gorkha earthquake case study to demonstrate its capability for large-scale, long-term reconstruction monitoring and to validate the approach against observed recovery patterns.

Chapter 5 synthesises the findings of the thesis by answering the research questions, discussing limitations and highlighting directions for future research.

REFERENCES

[1] D. Guha-Sapir, R. Below and P. Hoyois. 'EM-DAT: the emergency events database-Université catholique de Louvain (UCL)-CRED'. In: *Retrieved from EM-DAT* (2018).

[2] C. Dollet and P. Guéguen. 'Global occurrence models for human and economic losses due to earthquakes (1967-2018) considering exposed GDP and population'. In: *Natural Hazards* 110.1 (2022), pp. 349–372. DOI: 10.1007/s11069-021-04950-z.

[3] J. Zhao, X. Li and S. Chen. 'Estimation of economic loss and recover process after earthquake base on nighttime light data and time series model'. In: *Reliability Engineering & System Safety* (2025), p. 111244. DOI: 10.1016/j.ress.2025.111244.

[4] M. R. Whitworth, G. Giardina, C. Penney, L. Di Sarno, K. Adams, T. Kijewski-Correa, J. Black, F. Foroughnia, V. Macchiarulo, P. Milillo *et al.* 'Lessons for remote post-earthquake reconnaissance from the 14 August 2021 Haiti earthquake'. In: *Frontiers in Built Environment* (2022), p. 53. DOI: 10.3389/fbuil.2022.873212.

[5] M. Mokhtari, P. Faridi, M. Masoodi and S. M. Ahmadi. 'Perspective chapter: A global view of natural hazards related disasters'. In: *Natural Hazards-New Insights*. IntechOpen, 2023. DOI: 10.5772/intechopen.111582.

[6] A. Laosunthara, K. Krutphong, N. Leelawat, W. Wararuksajja, N. Sukulthanasorn, A. Suppasri, R. Thongthip and C. Chintanapakdee. 'Initial observations and immediate lessons learned from Thailand's response to the 2025 Mandalay earthquake'. In: *International Journal of Disaster Risk Reduction* (2025), p. 105675. DOI: 10.1016/j.ijdrr.2025.105675.

[7] R. Spence and A. Coburn. *Earthquake Protection*. en. 2nd ed. Hoboken, NJ: John Wiley & Sons, Ltd, Sept. 2002. DOI: 10.1002/0470855185.

[8] R. Spence and E. So. *Why do buildings collapse in earthquakes? Building for safety in seismic areas*. John Wiley & Sons, 2021. DOI: 10.1080/13602365.2016.1276094.

[9] S. Mangalathu, H. Sun, C. C. Nweke, Z. Yi and H. V. Burton. 'Classifying earthquake damage to buildings using machine learning'. In: *Earthquake Spectra* 36.1 (2020), pp. 183–208. DOI: 10.1177/8755293019878137.

[10] J. Macabuag, C. Altheim, S. Thorvaldsdottir and D. Perks. 'Damage assessments by international engineers following the Albania earthquake of November 2019'. In: *International Journal of Disaster Risk Reduction* 72 (2022), p. 102822. DOI: 10.1016/j.ijdrr.2022.102822.

[11] M. Al-Rawashdeh, M. Al Nawaiseh, I. Yousef, M. Bisharah, S. Alkhadrawi and H. Al-Bdour. 'Predicting building damage grade by earthquake: A Bayesian optimization-based comparative study of machine learning algorithms'. In: *Asian Journal of Civil Engineering* 25.1 (2024), pp. 253–264. DOI: 10.1007/s42107-023-00771-6.

[12] V. Macchiarulo, G. Giardina, P. Milillo, Y. D. Aktas and M. R. Whitworth. 'Integrating post-event very high resolution SAR imagery and machine learning for building-level earthquake damage assessment'. In: *Bulletin of Earthquake Engineering* (2024), pp. 1–27. DOI: 10.1007/s10518-024-01877-1.

[13] S. Ghaffarian and S. Emtehani. 'Monitoring urban deprived areas with remote sensing and machine learning in case of disaster recovery'. In: *Climate* 9.4 (2021), p. 58. DOI: 10.3390/cli9040058.

[14] D. Contreras, S. Wilkinson and P. James. 'Earthquake reconnaissance data sources, a literature review'. In: *Earth* 2.4 (2021), pp. 1006–1037. DOI: 10.3390/earth2040060.

[15] D. K. Singh, V. Hoskere and P. Milillo. 'Multiclass post-earthquake building assessment integrating high-resolution optical and SAR satellite imagery, ground motion, and soil data with transformers'. In: *Earthquake Spectra* 41.5 (2025), pp. 3365–3392. DOI: https://doi.org/10.1177/87552930251377778.

[16] L. Moya, F. Yamazaki, W. Liu and M. Yamada. 'Detection of collapsed buildings from LiDAR data due to the 2016 Kumamoto earthquake in Japan'. In: *Natural Hazards and Earth System Sciences* 18.1 (2018), pp. 65–78. DOI: 10.5194/nhess-18-65-2018.

[17] J. F. Falorca, J. P. Miraldes and J. C. G. Lanzinha. 'New trends in visual inspection of buildings and structures: Study for the use of drones'. In: *Open Engineering* 11.1 (2021), pp. 734–743. DOI: 10.1515/eng-2021-0071.

[18] A. Rao, J. Jung, V. Silva, G. Molinario and S.-H. Yun. 'Earthquake building damage detection based on synthetic aperture radar imagery and machine learning'. In: *Natural Hazards and Earth System Sciences Discussions* 23 (2023), pp. 1–32. DOI: 10.5194/nhess-23-789-2023.

[19] F. Foroughnia, V. Macchiarulo, L. Berg, M. DeJong, P. Milillo, K. W. Hudnut, K. Gavin and G. Giardina. 'Quantitative assessment of earthquake-induced building damage at regional scale using LiDAR data'. In: *International Journal of Disaster Risk Reduction* 106 (2024), p. 104403. DOI: 10.1016/j.ijdrr.2024.104403.

[20] L. Li, A. Chang-Richards, M. Boston, K. Elwood and D. Brunsdon. 'A machine learning-supported rapid classification of building damage following the 2010-2011 Canterbury earthquakes'. In: *Journal of Building Engineering* (2025), p. 112807. DOI: 10.1016/j.jobe.2025.112807.

[21] V. I. Novelli and D. D'Ayala. 'Use of the knowledge-based system LOG-IDEAH to assess failure modes of masonry buildings, damaged by L'Aquila earthquake in 2009'. In: *Frontiers in Built Environment* 5 (2019), p. 95. DOI: 10.3389/fbuil.2019.00095.

[22] S. A. Anagnostopoulos, M. Moretti, M. Panoutsopoulou, D. Panagiotopoulou and T. Thoma. *Post-Earthquake Damage and Usability Assessment of Buildings: Further Development and Applications*. Final report. Brussels, Belgium: European Commission, Directorate-General for Humanitarian Aid and Civil Protection, 2008. URL: https://civil-protection-humanitarian-aid.ec.europa.eu/system/files/2014-11/peadab.pdf (visited on 15/08/2026).

[23] H. Kotani, R. Honda, S. Imoto, L. Shakya and B. K. Shrestha. 'Transition of post-disaster housing of rural households: A case study of the 2015 Gorkha earthquake in Nepal'. In: *International Journal of Disaster Risk Reduction* 44 (2020), p. 101443. DOI: 10.1016/j.ijdrr.2019.101443.

[24] S. Voigt, T. Kemper, T. Riedlinger, R. Kiefl, K. Scholte and H. Mehl. 'Satellite image analysis for disaster and crisis-management support'. In: *IEEE Transactions on Geoscience & Remote Sensing* 45.6 (2007), pp. 1520–1528. DOI: 10.1109/TGRS.2007.895830.

[25] P. Ge, H. Gokon and K. Meguro. 'A review on synthetic aperture radar-based building damage assessment in disasters'. In: *Remote Sensing of Environment* 240 (2020), p. 111693. DOI: 10.1016/j.rse.2020.111693.

[26] S. Karimzadeh and M. Matsuoka. 'A preliminary damage assessment using dual path synthetic aperture radar analysis for the M 6.4 Petrinja earthquake (2020), Croatia'. In: *Remote Sensing* 13.12 (2021), p. 2267. DOI: 10.3390/rs13122267.

[27] E. M. Rathje and B. J. Adams. 'The role of remote sensing in earthquake science and engineering: Opportunities and challenges'. In: *Earthquake Spectra* 24.2 (2008), pp. 471–492. DOI: 10.1193/1.2923922.

[28] D. Jin, X. Wang, A. Dou and Y. Dong. 'Post-earthquake building damage assessment in Yushu using airborne SAR imagery'. In: *Earthquake Science* 24.5 (2011), pp. 463–473. DOI: 10.1007/s11589-011-0808-0.

[29] Y. Du, L. Gong, Q. Li and F. Wu. 'Earthquake-induced building damage assessment on SAR multi-texture feature fusion'. In: *IGARSS 2020-2020 IEEE International Geoscience and Remote Sensing Symposium*. IEEE. 2020, pp. 6608–6610. DOI: 10.1109/IGARSS39084.2020.9323644.

[30] F. Eslamizade, H. Rastiveis, N. K. Zahraee, A. Jouybari and A. Shams. 'Decision-level fusion of satellite imagery and LiDAR data for post-earthquake damage map generation in Haiti'. In: *Arabian Journal of Geosciences* 14 (2021), pp. 1–16. DOI: 10.1007/s12517-021-07293-y.

[31] D. Al-Khudhairy, I. Caravaggi and S. Giada. 'Structural damage assessments from IKONOS data using change detection, object-oriented segmentation, and classification techniques'. In: *Photogrammetric Engineerirng & Remote Sensing* 71.7 (2005), pp. 825–837. DOI: 10.14358/PERS.71.7.825.

[32] D. Brown, K. Saito, M. Liu, R. Spence, E. So and M. Ramage. 'The use of remotely sensed data and ground survey tools to assess damage and monitor early recovery following the 12.5. 2008 Wenchuan earthquake in China'. In: *Bulletin of Earthquake Engineering* 10 (2012), pp. 741–764. DOI: 10.1007/s10518-011-9318-7.

[33] R. Anniballe, F. Noto, T. Scalia, C. Bignami, S. Stramondo, M. Chini and N. Pierdicca. 'Earthquake damage mapping: An overall assessment of ground surveys and VHR image change detection after L'Aquila 2009 earthquake'. In: *Remote Sensing of Environment* 210 (2018), pp. 166–178. DOI: 10.1016/j.rse.2018.03.004.

[34] X. Wang and P. Li. 'Extraction of urban building damage using spectral, height, and corner information from VHR satellite images and airborne LiDAR data'. In: *ISPRS Journal of Photogrammetry and Remote Sensing* 159 (2020), pp. 322–336. DOI: 10.1016/j.isprsjprs.2019.11.028.

[35] G. Giardina, V. Macchiarulo, F. Foroughnia, J. N. Jones, M. R. Whitworth, B. Voelker, P. Milillo, C. Penney, K. Adams and T. Kijewski-Correa. 'Combining remote sensing techniques and field surveys for post-earthquake reconnaissance missions'. In: *Bulletin of Earthquake Engineering* (2023), pp. 1–25. DOI: 10.1007/s10518-023-01716-9.

[36] B. Voelker, P. Milillo, A. Tavakkoliestahbanati, V. Macchiarulo, G. Giardina, M. Recla, M. Schmitt, M. Cescon, Y. D. Aktas and E. So. 'The EEFIT remote sensing reconnaissance mission for the February 2023 Turkey earthquakes'. In: *IEEE Journal of Selected Topics in Applied Earth Observations and Remote Sensing* (2024). DOI: 10.1109/JSTARS.2024.3476029.

[37] J. Li, X. Huang, L. Tu, T. Zhang and L. Wang. 'A review of building detection from very high resolution optical remote sensing images'. In: *GIScience & Remote Sensing* 59.1 (2022), pp. 1199–1225. DOI: 10.1080/15481603.2022.2101727.

[38] M. Ji, L. Liu and M. Buchroithner. 'Identifying collapsed buildings using post-earthquake satellite imagery and convolutional neural networks: A case study of the 2010 Haiti earthquake'. In: *Remote Sensing* 10.11 (2018), p. 1689. DOI: 10.3390/rs10111689.

[39] J. Bevington, S. Pyatt, A. Hill, M. Honey, B. Adams, R. Davidson, S. Brink, S. Chang, D. Panjwani, R. Mills, P. Amyx and R. T. Eguchi. *Uncovering community disruption using remote sensing: An assessment of early recovery in post-earthquake Haiti*. Tech. rep. Disaster Research Center, 2010. URL: http://udspace.udel.edu/handle/19716/5850.

[40] S. O. Hashemi Parast, F. Yamazaki and W. Liu. 'Monitoring and evaluation of the urban reconstruction process in Bam, Iran, after the 2003 Mw 6.6 earthquake'. In: *Natural Hazards* 85 (2017), pp. 197–213. DOI: 10.1007/s11069-016-2573-9.

[41] D. Contreras, G. Forino and T. Blaschke. 'Measuring the progress of a recovery process after an earthquake: The Case of L'aquila, Italy'. In: *Internationl Journal of Disaster Risk Reduction* 28 (2018), pp. 450–464. DOI: 10.1016/j.ijdrr.2017.09.048.

[42] H. Miura, S. Midorikawa and M. Matsuoka. 'Building damage assessment using high-resolution satellite SAR images of the 2010 Haiti earthquake'. In: *Earthquake Spectra* 32.1 (2016), pp. 591–610. DOI: 10.1193/033014eqs042m.

[43] G. O. Reddy. 'Satellite remote sensing sensors: principles and applications'. In: *Geospatial Technologies in Land Resources Mapping, Monitoring and Management*. Springer, 2018, pp. 21–43. DOI: 10.1007/978-3-319-78711-4_2.

[44] G. Giardina, V. Macchiarulo, F. Foroughnia, J. N. Jones, M. R. Whitworth, B. Voelker, P. Milillo, C. Penney, K. Adams and T. Kijewski-Correa. 'Combining remote sensing techniques and field surveys for post-earthquake reconnaissance missions'. In: *Bulletin of Earthquake Engineering* 22.7 (2024), pp. 3415–3439. DOI: 10.1007/s10518-023-01716-9.

[45] D. Castelletti, G. Farquharson, J. Brown, S. De, N. Yague–Martinez, C. Stringham, G. Yalla and A. Villarreal. 'Capella space VHR SAR constellation: Advanced tasking patterns and future capabilities'. In: *IGARSS 2022-2022 IEEE International Geoscience and Remote Sensing Symposium*. IEEE. 2022, pp. 4137–4140. DOI: 10.1109/IGARSS46834.2022.9884458.

[46] CDSE. *Copernicus Data Space Ecosystem*. 2025. URL: https://dataspace.copernicus.eu/ (visited on 20/07/2025).

[47] L. Gong, C. Wang, F. Wu, J. Zhang, H. Zhang and Q. Li. 'Earthquake-induced building damage detection with post-event sub-meter VHR TerraSAR-X staring spotlight imagery'. In: *Remote Sensing* 8.11 (2016), p. 887. DOI: 10.3390/rs8110887.

[48] Y. Bai, B. Adriano, E. Mas and S. Koshimura. 'Machine learning based building damage mapping from the ALOS-2/PALSAR-2 SAR imagery: Case study of 2016 Kumamoto earthquake'. In: *Journal of Disaster Research* 12.sp (2017), pp. 646–655. DOI: 10.20965/jdr.2017.p0646.

[49] M. Matsuoka and F. Yamazaki. 'Use of satellite SAR intensity imagery for detecting building areas damaged due to earthquakes'. In: *Earthquake Spectra* 20.3 (2004), pp. 975–994. DOI: 10.1193/1.1774182.

[50] S. Karimzadeh and M. Mastuoka. 'Building damage assessment using multisensor dual-polarized synthetic aperture radar data for the 2016 M 6.2 Amatrice earthquake, Italy'. In: *Remote Sensing* 9.4 (2017), p. 330. DOI: 10.3390/rs9040330.

[51] P. Mazzanti, S. Scancella, M. Virelli, S. Frittelli, V. Nocente and F. Lombardo. 'Assessing the performance of multi-resolution satellite SAR images for post-earthquake damage detection and mapping aimed at emergency response management'. In: *Remote Sensing* 14.9 (2022), p. 2210. DOI: 10.3390/rs14092210.

[52] X. Wang, G. Feng, L. He, Q. An, Z. Xiong, H. Lu, W. Wang, N. Li, Y. Zhao, Y. Wang *et al.* 'Evaluating urban building damage of 2023 Kahramanmaras, Turkey earthquake sequence using SAR change detection'. In: *Sensors* 23.14 (2023), p. 6342. DOI: 10.3390/s23146342.

[53] O. L. Stephenson, T. Köhne, E. Zhan, B. E. Cahill, S.-H. Yun, Z. E. Ross and M. Simons. 'Deep learning-based damage mapping with InSAR coherence time series'. In: *IEEE Transactions on Geoscience & Remote Sensing* 60 (2021), pp. 1–17. DOI: 10.1109/TGRS.2021.3084209.

[54] S. Karimzadeh, M. Matsuoka, M. Miyajima, B. Adriano, A. Fallahi and J. Karashi. 'Sequential SAR coherence method for the monitoring of buildings in Sarpole-Zahab, Iran'. In: *Remote Sensing* 10.8 (2018), p. 1255. DOI: 10.3390/rs10081255.

[55] N. Tamkuan and M. Nagai. 'Fusion of multi-temporal interferometric coherence and optical image data for the 2016 Kumamoto earthquake damage assessment'. In: *ISPRS International Journal of Geo-Information* 6.7 (2017), p. 188. DOI: 10.3390/ijgi6070188.

[56] S. Plank. 'Rapid damage assessment by means of multi-temporal SAR—A comprehensive review and outlook to Sentinel-1'. In: *Remote Sensing* 6.6 (2014), pp. 4870–4906. DOI: 10.3390/rs6064870.

[57] L. Ge, A. H.-M. Ng, X. Li, Y. Liu, Z. Du and Q. Liu. 'Near real-time satellite mapping of the 2015 Gorkha earthquake, Nepal'. In: *Annals of GIS* 21.3 (2015), pp. 175–190. DOI: 10.1080/19475683.2015.1068221.

[58] H. Rastiveis, F. Eslamizade and E. Hosseini-Zirdoo. 'Building damage assessment after earthquake using post-event LiDAR data'. In: *The International Archives of the Photogrammetry, Remote Sensing and Spatial Information Sciences* 40 (2015), pp. 595–600. DOI: 10.5194/isprsarchives-XL-1-W5-595-2015.

2

QUANTITATIVE ASSESSMENT OF EARTHQUAKE-INDUCED BUILDING DAMAGE AT REGIONAL SCALE USING LIDAR DATA

Regional-scale assessment of earthquake damage to structures is crucial for post-disaster management. While Remote Sensing (RS) techniques can be of great help for a quick post-event structural assessment of large areas, currently available methods are limited to detecting severely damaged buildings. Furthermore, RS-based assessment methods typically provide only qualitative results, as they lack integration with information on the building's behaviour in response to seismic-induced ground shaking. In this chapter, we developed a new methodology that uses airborne Light Detection and Ranging (LiDAR) data, combined with structural indicators of building response, to provide a quantitative assessment of earthquake-induced damage at a regional scale. LiDAR datasets collected before and after an earthquake are used to measure residual displacements of building roofs. The resulting lateral drift estimations are used to quantify the level of damage for a specific building typology. Application to the LiDAR datasets collected before and after the 2014 earthquake in Napa Valley, California, demonstrates the proposed method's capability to detect moderate levels of structural damage, underscoring its potential for more efficient and scalable support for post-disaster management.

The work presented in this chapter was published in Foroughnia, F., Macchiarulo, V., Berg, L., DeJong, M., Milillo, P., Hudnut, K.W., Gavin, K. and Giardina, G., 2024. Quantitative assessment of earthquake-induced building damage at regional scale using LiDAR data. *International Journal of Disaster Risk Reduction*, 106, p.104403.

2.1. INTRODUCTION

As discussed in Chapter 1, rapid and reliable assessment of earthquake-induced building damage is essential for post-disaster response and recovery, particularly over large affected areas. Remote Sensing (RS) provides a complementary means of extending building damage assessment to regional scales. Existing RS-based approaches generally rely on either post-event classification or multi-temporal change detection. While classification approaches infer damage from post-event image characteristics, change-detection approaches identify earthquake-induced changes by comparing pre- and post-event observations. Among these, change-detection approaches are particularly relevant to the methodology developed in this chapter. Change-detection approaches have been applied to optical and Synthetic Aperture Radar (SAR) data using changes in spectral [1, 2], intensity, and coherence information [3, 4]. Beyond image-based observations, change-detection approaches leveraging airborne Light Detection and Ranging (LiDAR) elevation data have been used to assess three-dimensional geometric changes and identify collapsed buildings [5–7].

LiDAR sensors emit a laser pulse towards the ground surface and record the time for the reflected pulse to return to the sensor, resulting in distance and three-dimensional measurements of ground target locations. These measurements can provide high-precision three-dimensional representations of the ground surface and built environment, with typical vertical and horizontal Root Mean Square Errors (RMSEs) ranging from 5 to 10 cm and 10 to 25 cm, respectively [8]. This high geometric accuracy enables the identification of changes in building geometry by comparing pre- and post-event observations.

In previous studies, damaged buildings were identified by detecting changes in the average building height from LiDAR-derived Digital Surface Models (DSMs) before and after an earthquake. However, earthquake-induced horizontal ground displacement can cause the same building to occupy slightly different horizontal positions in the pre- and post-event DSM. Direct comparison without accounting for this displacement may therefore introduce apparent elevation differences that do not represent actual changes in building height. To ensure that corresponding building surfaces are compared, a preliminary horizontal co-registration of the pre- and post-event DSM can be performed before calculating elevation changes [5]. Nevertheless, this approach can detect damage that results in a notable variation in building height, such as partial or complete collapse [9]. Damage that does not substantially alter the building's vertical geometry may therefore remain undetected. Other LiDAR-derived geometric characteristics have also been explored for building damage assessment, including changes in roof shape, slope [10], surface orientation [11], and three-dimensional shape descriptors [12]. These parameters leverage the geometric information from LiDAR point clouds to identify alterations in building and roof morphology associated with damage.

While these approaches are effective in distinguishing between collapsed or severely damaged and undamaged buildings, they fall short of accurately measuring the extent of damage, particularly at the slight or moderate levels. This limitation arises from their reliance primarily on observable geometric changes, such as variations in building height, roof slope, shape, and surface orientation. Such changes are generally more pronounced when damage substantially alters the building geometry. Consequently, these approaches

are particularly effective in identifying severely damaged or collapsed structures that produce clearly discernible changes in RS imagery. For instance, severe damage or complete collapse can be indicated by the disappearance of a building footprint, a significant reduction in building height, or the presence of rubble and debris in the surrounding areas. Since they cannot provide insights into structural failure mechanisms, these approaches are inadequate for quantifying the extent of damage. Therefore, accurately quantifying and evaluating slight-to-moderate damage remains challenging.

To quantitatively assess building damage across various levels, including slight-to-moderate damage, displacement is a more effective performance indicator, as it is directly linked to building deformations and can aid in identifying failure mechanisms. For instance, lateral drift measurements derived from building displacements are commonly used to quantify the extent of damage caused by flexural and shear seismic mechanisms [13]. The peak drift ratio, defined as the ratio of the maximum roof drift to the building height, has been proven effective for a rapid evaluation of earthquake impacts on buildings [13–15]. Because peak drift can only be measured by a monitoring system installed on the building during the seismic event, estimating it is not practically applicable to most buildings [14]. A more practical indicator is the residual drift, which corresponds to the building's permanent displacement measured at the end of the seismic event [13, 16]. Importantly, the relationship between residual drift and damage severity should be interpreted in relation to the structural system, as different systems exhibit different deformation capacities and residual-drift behaviour [17].

Building displacements can be estimated by differential LiDAR-based approaches. Since the three-dimensional coordinates of the ground surface targets are measured by LiDAR sensors, pre-and post-event LiDAR data can be used to obtain three-dimensional ground surface displacement measurements regardless of fault ruptures and displacement magnitudes, as demonstrated in [8, 18–21]. Two differential approaches can be employed to generate displacement vectors from LiDAR observations: the Particle Image Velocimetry (PIV) and the Iterative Closest Point (ICP) methods.

The PIV method, originally developed in fluid mechanics, determines the displacement vectors of fluid particles within a given space by finding correlations between images of the particles acquired over a short time span [22]. This method has been adopted in seismic applications to obtain seismic-induced displacement vectors using LiDAR data [23–26]. It requires pre- and post-event LiDAR datasets, such as intensity or elevation imagery, to perform a spatial cross-correlation analysis between them and estimate the displacements that occurred. However, as LiDAR observations are recorded as discrete points, an additional step of creating two-dimensional images through gridding or smoothing of the point observations is required. Consequently, not only does the method fail to provide separate displacement measurements for buildings, but the smoothing process may introduce biases within the displacement results [8].

The ICP method, on the other hand, uses the point observations to align two three-dimensional point clouds by minimising the distance between the clouds [27, 28]. The method has the potential to be adopted for monitoring ground seismic displacements using airborne LiDAR clouds [8, 21], based on the assumption that the transition vector aligning the two clouds before and after an earthquake equals the earthquake-induced ground surface movement. Unlike the PIV method, the ICP

method can also theoretically provide direct measurements of building displacements by aligning two point clouds acquired at different times. Since each cloud includes height information, it is possible to separate points on building roofs from points at the ground level to estimate the displacement vectors for each building individually. Various studies have used the ICP technique in earthquake-related applications [8, 21], focusing specifically on the estimation of earthquake-induced deformations of the ground surface. However, these studies did not address the measurements of earthquake-induced structural deformations in buildings. The study by [29] is the only research that applied the ICP technique to LiDAR building observations, but to assess landslide-induced changes in a small area.

In this chapter, we exploited the potential of the ICP method to develop a novel approach to quantitatively assess building damage after an earthquake. As opposed to qualitative observation-based methods, we developed a methodology that integrates RS LiDAR data with structural analysis to detect moderate levels of damage on a large scale, characterised by effects such as large cracks at the corners of openings for the light-frame wood building typology considered in this study [17]. Our approach involved analysing LiDAR data acquired before and after the earthquake to determine the residual displacements of buildings. Building displacement measurements enable identification of damage levels that are not directly visible through RS images or height data. The method classifies damage levels by converting building residual displacements into drift measurements, enabling regional-scale damage classification ranging from slight to moderate. We evaluated the performance of the proposed methodology by using LiDAR datasets acquired before and after the 2014 South Napa earthquake in California. Results were compared to observations from field investigations [18, 30].

2.2. CASE STUDY AND DATASETS

On August 24, 2014, a moment magnitude (Mw) 6.0 earthquake struck the North San Francisco Bay Area, California. The epicentre was located to the south of Napa Valley at N38.220 W122.313, roughly 8 km south-southwest of the City of Napa, at a depth of approximately 11 km [31]. The earthquake ruptured the ground surface along several strands of the West Napa Fault zone, which is part of the larger San Andreas Fault Zone System. The surface rupture had a length of 12−15 km, extending northward from Cuttings Wharf town to Alston Park, in the City of Napa (Figure 2.1). The 2014 South Napa earthquake was the first to cause substantial surface ruptures in a densely urbanised area in Northern California since the 1960 San Andreas event. A co-seismic slip of 1.5 to 46 cm occurred along the earthquake rupture, which was predominantly right lateral [32].

The City of Napa was among the most affected areas. At least $300 million worth of economic impact was observed on private and commercial properties, while public infrastructure incurred $58 million in damage [36]. Damage was observed from the Browns Valley residential neighbourhood to the east of the downtown area, where some residential buildings exhibited foundation shifts, wall cracks and chimney collapses. In Napa downtown, some historic masonry buildings were also severely damaged [37]. The study area (Figure 2.1) is located in the south part of the Browns Valley neighbourhood

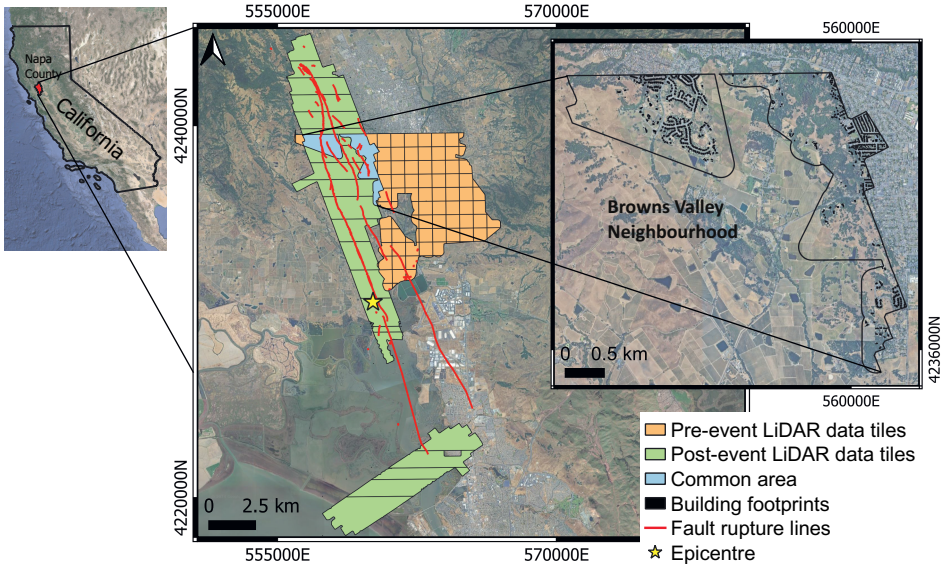

Figure 2.1.: Case study area, showing the regions covered by pre- and post-event LiDAR data. Red lines indicate fault ruptures [33]. The black polygons refer to building footprints, obtained from OpenStreetMap (OSM) [34] data layer and the Napa municipality [35].

and includes wood-frame structures [38], which mostly suffered from cracked walls, and fallen or cracked chimneys [37].

2.2.1. LIDAR DATA

We used two point clouds acquired before and after the earthquake. The pre-earthquake dataset was collected on June 7th, 2014, over Napa County by an airborne Leica ALS60 with a nominal point density of 8 pts/m^2. The data was initially in the Coordinate Reference System (CRS) of NAD83 California State Plane Zone II with units of survey feet and NAVD88 orthometric elevations.

Following the 24th August earthquake, a post-earthquake dataset, distributed by [39], was acquired on the 9th of September by an Optech Orion M300 scanner, achieving point densities of approximately 11.4 pts/m^2 [20]. The elevation observations obtained from the post-event LiDAR were validated by the vendor using eight ground control points, demonstrating high accuracy and an error of approximately 1.2 cm. The post-event data were projected in the CRS of NAD83 UTM Zone 10N, with both horizontal and vertical measurements in meters. Consequently, to ensure consistency, we also transformed the pre-event data to match the CRS of the post-event dataset. The post-event point cloud was classified by the vendor using the TerraScan software. The software classifies ground points by creating a triangulated surface model. Points within 0.05 m of the triangulated ground surface were incorporated into the model, resulting in a sparse ground model

containing some artefacts. To remove the artefacts from the sparse ground model, points that were up to 0.15 m from the ground model were added, leading to the creation of a denser and more accurate ground model [40].

The post-event data were originally classified into seven classes: unclassified, ground, low vegetation, medium vegetation, high vegetation, building, and outlier points according to Terrascan's proprietary algorithm based on specified setting parameters. For the rich dataset used in this study, the classification parameters defined low vegetation as points 0 m to 0.15 m above the triangulated ground model, medium vegetation as points 0.15 m to 2.0 m above the ground model, and high vegetation as points 2 m to 70 m above the ground model. The building-classification routine used a minimum building-size parameter of 50 m^2. However, the pre-event data had not been classified prior to this analysis. The classification of the pre-event data was conducted using LAStools functions implemented in a Quantum Geographic Information System (QGIS) environment [41]. We first identified the ground points and then classified the building points based on their height information.

The geographical extent of the two surveys is shown in Figure 2.1. This study focuses on the overlapping area between the two surveys, which is approximately 4.7 km^2 (Figure 2.1).

2.2.2. BUILDING FOOTPRINT DATASET

Building footprint layers were used to extract the roof observation points from the LiDAR building clouds. The commonly used data source for this purpose is the OpenStreetMap (OSM) building footprint layer [34]. However, the OSM layer did not include all buildings within the area of interest. To address this limitation, we used the footprints provided by the Napa Municipality [35]. As the Municipality layer does not accurately represent the real shapes of building roofs, we combined the two footprint layers into one, using the Municipality data only for areas without OSM footprints, aiming to extract as many buildings as possible. In total, we extracted 684 buildings for the damage level assessment, as shown in Figure 2.1.

2.2.3. FIELD DATA

The United States Geological Survey (USGS) team carried out field measurements during the three months following the 2014 South Napa earthquake. Their work, detailed in [18], included an evaluation of afterslip observations, an investigation of seismic shaking-related damage in the downtown area, and mapping of fault strands, which are active or might be a threat to future ruptures. They also provided geospatial information derived from several imagery sources, including aerial photographs, airborne LiDAR data, medium-resolution Landsat-8 and SPOT-6 imagery, and high-resolution WorldView-2 and QuickBird-1 optical images. To evaluate our work, we used lateral ground offset displacements as the ground truth.

Furthermore, the California Governor's Office of Emergency Services (Cal OES) conducted field inspections to assess building damage. These inspections resulted in a dataset in which some buildings were restricted in use (yellow-tagged), and others were deemed unsafe (red-tagged). The building tagging data consists of 1572 yellow- and 152

red-tagged structures and is available at [30]. Geospatial records of inspected buildings show that red and yellow tags were distributed across the City of Napa, from the west of the Browns Valley to the east of the Napa River [37]. Most red-tagged structures were located in downtown Napa, where pre-LiDAR data was not available. Figure 2.2 shows the distribution of tagged buildings within our region of interest. Within this area, 39 buildings were tagged: 38 yellow-tagged and 1 red-tagged. No tagging information was available for the remaining buildings.

2.3. METHODOLOGY

We developed a new methodology for quantifying the extent of building damage at a regional scale by using RS LiDAR data. Our approach combines LiDAR-derived displacements with structural analysis to derive building drift measurements. These measurements enable us to categorise the level of damage for each building. Figure 2.3 depicts a visual schematic representation of the proposed methodology.

The method first classifies the LiDAR clouds to extract the ground and building points. The ICP registration method [27] is then applied to pre- and post-event ground and building points to obtain three-dimensional displacement vectors. We designed two strategies of point-based and window-based alignment in the ICP approach to process the building and ground point clouds, respectively. In the building cloud processing, an estimate of three-dimensional displacements was obtained for each roof point. LiDAR observations of buildings consist of coordinates of the roofs, indicating building positions on the ground. Hence, the transition vectors obtained from the ICP alignment of the roof points also include the contribution of ground displacements. For this reason, we estimated the ground displacements to subtract them from the building displacements.

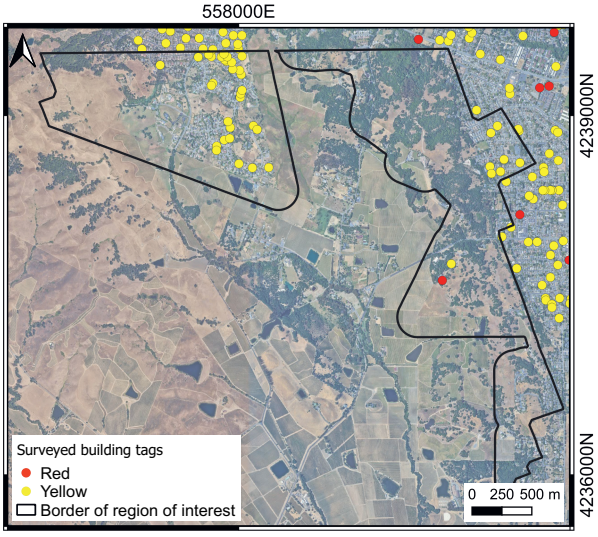

Figure 2.2.: Distribution of yellow- and red-tagged buildings in the region of interest.

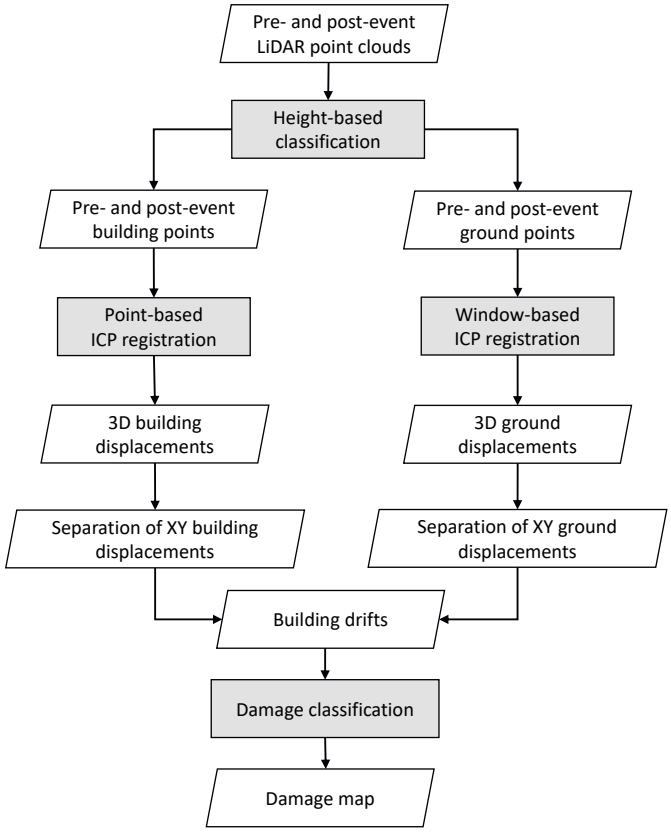

Figure 2.3.: Flowchart of the proposed approach.

The application of the ICP method to estimate ground displacements was inspired by the window-based ICP registration as described in [8]. As the ground deformations might vary with distance from the fault, we divided the datasets into 100 x100 m^2 windows and then applied the point-based ICP to all point observations within each window separately.

After separating the X and Y displacement components, the residual building displacements, i.e. displacements at the building level after removing the ground components, were derived. Finally, we determined the level of damage for each building by correlating these residual building displacements with residual drift ratios. The ICP approach and subsequent steps for damage quantification are described below.

2.3.1. ITERATIVE CLOSEST POINT (ICP)

In the ICP algorithm, one cloud is considered fixed as a reference cloud, and the other as a target cloud. The ICP aligns the target cloud with the reference one iteratively [27]. The

post-event point cloud served as the reference, and the pre-event cloud as the target in this study.

First, we used the KD-tree nearest neighbour algorithm [42] to identify the closest corresponding point in the reference cloud for each point in the target cloud. Second, we applied a point-to-point rigid-body transformation function to the target cloud, including a transition vector and a rotation matrix. The function minimises an error metric, i.e. Mean Square Error (MSE), between all corresponding pairs. The target cloud iteratively converges toward the reference set as the correspondences progressively improve. The procedure of determining correspondences and computing the transformation repeats until the MSE does not change any longer or reaches a predefined threshold. This corresponds to a linear least-squares problem that was solved robustly by the Singular Value Decomposition (SVD) method [19]. The algorithm also reduces the impact of outliers by adding weight to corresponding pairs based on the distance criterion [43]. For each point, the displacement vectors are the sum of the transition vectors in horizontal and vertical directions over the iterations.

As misclassified points and outliers, e.g. vegetation can negatively affect the registration result, we added a rejection step to exclude invalid correspondences from the ICP chain processing. The rejection step filters out false correspondences based on distance and normal vector compatibility criteria.

2.3.2. DRIFTS AND DAMAGE CLASSIFICATION

A 4-m buffer was used to extract the points around each building. We then calculated the average ground displacements of the points within the buffers. To obtain the residual building displacements, the average ground displacement was subtracted from each building point's displacement. To estimate the residual drift ratios D, we first calculated the average residual building displacements of all roof points in the X and Y directions separately. The maximum average value was then divided by the average building height to obtain the drift ratio for each building. The building height was estimated by subtracting the average Z-coordinate of ground points within the buffer from that of the roof points. Finally, the drift ratios were used to classify the level of damage to buildings from slight to complete.

As the building stock analysed in this work consists of wooden-frame structures, we used the damage level classification from [44] for this structural typology. Specifically, the damage level was categorised as negligible for $D < 0.42\%$, slight for $0.42\% \leq D < 1\%$, moderate for $1\% \leq D < 3.2\%$, extensive for $3.2\% \leq D < 7.9\%$, and complete for $D \geq 7.9\%$. This classification is based on the Hazards U.S. (HAZUS) loss estimation approach [17] to assess earthquake damage to buildings. The slight and moderate levels of damage refer to small and large cracks at the corners of openings, respectively. Extensive damage corresponds to large diagonal cracks and residual displacements in shear walls, while large permanent deformation of the building and foundation movement indicates complete damage [44].

2.4. Results and discussion

In this section, we first present the displacement results at the ground and building levels, and then proceed to derive and discuss the corresponding building damage levels.

2.4.1. Ground-level displacements

The pre- and post-ground point clouds were divided into windows based on their X and Y coordinates. Additionally, we incorporated observation points within a buffer of 10 m around windows of the post-event cloud. This was necessary to ensure that all topography features present in the pre-event cloud remained included in the post-event cloud, as the two clouds were not yet aligned. To align the ground point clouds, windows were progressively moved across the analysed area by increments of a given size. These increments are here defined as steps. We initially adopted window and step sizes of 100 m and 25 m, respectively, as proposed by [19]. This led to a window-side overlap of 75 m between two consecutive windows, ensuring smooth continuity in the displacement pattern. Smaller step sizes led to larger overlaps, further enhancing the smoothness of displacements. This was tested by considering different step sizes of 25, 50, and 75 m, while maintaining a fixed window size of 100 m. Additionally, we tested different window sizes, such as 30, 50, 100, and 200 m, to assess their impact on the final results. Results showed similar patterns and magnitudes of deformation, indicating no significant dependence on the window size. Consequently, we adopted the initial window and step sizes of 100 m and 25 m, respectively, to estimate the ground displacements.

Figure 2.4 shows the maps of three-dimensional ground displacements induced by the South Napa earthquake. The ground results show that most of the displacement occurred in the Y direction, with the largest movement on the left side of the fault. This agrees with the in-situ ground motion observations, indicating that the earthquake primarily exhibited a right-lateral strike-slip behaviour [18]. Similar studies conducted in the Browns Valley area to estimate the ground displacement support these findings. For example, [20] also obtained a comparable right-lateral pattern and magnitude of displacements. However, their results indicated that the ground surface on both sides of the main rupture moved in the same direction. In contrast, the displacement field obtained in this study showed a distinct discontinuity in the displacement pattern, accurately representing the location of the fault rupture. This discrepancy may arise from differences in the weighting procedures for corresponding pairs in the ICP registration. Another study conducted by [45] also identified a discernible displacement pattern, despite applying different data preparations and using unweighted least squares to minimise the MSE. Their results showed smoother, higher-resolution displacement estimates, as a smaller window size of 64 m and a step size of 8 m were used during processing.

As shown in Figures 2.4a, 2.4c and 2.4e, some areas exhibit significantly larger amounts of displacements, represented by dark blue or dark red colours. These regions correspond to locations where no post-event data were available, resulting in inaccurate point correspondences within the reference data cloud. To address this issue, false corresponding pairs were eliminated during the rejection step described in Section 2.3. In this step, pairs of points with a distance exceeding 30 cm and normal vectors having an angle larger than the average normal angle of all corresponding pairs within the

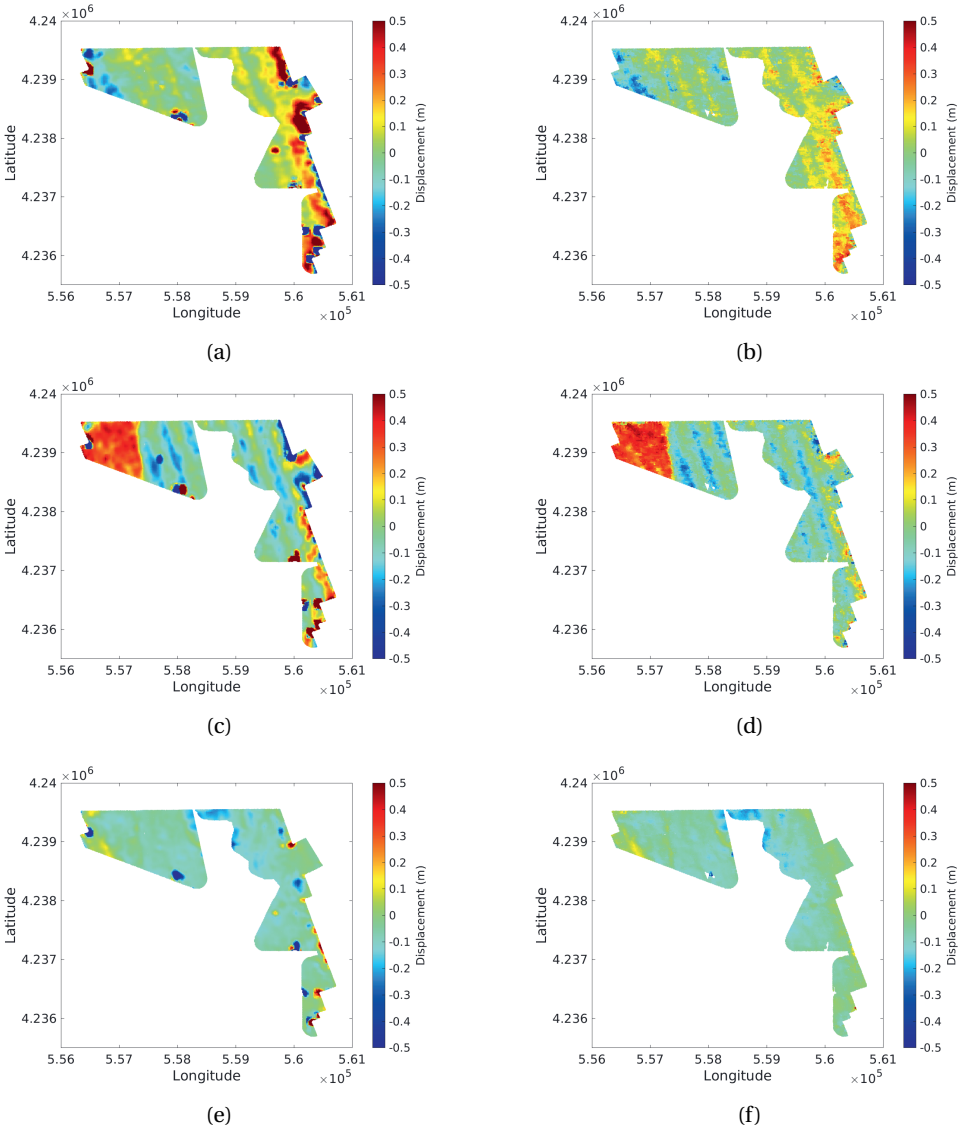

Figure 2.4.: LiDAR-derived ground displacement maps in (a) X, (c) Y, and (e) Z directions. Figures (b), (d) and (f) show the corresponding maps where false correspondence pairs were removed (Section 2.3).

window were excluded. The resulting ground displacement maps, post-rejection step, are presented in Figures 2.4b, 2.4d, and 2.4f.

The ground displacement results (Figure 2.4) reveal a distinct regular pattern of movements in horizontal directions. This pattern is consistent with a systematic error in the X component, and particularly in the Y component, which appears to correlate with the flight line direction of the pre-event survey. This suggests the presence of pre-processing errors in the pre-event LiDAR point cloud. Investigating these systematic errors would require access to raw LiDAR data and navigation information from the pre-event survey [46], which were not available for the current study. Although this possible systematic error could introduce bias in both the ground and building displacement measurements, its impact on the final estimations of building drift measurements is expected to be minimal. Since the error affects both ground and building measurements, it is presumed to be neutralised when subtracting the ground displacements from the building displacements to calculate the residual building displacements. Additionally, any remaining random errors were mitigated by averaging the residual building displacements to estimate the drifts.

2.4.2. BUILDING DRIFTS AND DAMAGE ASSESSMENT

We processed 684 buildings extracted from the OSM [34] and the Napa municipality [35] data layers. After extracting the building points, we separately aligned the pre- and post-event roof points using the point-based ICP approach. The ICP registration estimates the shifts and rotations between the two building clouds, providing building displacement vectors. To illustrate the effectiveness of the ICP alignment, we depicted the distribution of roof points (for one random building in the area) before and after the ICP registration in Figure 2.5. This visualisation confirms that the ICP process effectively aligned the pre- and post-event point observations. Furthermore, Figure 2.6 shows the location of building roof points for an individual building, along with the distribution of the ground points within a 4-m buffer around the building. The estimated Y displacement components for the building roof points are visualised using a colour gradient, with the scale ranging from smaller (red) to larger (blue) values.

To estimate the drift ratio for each building, we computed the residual building displacements by subtracting the average ground displacement component from the building measurements. The histograms of these residual building displacements in horizontal directions are presented in Figure 2.7. The majority of buildings exhibited small residuals. The large residual displacement observed for some buildings might also be attributed to tree leaves on their roofs. Classifying trees with heights similar to building roofs as roof points can introduce a bias in the building displacement vectors. This issue could be addressed by incorporating optical Red–Green–Blue (RGB) information from the observations to accurately identify tree points and exclude them from building roofs, further enhancing the accuracy of the results. A level of damage was then assigned to each building by estimating the drift ratios and classifying them into five levels of damage, as described in Section 2.3. These damage categories are specific to light-frame wood constructions designed for specific seismic zones in California. Therefore, they may not be directly applicable to other case studies in different regions or construction types.

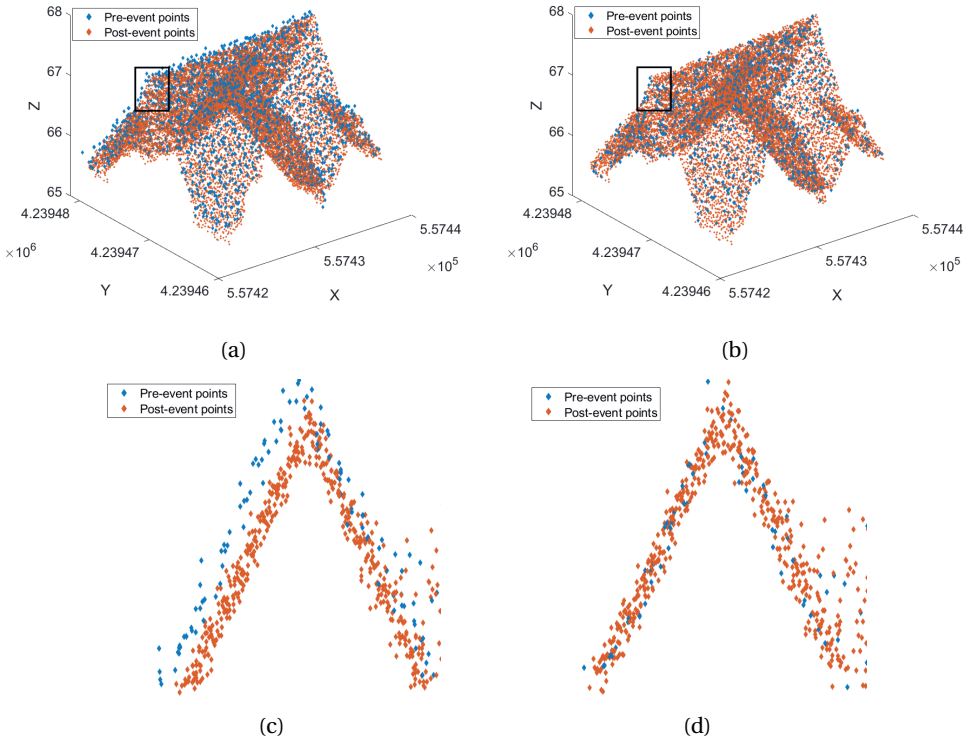

Figure 2.5.: An example of the distribution of building roof points for (a) before and (b) after the ICP registration. Figures (c) and (d) are close-up views of before and after the ICP registration for one of the roof corners, shown by black rectangles in (a) and (b).

The map and distribution of obtained damage levels are illustrated in Figures 2.8 and 2.9, respectively. Figure 2.8 visually represents building damage levels by colours ranging from green to red, indicating varying degrees of damage in the Napa Valley area. The map shows that most of the building damage across the area of interest is at moderate levels. This observation is further supported by Figure 2.9, which shows that the majority of buildings exhibit negligible-to-moderate damage, with only a few classified as extensively damaged. Specifically, the percentage distribution of obtained damage levels is approximately as follows: negligible damage 27.8%, slight damage 28.3%, moderate damage 38.5%, extensive damage 5.2%, and complete damage 0.1%.

2.5. VALIDATION

The field datasets were used to validate the ground displacements, followed by an evaluation of the obtained building damage levels.

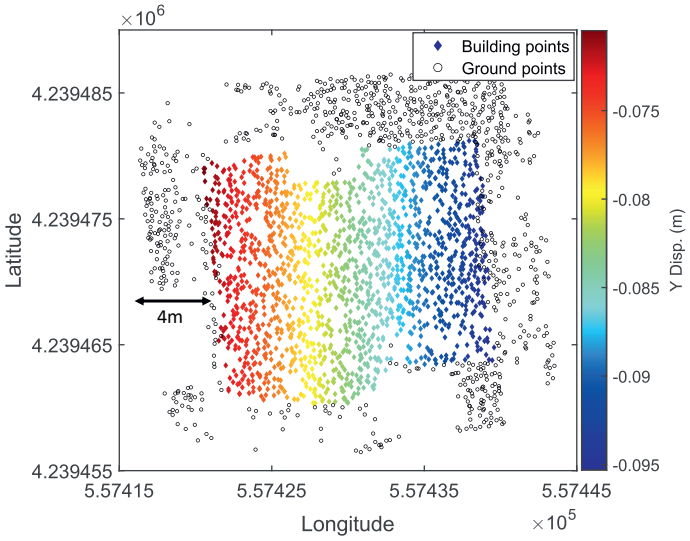

Figure 2.6.: An example of a two-dimensional map of building roof Y displacements. Displacements of the ground points within a 4-m buffer around the buildings were used to estimate the residual building displacements.

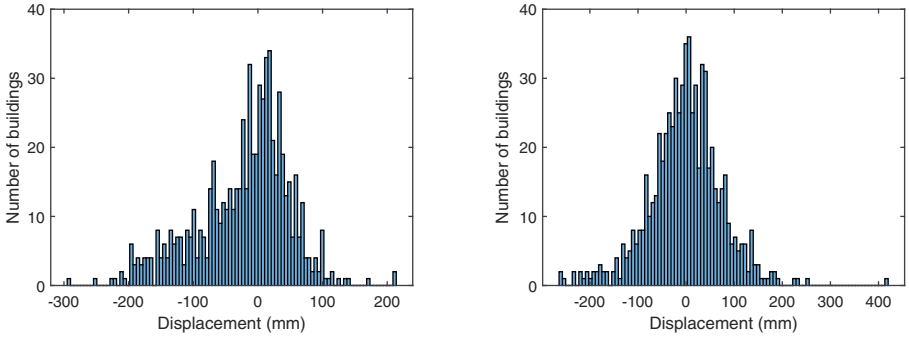

(a) (b)

Figure 2.7.: Distribution of residual building displacements in (a) X and (b) Y directions for all buildings in the area of interest. The residual building displacements were obtained by subtracting the average ground displacements within a buffer of 4 m around each building.

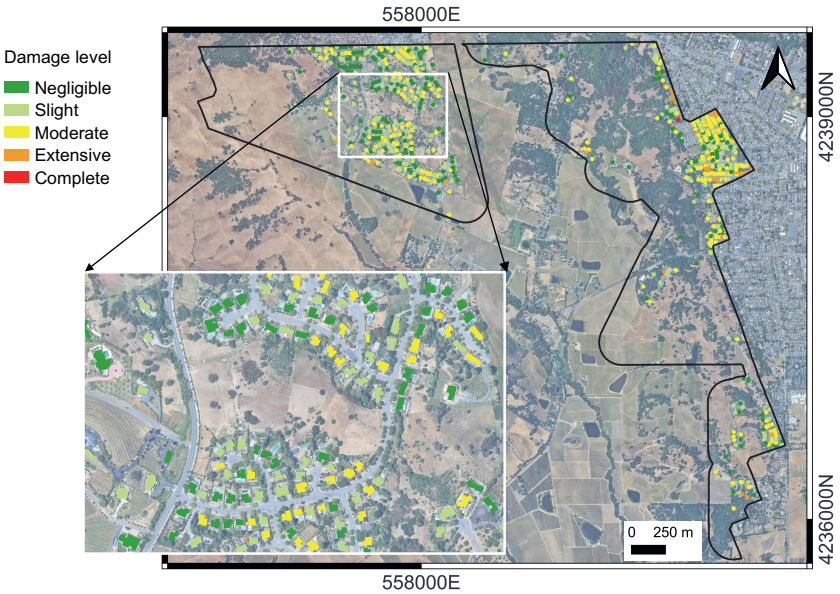

Figure 2.8.: Building damage map. Building damage levels are based on the residual drift ratios derived from LiDAR displacement measurements.

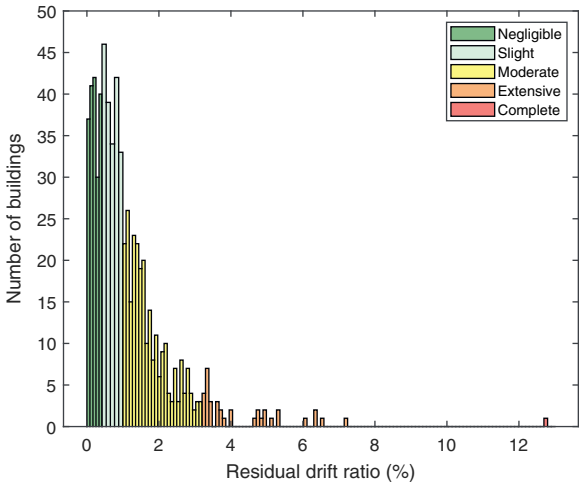

Figure 2.9.: Distribution of building damage levels in the region of interest.

2.5.1. GROUND DISPLACEMENT VALIDATION

To quantitatively validate the ground displacement estimation, we compared these results with independently acquired field data by the USGS team [18]. The USGS observations included measurements of right-lateral offsets along the fault strands at several locations. During the field survey, the largest lateral offsets were observed along the longest fault strand on the west of the Napa Valley (trace A in Figure 2.10a). The maximum displacement of 46 cm was recorded approximately 10 km from the epicentre towards the northwest [18]. Additionally, the slip observations on trace A included both co-seismic and afterslip measurements.

Figure 2.10a shows the locations inspected in the field along trace A, as documented by [18]. Within the area of interest, there was only one offset observation of 36 cm. Since the exact measurement locations were not available, we analysed a range of displacement magnitudes along the fault strand within the area of interest. To achieve this, perpendicular cross-sections, each with a length of 200 m, were created at intervals of 50 m, resulting in 20 cross lines (Figure 2.10b).

For the cross-section displacement estimation, we defined a 1-m-wide buffer on either side of each cross-section and extracted the displacement points within the corresponding buffer regions. We included points within 100 m on each side of the rupture in the cross-section displacement estimation, as significant relative displacements attributable to the fault rupture were not observed further away from the fault. The average magnitudes of Y-direction displacement were then calculated along each side of each cross-section. To obtain the offset of Y-direction displacements for each cross-section, we subtracted the average magnitude on the right side from the average magnitude on the left side. As the LiDAR-derived measurements were in the geographical coordinate system, the offsets were estimated along the north-south direction. To compare these estimated offsets with the ground measurements, we projected them to the fault direction using the angle between the offset displacement vector and the fault

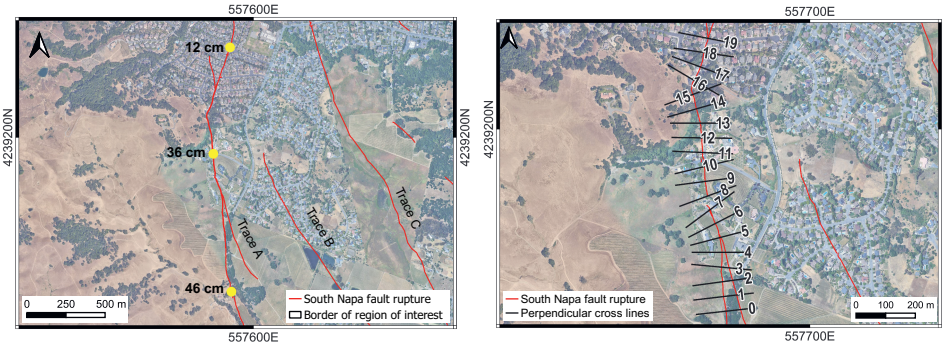

(a) (b)

Figure 2.10.: (a) In-situ right-lateral displacements along trace A, showing the maximum measured slip in the selected sites, rounded to the nearest cm [18] and (b) cross-sections along trace A.

line. For example, Figure 2.11 shows the spatial profile of displacement measurements along cross-section number 10 within the 200 m length. The displacement profile shows an offset of about 37 cm along the north-south direction, which corresponds to 35 cm when projected along the fault rupture direction.

Table 2.1 shows all the offset measurements parallel to the fault rupture. The range of magnitudes along the fault, from south to north (number 0 to 19), is in good agreement with the field observations. More specifically, offset numbers 9, 10, and 11 correspond to the area of the in-situ measurement of 36 cm. The average magnitude of these offsets obtained by LiDAR data is 35.9 cm. This consistency indicates that the LiDAR-derived ground displacement is reliable for further analysis, specifically for quantifying the damage level for each building using residual building displacements.

Additionally, we employed an additional coding source to evaluate the obtained results. Specifically, we used the Point Data Abstraction Library (PDAL), an open-source Python library designed for LiDAR data processing, as described in [47]. In their research, the authors used PDAL's Python extension to quantify ground deformation following the 2014 Napa earthquake. They analysed pre- and post-event airborne LiDAR point cloud data using an ICP algorithm. To ensure consistency, we focused on the same region of interest within the extent of our data coverage and replicated the parameters outlined in [47]. Our analysis yielded outcomes that showed similar patterns and magnitudes of displacement to those observed in their study.

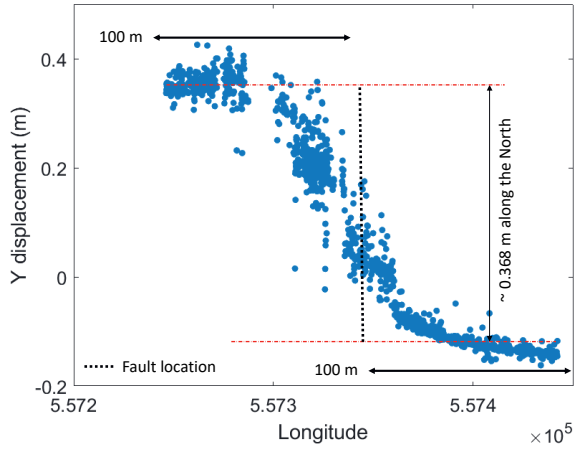

Figure 2.11.: Spatial profile of ground displacements along the cross-section number 10 shown in Figure 2.10b. The black dashed line indicates the fault rupture location.

Table 2.1.: Offset measurements parallel to the fault rupture along the cross-sections represented in Figure 2.10b.

Cross-section number	LiDAR-derived offsets parallel to the fault (cm)
0	23.20
1	25.20
2	27.01
3	31.30
4	31.00
5	29.07
6	30.05
7	27.05
8	29.30
9	37.50
10	35.40
11	34.90
12	40.60
13	37.80
14	39.70
15	28.40
16	19.60
17	18.50
18	23.70
19	17.30

2.5.2. BUILDING DAMAGE VALIDATION

To validate the building-level results, we used information from tagged buildings as outlined in Section 2.2. As shown in Figure 2.12, the distribution of LiDAR-derived damage levels for the yellow-tagged buildings mostly fell in the range of negligible, slight, and moderate levels. This is in agreement with the field damage observations. LiDAR-based results indicated complete damage only for one of the buildings, which does not correspond to the field-based red-tagged. The field-based red-tagged building was classified as a moderately damaged building based on LiDAR observations. As the building classified as completely damaged from LiDAR observations was not tagged, and no further information was available on the red-tagged building, no speculation can be made on the reasons for discrepancies in these two individual cases.

While the validation confirmed the effectiveness of the method in detecting moderate damage levels and its applicability to the analysed building typology, the building-level validation was limited to 39 structures and was not evenly distributed across damage levels. It is advisable to extend future applications to a broader array of field observations and various building typologies to generalise these findings. Given its emphasis on assessing moderate damage through building drift evaluation, this approach is

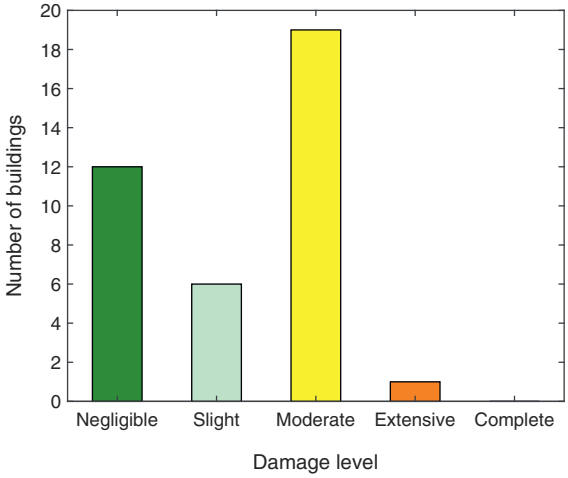

Figure 2.12.: Distribution of the 38 yellow-tagged buildings in the region of interest.

complementary to damage detection and classification methods that utilise SAR, optical satellite, or LiDAR elevation data, which are primarily concerned with identifying severely damaged and collapsed structures.

A current limitation of the method is the necessity for both pre- and post-event LiDAR data. When pre-event LiDAR data is not available, alternative sources of pre-event data can be used, including aerial imagery or a high-resolution DSM. It is possible to generate three-dimensional point clouds from alternative data sources and photogrammetric methods [48], although their accuracy depends on factors such as imagery resolution, DSM quality, and the processing techniques employed. In addition to data availability, the reliability of the estimated building displacements depends on the quality and spatial distribution of the LiDAR observations. Insufficient point density or occlusions can result in incomplete sampling of building surfaces, while vegetation may obscure or contaminate roof observations. These factors can reduce the number and distribution of corresponding building points available across pre- and post-event acquisitions, thereby affecting displacement estimation. A similar limitation arises for severely damaged or collapsed buildings, where substantial alteration or loss of the roof may prevent sufficient correspondence between the pre- and post-event point clouds for reliable displacement estimation. In such cases, other LiDAR-derived indicators, such as changes in building height, roof shape, surface orientation, or three-dimensional geometry, may provide complementary information, as these features are sensitive to the morphological changes associated with severe damage and collapse. Combining such geometric indicators with the displacement-based approach could therefore extend the methodology across a broader range of damage states. Residual displacement can provide a physically interpretable measure when sufficient building geometry is preserved, while indicators of geometric change can support the identification of buildings for which reliable displacement estimation is no longer possible.

Beyond the availability and correspondence of building observations, measurement uncertainty in the LiDAR data also affects the reliability of the derived displacement indicators. Although the effects of systematic and random errors in the LiDAR observations were identified and mitigated through the differential and averaging procedures described above, their uncertainties were not explicitly propagated into the derived residual displacements and drift ratios. Future work could quantify this uncertainty propagation to further characterise the reliability of the resulting damage classification.

A further limitation concerns the use of residual drift as an indicator of structural damage. The approach is most sensitive to damage mechanisms that produce measurable permanent deformation at the building scale. Localised structural damage, such as brittle failure of individual components or connections, as well as non-structural damage, may occur without significant whole-building residual deformation and may therefore not be adequately captured. Similarly, structures that experience substantial transient deformation but exhibit limited residual drift may have damage underestimated by this indicator. The inferred damage levels should therefore be interpreted as deformation-based estimates of damage severity rather than as a representation of all possible damage mechanisms.

It is also worth mentioning that, the rising number of government initiatives worldwide committed to the active collection of LiDAR data for diverse purposes, ranging from topographic mapping and land use planning to environmental monitoring and disaster management [49–53], suggests expanding opportunities for the wider application of this method in evaluating structural damage in the future.

2.6. CONCLUSION

This chapter presents a new methodology for the regional-scale quantitative assessment of earthquake-induced building damage using Remote Sensing (RS) airborne Light Detection and Ranging (LiDAR) point cloud data. The proposed method enables detection of moderate levels of damage, which are typically difficult to identify using other RS techniques. For the first time, building damage is quantified by integrating LiDAR-derived displacement measurements and a structural engineering parameter, the drift ratio. Using the Iterative Closest Point (ICP) registration approach, displacement measurements at the building and ground levels are used to estimate drifts and categorise damage levels from negligible to complete. The proposed methodology is applied to LiDAR data from the 2014 South Napa earthquake in California, demonstrating its effectiveness in detecting moderate levels of damage at a regional scale. The findings of the current study highlight the potential of using LiDAR-based displacement measurements in conjunction with structural analysis approaches for more efficient and more scalable post-earthquake damage assessment over large areas.

DATA AVAILABILITY

The datasets used in this research are a combination of publicly accessible and proprietary resources. Post-event airborne LiDAR data for the 2014 South

Napa earthquake are openly available through the OpenTopography Facility (https://doi.org/10.5069/G9F769H3), and the building footprint datasets utilised for structural identification were obtained from the Napa County GIS Open Data portal (https://gisdata.napacounty.gov/datasets/napacounty::buildingfootprint-public/about). Field observations and surface rupture data are available through the USGS (https://doi.org/10.3133/ofr20191018), while field photographic documentation can be accessed via the Earthquake Engineering Research Institute's Learning from Earthquakes archive (https://learningfromearthquakes.org/earthquakes/2014-08-24-south-napa/). The pre-event LiDAR data analysed in this study are commercial and are not publicly available due to third-party restrictions and may be subject to different licensing terms from the original provider.

References

[1] N. Tamkuan and M. Nagai. 'Fusion of multi-temporal interferometric coherence and optical image data for the 2016 Kumamoto earthquake damage assessment'. In: *ISPRS International Journal of Geo-Information* 6.7 (2017), p. 188. DOI: 10.3390/ijgi6070188.

[2] R. Anniballe, F. Noto, T. Scalia, C. Bignami, S. Stramondo, M. Chini and N. Pierdicca. 'Earthquake damage mapping: An overall assessment of ground surveys and VHR image change detection after L'Aquila 2009 earthquake'. In: *Remote Sensing of Environment* 210 (2018), pp. 166–178. DOI: 10.1016/j.rse.2018.03.004.

[3] S. Karimzadeh, M. Matsuoka, M. Miyajima, B. Adriano, A. Fallahi and J. Karashi. 'Sequential SAR coherence method for the monitoring of buildings in Sarpole-Zahab, Iran'. In: *Remote Sensing* 10.8 (2018), p. 1255. DOI: 10.3390/rs10081255.

[4] O. L. Stephenson, T. Köhne, E. Zhan, B. E. Cahill, S.-H. Yun, Z. E. Ross and M. Simons. 'Deep learning-based damage mapping with InSAR coherence time series'. In: *IEEE Transactions on Geoscience & Remote Sensing* 60 (2021), pp. 1–17. DOI: 10.1109/TGRS.2021.3084209.

[5] L. Moya, F. Yamazaki, W. Liu and M. Yamada. 'Detection of collapsed buildings from LiDAR data due to the 2016 Kumamoto earthquake in Japan'. In: *Natural Hazards and Earth System Sciences* 18.1 (2018), pp. 65–78. DOI: 10.5194/nhess-18-65-2018.

[6] W. Liu and F. Yamazaki. 'Extraction of collapsed buildings due to the 2016 Kumamoto, Japan, earthquake using two-temporal LiDAR data'. In: *Lidar Remote Sensing for Environmental Monitoring XVI*. Vol. 10779. SPIE. 2018, pp. 153–159. DOI: 10.1117/12.2324385.

[7] L. Saganeiti, F. Amato, G. Nolè, M. Vona and B. Murgante. 'Early estimation of ground displacements and building damage after seismic events using SAR and LiDAR data: The case of the Amatrice earthquake in central Italy, on 24th August 2016'. In: *International Journal of Disaster Risk Reduction* 51 (2020), p. 101924. DOI: 10.1016/j.ijdrr.2020.101924.

[8] E. Nissen, A. K. Krishnan, J. R. Arrowsmith and S. Saripalli. 'Three-dimensional surface displacements and rotations from differencing pre-and post-earthquake LiDAR point clouds'. In: *Geophysical Research Letters* 39.16 (2012). DOI: 10.1029/2012GL052460.

[9] S. Ghaffarian, N. Kerle and T. Filatova. 'Remote sensing-based proxies for urban disaster risk management and resilience: A review'. In: *Remote sensing* 10.11 (2018), p. 1760. DOI: 10.3390/rs10111760.

[10] R. C. Labiak, J. A. Van Aardt, D. Bespalov, D. Eychner, E. Wirch and H.-P. Bischof. 'Automated method for detection and quantification of building damage and debris using post-disaster LiDAR data'. In: *Laser Radar Technology and Applications XVI*. Vol. 8037. SPIE. 2011, pp. 145–152.

[11] D. Aixia, M. Zongjin, H. Shusong and W. Xiaoqing. 'Building damage extraction from post-earthquake airborne LiDAR data'. In: *Acta Geologica Sinica-English Edition* 90.4 (2016), pp. 1481–1489. DOI: 10.1111/1755-6724.12781.

[12] P. Dong and H. Guo. 'A framework for automated assessment of post-earthquake building damage using geospatial data'. In: *International journal of remote sensing* 33.1 (2012), pp. 81–100. DOI: 10.1080/01431161.2011.582188.

[13] E. Miranda and C. J. Reyes. 'Approximate lateral drift demands in multistory buildings with nonuniform stiffness'. In: *Journal of Structural Engineering* 128.7 (2002), pp. 840–849. DOI: 10.1061/(ASCE)0733-9445(2002)128:7(840).

[14] K. Dai, J. Wang, B. Li and H. Hong. 'Use of residual drift for post-earthquake damage assessment of RC buildings'. In: *Engineering Structures* 147 (2017), pp. 242–255. DOI: 10.1016/j.engstruct.2017.06.001.

[15] M. Gaetani d'Aragona, M. Polese, E. Cosenza and A. Prota. 'Simplified assessment of maximum interstory drift for RC buildings with irregular infills distribution along the height'. In: *Bulletin of Earthquake Engineering* 17.2 (2019), pp. 707–736. DOI: 10.1007/s10518-018-0473-y.

[16] A. Ghobarah. 'On drift limits associated with different damage levels'. In: *International Workshop on Performance-Based Seismic Design*. Vol. 28. Department of Civil Engineering, McMaster University, Ontario, Canada. 2004.

[17] FEMA. *Multi-hazard loss estimation methodology, earthquake model*. Tech. rep. Federal Emergency Management Agency, Washington, D.C., 2006.

[18] K. W. Hudnut, T. M. Brocher, C. S. Prentice, J. Boatwright, B. A. Brooks, B. T. Aagaard, J. L. Blair, J. Fletcher, J. E. Erdem, C. W. Wicks *et al. Key recovery factors for the August 24, 2014, South Napa earthquake*. Vol. 10. US Department of the Interior, US Geological Survey, 2014. DOI: 10.3133/ofr20141249.

[19] X. Zhang. 'LiDAR-based change detection for earthquake surface ruptures'. PhD thesis. University of Houston, May 2016. DOI: 10.1109/JSTARS.2015.2398317.

[20] A. Lydaa, X. Zhang, C. Glennie, K. Hudnut and B. Brooks. 'Airborne Light Detection and Ranging (LiDAR) derived deformation from the MW 6.0 24 August 2014 South Napa earthquake estimated by two and three dimensional point cloud change detection techniques'. In: *International Archives of the Photogrammetry, Remote Sensing & Spatial Information Sciences* 41 (2016). DOI: 10.5194/isprs-archives-XLI-B2-35-2016.

[21] C. P. Scott, J. R. Arrowsmith, E. Nissen, L. Lajoie, T. Maruyama and T. Chiba. 'The M7 2016 Kumamoto, Japan, earthquake: 3-D deformation along the fault and within the damage zone constrained from differential liDAR topography'. In: *Journal of Geophysical Research: Solid Earth* 123.7 (2018), pp. 6138–6155. DOI: 10.1029/2018JB015581.

[22] M. Raffel, C. E. Willert, J. Kompenhans *et al. Particle image velocimetry: A practical guide*. Vol. 2. Springer, 1998. DOI: 10.1029/2018JB015581.

[23] S. Mukoyama. 'Estimation of ground deformation caused by the earthquake (M7.2) in Japan, 2008, from the geomorphic image analysis of high-resolution LiDAR DEMs'. In: *Journal of Mountain Science* 8.2 (2011), pp. 239–245. DOI: 10.1007/s11629-011-2106-7.

[24] A. Borsa and J.-B. Minster. 'Rapid determination of near-fault earthquake deformation using differential LiDAR'. In: *Bulletin of the Seismological Society of America* 102.4 (2012), pp. 1335–1347. DOI: 10.1785/0120110159.

[25] L. Moya, F. Yamazaki, W. Liu and T. Chiba. 'Calculation of coseismic displacement from liDAR data in the 2016 Kumamoto, Japan, earthquake'. In: *Natural Hazards and Earth System Sciences* 17.1 (2017), pp. 143–156. DOI: 10.5194/nhess-17-143-2017.

[26] D. Ishimura, S. Toda, S. Mukoyama, S. Homma, K. Yamaguchi and N. Takahashi. '3D surface displacement and surface ruptures associated with the 2014 Mw 6.2 Nagano earthquake using differential LiDAR3D surface displacement and surface ruptures'. In: *Bulletin of the Seismological Society of America* 109.2 (2019), pp. 780–796. DOI: 10.1785/0120180020.

[27] P. J. Besl and N. D. McKay. 'Method for registration of 3-D shapes'. In: *Sensor Fusion IV: Control Paradigms and Data Structures*. Vol. 1611. Spie. 1992, pp. 586–606. DOI: 10.1117/12.57955.

[28] Y. Chen and G. Medioni. 'Object modelling by registration of multiple range images'. In: *Image and Vision Computing* 10.3 (1992), pp. 145–155. DOI: 10.1016/0262-8856(92)90066-C.

[29] T. Zieher, M. Bremer, M. Rutzinger, J. Pfeiffer, P. Fritzmann and V. Wichmann. 'Assessment of landslide-induced displacement and deformation of above-ground objects using UAV-borne and airborne laser scanning data'. In: *ISPRS Annals of Photogrammetry, Remote Sensing and Spatial Information Sciences* 4 (2019). DOI: 10.5194/isprs-annals-IV-2-W5-461-2019.

[30] Cal OES. *August 24, 2014 South Napa Earthquake*. 2014. URL: https://www.caloes.ca.gov/ (visited on 03/05/2015).

[31] USGS. *M 6.0 South Napa*. 2014. URL: https://earthquake.usgs.gov/earthquakes/eventpage/nc72282711/executive#summary (visited on 28/08/2017).

[32] T. M. Brocher, A. S. Baltay, J. L. Hardebeck, F. F. Pollitz, J. R. Murray, A. L. Llenos, D. P. Schwartz, J. L. Blair, D. J. Ponti, J. J. Lienkaemper *et al.* 'The Mw 6.0 24 August 2014 South Napa earthquake'. In: *Seismological Research Letters* 86.2A (2015), pp. 309–326. DOI: 10.1785/0220150004.

[33] D. J. Ponti, C. M. Rosa and J. L. Blair. *The Mw 6.0 South Napa earthquake of August 24, 2014—Observations of surface faulting and ground deformation, with recommendations for improving post-earthquake field investigations*. Tech. rep. US Geological Survey, 2019. DOI: 10.3133/ofr20191018.

[34] OpenStreetMap. 2023. URL: https://www.openstreetmap.org (visited on 01/06/2020).

[35] County of Napa. *GIS data catalog*. 2021. URL: https://gisdata.napacounty.gov/datasets/napacounty::buildingfootprint-public/about.

[36] EERI. *M 6.0 South Napa, California Earthquake of August 24, 2014*. Tech. rep. EERI, 2014. URL: https://lfestorage.s3.us-east-2.amazonaws.com/images/2014_08_24_south_napa/pdfs/EERI_EQ_report/EERI-Special-Eq-Report-2014-South-Napa-versionOct19web.pdf.

[37] J. Boatwright, J. L. Blair, B. T. Aagaard and K. Wallis. 'The distribution of red and yellow tags in the City of Napa'. In: *Seismological Research Letters* 86.2A (2015), pp. 361–368. DOI: 10.1785/0220140234.

[38] P. Heresi and E. Miranda. 'Fragility curves and methodology for estimating post-earthquake occupancy of wood-frame single-family houses on a regional scale'. In: *Journal of Structural Engineering* 147.5 (2021), p. 04021039. DOI: 10.1061/(ASCE)ST.1943-541X.0002989.

[39] OpenTopography. *August 24, 2014 South Napa Earthquake*. 2014. URL: https://doi.org/10.5069/G9F769H3 (visited on 03/05/2015).

[40] S. DeLong. '2014 South Napa Earthquake airborne liDAR reprocessing notes'. USGS Earthquake Science Center. 2014. DOI: 10.13140/RG.2.1.4248.7525.

[41] LAStools. *Efficient LiDAR Processing Software (version 1.4)*. 2019. URL: http://rapidlasso.com/LAStools.

[42] J. H. Friedman, F. Baskett and L. J. Shustek. 'An algorithm for finding nearest neighbors'. In: *IEEE Transactions on Computers* 100.10 (1975), pp. 1000–1006. DOI: 10.1109/T-C.1975.224110.

[43] A. Diederichs, E. Nissen, L. Lajoie, R. Langridge, S. Malireddi, K. Clark, I. Hamling and A. Tagliasacchi. 'Unusual kinematics of the Papatea fault (2016 Kaikōura earthquake) suggest anelastic rupture'. In: *Science Advances* 5.10 (2019), eaax5703. DOI: 10.1126/sciadv.aax5703.

[44] B. R. Ellingwood, D. V. Rosowsky and W. Pang. 'Performance of light-frame wood residential construction subjected to earthquakes in regions of moderate seismicity'. In: *Journal of Structural Engineering* 134.8 (2008), pp. 1353–1363. DOI: 10.1061/(ASCE)0733-9445(2008)134:8(1353).

[45] N. Ekhtari and C. Glennie. 'High-resolution mapping of near-field deformation with airborne Earth observation data, a comparison study'. In: *IEEE Transactions on Geoscience & Remote Sensing* 56.3 (2017), pp. 1598–1614. DOI: 10.1109/TGRS.2017.2765601.

[46] C. L. Glennie, A. Hinojosa-Corona, E. Nissen, A. Kusari, M. E. Oskin, J. R. Arrowsmith and A. Borsa. 'Optimization of legacy liDAR data sets for measuring near-field earthquake displacements'. In: *Geophysical Research Letters* 41.10 (2014), pp. 3494–3501. DOI: 10.1002/2014GL059919.

[47] H. Butler, B. Chambers, P. Hartzell and C. Glennie. 'PDAL: An open source library for the processing and analysis of point clouds'. In: *Computers & Geosciences* 148 (2021), p. 104680. DOI: 10.1016/j.cageo.2020.104680.

[48] N. Cenni, S. Fiaschi and M. Fabris. 'Integrated use of archival aerial photogrammetry, GNSS, and InSAR data for the monitoring of the Patigno landslide (Northern Apennines, Italy)'. In: *Landslides* 18 (2021), pp. 2247–2263. DOI: 10.1007/s10346-021-01635-3.

[49] OpenTopography. *Find Topography Data*. 2024. URL: https://portal.opentopography.org/datasets.

[50] USGS. *USGS*. 2024. URL: https://www.usgs.gov/faqs/what-lidar-data-and-where-can-i-download-it.

[51] NEON. *National Ecological Observatory Network, Explore Data Products*. 2024. URL: https://data.neonscience.org/data-products/explore.

[52] Natural Resources Canada. *Natural Resources Canada*. 2024. URL: https://natural-resources.canada.ca/home.

[53] European Data. *European Data*. 2024. URL: https://data.europa.eu/en.

3

INSAR-BASED FRAMEWORK FOR MULTI-LEVEL BUILDING DAMAGE CLASSIFICATION AFTER EARTHQUAKES

Synthetic Aperture Radar (SAR) has gained prominence for post-earthquake damage assessment due to its ability to acquire high-resolution imagery under all weather and lighting conditions. However, most existing SAR-based studies rely on binary Machine Learning (ML) classification, distinguishing only between collapsed and intact buildings, while moderate damage is typically overlooked. Although some recent studies have explored multi-level damage classification, their effectiveness is often limited by the lack of physically meaningful indicators, such as displacement, that represent earthquake-induced deformation and can be directly linked to structural response and damage. To address this limitation, this chapter proposes the first implementation of an ML framework that integrates displacement information derived from SAR Interferometry (InSAR), providing a more direct and accurate measure of earthquake-induced structural deformation that can be related to structural response and damage. A supervised learning model is developed using InSAR-derived displacement and coherence metrics, together with structural and site-related features. Two progressive components are implemented: (i) a region-specific learning scheme, in which models are trained and tested on individual earthquake events, and (ii) a combined learning scheme that integrates data from multiple events to assess the model's ability to generalise across regions. The proposed framework is applied to post-event datasets from the 2015 Nepal earthquake and the 2016 Central Italy earthquake sequence. Results demonstrate the effectiveness of InSAR features in

The work presented in this chapter was published in Foroughnia, F., Macchiarulo, V. and Giardina, G., 2026. Multi-Level Earthquake Damage Assessment Using InSAR-Derived Displacement. *International Journal of Disaster Risk Reduction*, p.106333

multi-class damage mapping. Region-specific models effectively capture event-driven damage patterns, while cross-event analyses indicate robust performance across the three studied earthquakes. These findings highlight the potential of InSAR-driven ML approaches as reliable and scalable tools for rapid post-earthquake damage assessment and improved disaster response.

3.1. Introduction

As discussed in chapters 1 and 2, rapid and regional-scale assessment of earthquake-induced building damage is essential for supporting post-disaster response, while conventional field investigations are constrained by the time, resources, and accessibility required to inspect large affected areas. Remote Sensing (RS) provides a means of extending damage assessment spatially, with optical imagery, Synthetic Aperture Radar (SAR), and airborne Light Detection and Ranging (LiDAR) offering complementary information for identifying earthquake-induced impacts.

Chapter 2 investigated this potential using high-resolution pre- and post-event LiDAR observations, demonstrating how three-dimensional building displacements can be translated into residual drift measures for quantitative assessment of structural damage. However, the applicability of such an approach depends on the availability of suitable pre- and post-event LiDAR acquisitions, which remains limited for many earthquake-affected regions. This chapter, therefore, shifts the focus to spaceborne SAR observations as a more widely available source of remotely sensed information for regional-scale building damage assessment. In addition to the general advantages of SAR for large-scale and timely observation discussed in Chapter 1, its increasing availability provides an opportunity to investigate scalable approaches for assessing building damage across different earthquake-affected regions.

SAR sensors transmit microwave pulses towards the Earth's surface, a portion of which is reflected back to the sensor [1, 2]. The resulting SAR observations contain amplitude and phase information [3]. The amplitude represents the strength of the returned signal, while the phase contains information related to the distance travelled by the signal between the sensor and the ground [4]. Backscatter intensity is derived from the amplitude information and has been used to detect earthquake-induced surface changes, including collapsed structures and debris [5, 6]. Phase information, in turn, enables interferometric measurements of ground displacement and the computation of coherence, which quantifies the correlation between radar signals acquired at different times [7, 8]. A significant reduction in coherence following an earthquake can indicate substantial changes in the scattering characteristics associated with building collapse or severe structural damage [4, 9, 10].

As reviewed in Chapter 1, imaged-based approaches commonly employ change detection based on pre- and post-event SAR observations, particularly changes in backscatter intensity and coherence [5, 11–13]. These approaches use ratios, differences, and statistical measures of the radar observations to identify changes associated with building damage. While effective in many cases, they can be sensitive to image quality and threshold selection and may perform poorly in heterogeneous urban environments.

To address these challenges, recent studies have increasingly adopted advanced classification techniques. Leveraging high-performance computing, open-source libraries, and Machine Learning (ML) has driven substantial progress in automating and enhancing post-earthquake damage detection based on SAR imagery [14]. Different ML classifiers, such as Random Forest (RF), Support Vector Machines (SVMs), and K-Nearest Neighbour (K-NN), have been adopted for building damage assessment using statistical [15] or textural features [8] of Very High-Resolution (VHR) SAR imagery. However, most of these studies have primarily focused on binary classification, distinguishing between collapsed and standing buildings, while overlooking intermediate damage levels, such as moderate damage, which are more difficult to identify [16, 17]. Slight-to-moderate damage often does not produce visually distinct changes, such as variations in roof geometry or surface scattering properties, that can be easily detected in SAR imagery. Consequently, classification models that rely solely on features such as backscatter intensity, texture, and coherence tend to overlook subtle structural damage, thereby limiting their effectiveness in accurately classifying multi-level damage [18]. Additionally, because many of these models rely solely on SAR data, they neglect other influential factors, such as soil conditions, ground slope, and seismic intensity, which significantly affect the extent and distribution of building damage [19].

To overcome these limitations, recent studies have explored multi-level damage classification frameworks that integrate radar observations with additional contextual and structural information, including building typology, age, area, and traditional seismic indicators such as Peak Ground Velocity (PGV) and Peak Ground Acceleration (PGA). Within these efforts, SAR-derived features, such as coherence-based Damage Proxy Maps (DPMs) [14] and amplitude measures [19], have become central for characterising multi-level damage patterns. However, the effectiveness of these SAR-focused frameworks remains constrained by their reliance on ground-based seismic metrics, which are often spatially sparse or entirely unavailable in many affected regions. This dependence limits their capacity to provide consistent, high-resolution assessments, reinforcing the need for alternative features that can also independently capture fine-grained variations in damage severity.

A promising yet underexplored alternative is ground displacement derived from Differential SAR Interferometry (D-InSAR), hereafter simply referred to as InSAR. This technique estimates ground displacement induced by an earthquake by analysing phase differences between SAR images acquired before and after an earthquake [3, 20, 21]. Unlike commonly used SAR-based features, such as backscatter intensity, coherence, and texture, InSAR-derived displacements offer a direct representation of ground earthquake-induced ground deformation. This is particularly valuable for detecting slight-to-moderate building damage [18], which often lacks visually distinct surface indicators yet is mechanically linked to underlying displacement patterns.

Recent studies have demonstrated that co-seismic ground displacements derived from InSAR correlate well with building damage patterns following earthquakes [22–25]. For example, [25] developed a quantitative method to extract horizontal building deformations in the earthquake direction using InSAR, showing that the magnitude of displacement directly correlated with the severity of structural damage observed in high-resolution optical imagery. While such studies clearly demonstrate the relevance

of InSAR-derived displacement for timely post-earthquake assessment, its integration into an ML framework for post-earthquake building damage assessment as a physically interpretable representation of earthquake-induced deformation has not yet been explored.

In this study, we developed a multi-class ML framework that uses InSAR-derived displacement and coherence maps to assess earthquake-induced building damage. The input features fed into the ML system included co-seismic displacements, co-seismic coherence, ground surface slope, and site-related properties, which were then combined with structural attributes to classify the building damage level. The framework categorises buildings into three damage classes: No Damage (no to slight structural damage), Moderate, and Severe (significant damage, partial collapse, or collapse). To evaluate the effectiveness of the proposed InSAR-based approach, we compared its performance with models that rely on conventional seismic indicators, such as PGV and PGA. By comparing classification metrics across InSAR-derived and traditional seismic features, we examined whether InSAR can provide comparable or complementary information on damage patterns. This comparison assesses the potential of InSAR as an alternative source of information in areas where seismic recordings are unavailable.

We applied the proposed method to three distinct earthquake events: the 2015 Gorkha earthquake in Nepal and the 2016 Central Italy earthquake. These events encompass a range of seismic impacts, building typologies, and damage distributions. Pre- and post-event Sentinel-1 images were utilised for InSAR analysis to generate co-seismic displacement and coherence maps for these regions. Observed building damage data obtained from post-earthquake field assessments were used as the target labels for supervised classification. For each region of interest, ML models were trained on a subset of data and evaluated on the corresponding test datasets. Given the imbalanced nature of the damage datasets and the inherent class overlaps, we implemented targeted strategies within the learning pipeline to improve classification performance. A combined learning model was also trained on all three regional datasets to evaluate the generalisation capability of the proposed framework across different seismic events. This multi-event training strategy offers insight into the scalability and operational potential of InSAR-enhanced damage assessment models for future earthquakes.

3.2. CASE STUDIES

We evaluated the proposed ML framework for multi-class building damage classification across urban regions affected by three earthquake events: the 2016 Amatrice and Norcia earthquakes in Central Italy and the 2015 Gorkha earthquake in Nepal. These events were chosen because they collectively represent a wide range of conditions relevant to model evaluation. They include multiple levels of building damage, large affected areas, and diverse building typologies and construction materials, providing a robust basis to assess the model's ability to accurately capture structural damage. Furthermore, comprehensive SAR datasets are available for these events, facilitating the detailed extraction of displacement-based features. Figure 3.1 shows the location of the earthquake events and the corresponding extent of building damage.

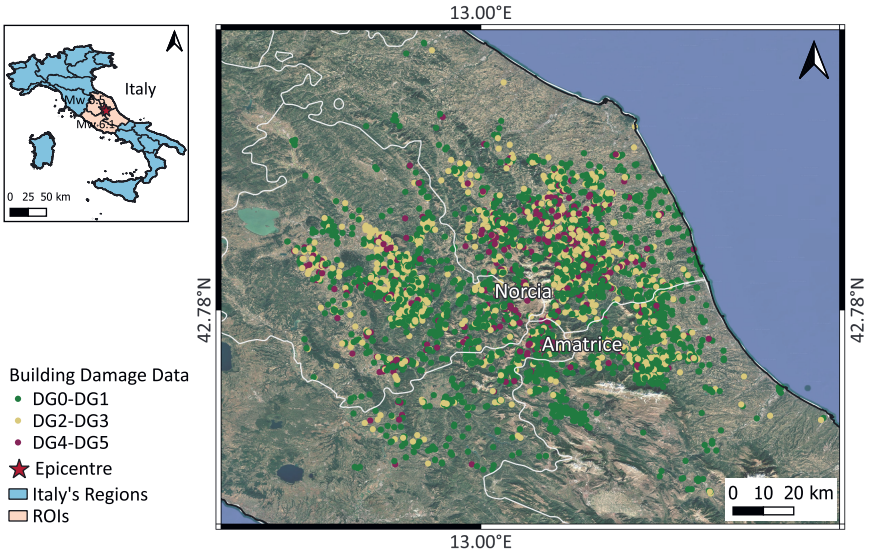

(a)

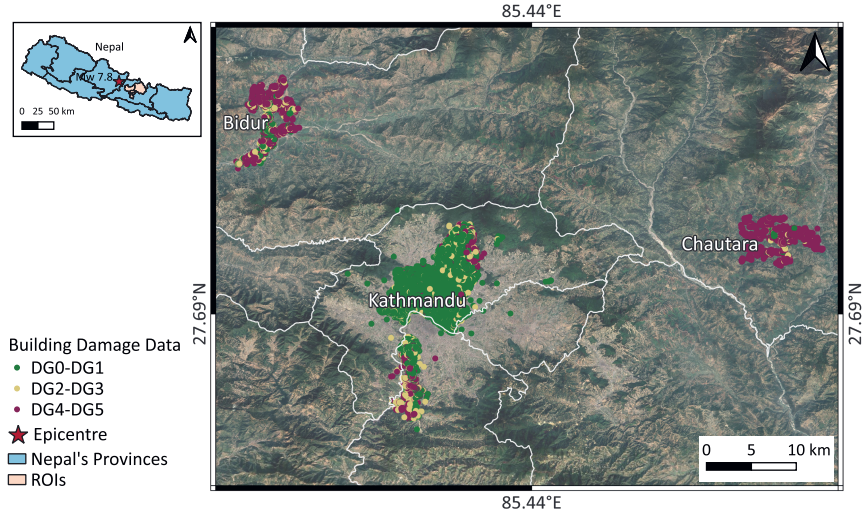

(b)

Figure 3.1.: Study areas and the distribution of building damage data for the (a) Central Italy and (b) Gorkha, Nepal earthquake events. Damge grades: DG0–DG1, No Damage; DG2–DG3, Moderate Damage; DG4–DG5, Severe Damage classes.

3.2.1. The 2016 Central Italy earthquake events

The 2016 Central Italy earthquakes began on August 24 with a moment magnitude (Mw) 6.1 event near Amatrice, located in a high seismic strain zone of the Apennines [26], causing around 300 fatalities and severe damage to the region [27]. Following the Amatrice earthquake, a surface rupture extending ~5.2 km was mapped, showing an average displacement of about 13 cm [26]. Aftershocks continued until late October, when a Mw 6.5 earthquake struck near Norcia on 30 October, affecting the area between the previous ruptures. Although other events occurred in late October, before the Norcia earthquake, they were excluded from this study due to their lower magnitudes. For this analysis, only the Amatrice and Norcia earthquakes were selected, as both had a Mw of 6 or greater.

3.2.2. The 2015 Gorkha earthquake

On 25 April 2015, a Mw 7.8 earthquake struck central Nepal, with its epicentre located near Gorkha, approximately 80 km northwest of Kathmandu [28]. The quake ruptured west to east along a shallowly dipping fault [29], resulting in intense ground shaking in Kathmandu and surrounding municipalities [28]. The mainshock caused widespread destruction of infrastructure and buildings in both urban and rural areas, triggered landslides that blocked roads, and disrupted rescue operations. Significant aftershocks also caused further damage in northern Central Nepal [28]. By 26 May 2015, the earthquake had resulted in 8,510 deaths and 199 missing people, with an additional 163 fatalities following a major aftershock on 12 May [28]. Both the mainshock and the aftershocks were analysed.

3.3. Datasets

This section outlines the datasets used for the analysis, including SAR images, building characteristics, building damage data, and site-related parameters, such as slope, soil type, and distance to the epicentre.

3.3.1. SAR images

Sentinel-1 Single Look Complex (SLC) Interferometric Wide (IW) swath images were used to generate coherence and displacement maps. The Sentinel-1 mission, operated by the European Space Agency (ESA), offers global SAR coverage with a revisit time of up to six days [30], enabling timely monitoring of seismic events. The IW mode acquires data using the Terrain Observation by Progressive Scans SAR (TOPSAR) technique, providing a swath width of approximately 250 km and a spatial resolution of 5×20 m in range and azimuth, respectively. Vertical–Vertical polarisation (VV) polarised images acquired from both ascending and descending geometries were used, with data collected before and after each earthquake event described in Section 3.2. For Amatrice and Norcia, coherence and displacement maps were generated using InSAR data spanning the mainshock events. In Nepal, these maps were produced for both the mainshock and aftershock due to the significant magnitude of the latter. In this case, the post-mainshock image also served as the pre-aftershock image for the analysis. Table 3.1 reports the information about the

SAR data used in this study to create InSAR-derived features. Note that for the Amatrice ascending geometry, two consecutive image frames acquired on the same date were used to ensure complete coverage of the affected area.

3.3.2. BUILDING DAMAGE DATA

Building damage data for the Central Italy earthquakes were obtained from the Database of Observed Damage (DaDO), openly available through a web-based Geographic Information System (GIS) platform [31]. The DaDO is designed to compile and disseminate information on building characteristics, seismic ground motions, and observed earthquake damage to ordinary buildings and churches across Italy for events from 1976 to 2019. Only data from ordinary buildings collected after the Central Italy earthquakes were considered. The database applies a standardised framework to harmonise the collected data and to convert damage observations to the European Macroseismic Scale 1998 (EMS-98) [32], following the methodology of [33]. The EMS-98 damage grades, which range from DG0 (no damage) to DG5 (total collapse), are grouped into four categories: no damage (DG0), slight damage (DG1), moderate damage (DG2–DG3), and severe damage (DG4–DG5). The damage feature used for the analysis corresponds to damage observed in vertical structural elements. The distribution of damage data across Central Italy is shown in Figure 3.1a. The dataset also provides detailed information on building characteristics and structural configuration, from which the attributes were selected.

The building damage data for the Gorkha earthquake was obtained from the National Society for Earthquake Technology–Nepal (NSET). The collection of these data was supported by the Public Private Partnership for Earthquake Risk Management (3PERM) program. The assessment involved collecting and analysing detailed building information, including construction practices, typology, footprint, age, number of storeys, and damage grades. The survey covered all private buildings within the municipal

Table 3.1.: SAR imagery acquisition information for the earthquake regions shown in Figure 3.1. (M) and (A) refer to the Mainshock and Aftershock events in Gorkha, Nepal, respectively.

Earthquake	**Orbit**	**Path**	**Satellite**		**Acquisition date**	
			Pre	**Post**	**Pre**	**Post**
Amatrice 24-08-2016	Ascending	44	S-1A	S-1B	22-08-2016	28-08-2016
	Descending	22	S-1A	S-1B	21-08-2016	27-08-2016
Norcia 30-10-2016	Ascending	44	S-1A	S-1A	27-08-2016	08-11-2016
	Descending	22	S-1B	S-1A	26-10-2016	01-11-2016
Gorkha (M) 25-04-2015	Ascending	85	S-1A	S-1A	16-03-2015	03-05-2015
	Descending	19	S-1A	S-1A	17-04-2015	29-04-2015
Gorkha (A) 12-05-2015	Ascending	85	S-1A	S-1A	03-05-2015	15-05-2015
	Descending	19	S-1A	S-1A	29-04-2015	04-06-2015

boundaries, excluding government and institutional structures. In total, 188,430 buildings were evaluated. The assessments were conducted after the full earthquake sequence, including the mainshock and subsequent aftershocks, and therefore represent the final cumulative damage state of each building. A single overall damage grade was assigned to each building following field inspection. Damage assessment followed the EMS-98 scale, with grades ranging from DG0 (no damage) to DG5 (total collapse). Unlike the Central Italy dataset, in which DG2–DG3 and DG4–DG5 were already grouped as moderate and severe damage, respectively, the Gorkha dataset reported the individual damage grades. The spatial distribution of building damage for the Gorkha earthquake is illustrated in Figure 3.1b.

Based on the information available for the case studies, the following common building attributes were considered as input features in the classification models:

- Building age: the time difference between the year of the earthquake and the year of building construction;
- Building typology: categories included Reinforced Concrete (RC) structures, good- and poor-quality masonry, wood structures, adobe, steel frame, and mixed-frame buildings. The distinction between good- and poor-quality masonry was provided in both datasets and was retained as reported, without imposing a common quality definition. For the Italian dataset, poor-quality masonry refers to masonry with irregular texture and poor construction quality, typically consisting of unsquared stone or cobbles. In contrast, good-quality masonry refers to regularly arranged masonry of better construction quality, such as blocks, bricks, or squared stone. Mixed-frame buildings correspond to structures in which masonry and framed structural systems coexist, including configurations with frames above masonry, masonry above frames, or masonry and frames acting in parallel on the same storeys. In the Italian dataset, this typology was classified as either good or poor quality. The good- and poor-quality distinction for mixed-frame buildings was retained from the dataset and reflects the quality classification of the associated masonry component.
- Building floor surface: average storey surface area.
- Number of storeys: total number of floors above the ground surface.

3.3.3. Site-related datasets

To incorporate the influence of local soil conditions, we used the time-averaged shear-wave velocity to 30 m depth (Vs30) [34]. Global Vs30 datasets are publicly accessible via the United States Geological Survey (USGS) [35]. We also incorporated the distance to the epicentre and ground surface slope using the 30-m-resolution Copernicus Digital Elevation Model (DEM) downloaded from [36].

3.4. Methodology

We propose a multi-class ML framework for classifying building damage levels in the immediate aftermath of an earthquake, with a particular focus on InSAR-derived

information. The approach specifically addresses the challenges of multi-level damage assessment, including class imbalance, overlapping damage categories, and the need to capture the gradual physical differences between damage levels. Class imbalance arises when certain damage categories contain far more samples than others, causing models to favour the majority classes. Overlapping damage categories occur when different damage levels share similar features, making them difficult to separate accurately. The framework integrates InSAR-derived displacements and coherence with structural and site-related information to create a detailed, physically informed representation of earthquake impacts at the building scale. The processing and preparation of input features for classification are described in Section 3.4.1. The framework consists of two progressive components:

1. **Region-specific learning:** Independent models were developed for each earthquake event, enabling region-specific classification. This design enables the exploration of how InSAR features interact with structural and site-related variables, such as soil, slope, and proximity to the epicentre, under various seismic conditions. It also includes strategies to address class imbalance and category overlap, ensuring robust performance across regions (Section 3.4.2).

2. **Combined learning across regions:** To evaluate the framework's generalisation capability, all available datasets from different earthquake events were merged into unified training and testing sets. This step assesses scalability across diverse regions, structural typologies, and seismic characteristics, assessing the framework's potential for region-independent earthquake damage assessment (Section 3.4.3).

Figure 3.2 outlines the overall methodology. A detailed description of each component, including data preparation, processing steps, and performance evaluation, is provided in the following sections.

3.4.1. DATA PREPARATION

A critical component of the proposed framework is the development of a physically meaningful and internally consistent feature set that integrates InSAR-derived displacement and coherence data with structural and site-related attributes. To prepare the input features for the subsequent classification, several processing steps were performed. These included applying InSAR techniques to SAR imagery to generate displacement and coherence maps, performing atmospheric correction on the obtained displacement data, and preparing labelled datasets of structural and damage information.

3.4.1.1. INSAR DISPLACEMENT

InSAR-derived displacements are directly related to earthquake-induced damage, as they represent the ground deformation experienced by structures during seismic events. InSAR processing was conducted to measure ground surface displacement associated with each event. All SAR image pairs were co-registered prior to interferogram generation to ensure precise pixel alignment between acquisitions. Interferograms were generated

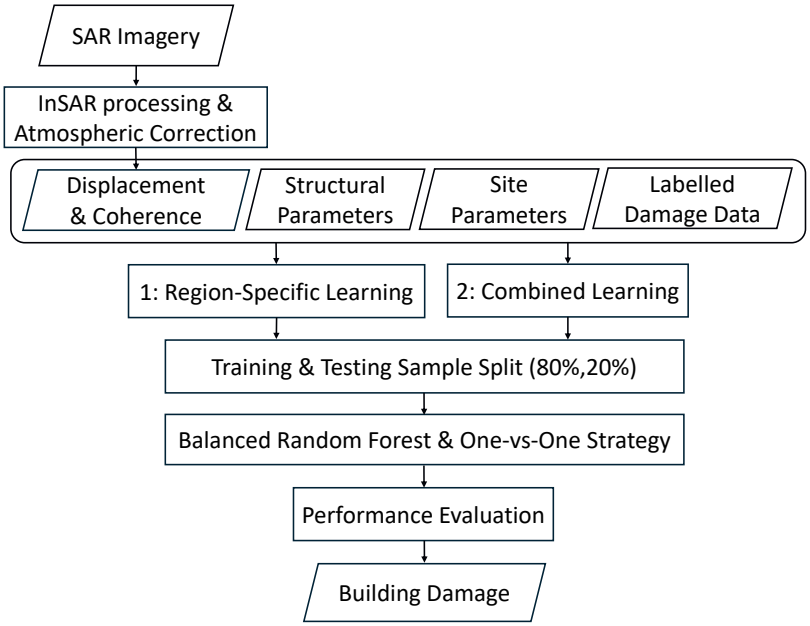

Figure 3.2.: Flowchart of the proposed methodology.

by multiplying the complex conjugate of the post-event SLC (secondary) image with the pre-event SLC (primary) image [37]. These interferograms represent the interferometric phase, which is the phase difference between the two SAR acquisitions obtained over the same area before and after the earthquake and from slightly different satellite positions [38, 39]. To reduce speckle noise and improve phase estimation, the primary and secondary images were multilooked with factors of 10×2 (range × azimuth), resulting in interferograms with an approximate ground range resolution of 80 m and a pixel spacing of 40 m. To isolate the displacement signal due to the earthquake, unwanted phase contributions were removed from the interferometric phase. The Earth's curvature contribution was corrected using the satellite imaging geometry. At the same time, the topographic phase component was removed prior to displacement estimation using an external DEM, thereby accounting for topographic effects during interferogram formation [20]. Although atmospheric and noise contributions are typically ignored, assuming their impact is minimal relative to the displacement signal, we corrected for atmospheric effects using the methodology described below.

We applied the Goldstein–Werner Adaptive Phase Filter (AdF) [40] with a threshold of 0.6 to enhance fringe visibility and reduce phase noise before unwrapping. Since the interferometric phase is inherently wrapped within the $[-\pi,\pi]$ interval, phase ambiguities arise whenever the actual phase change exceeds a single 2π cycle, which is common in cases of large displacements [41]. To reconstruct the continuous phase field from these wrapped values [42], phase unwrapping was performed using the Minimum Cost Flow

(MCF) algorithm implemented in the GAMMA software package [43]. The unwrapped phase was subsequently converted into Line-of-Sight (LOS) displacements, providing pixel-wise measurements of ground displacement between the two acquisition dates [40]. These measurements were calculated relative to a reference point, identified as the pixel with the highest coherence. To determine this reference, the corresponding coherence map (see Section 3.4.1.2) was evaluated to locate all pixels with maximum coherence, and each candidate was assessed within a 9-pixel window. The reference point was the pixel with the highest cumulative coherence within its window; if multiple pixels shared the same value, the pixel closest to the origin (bottom-left for ascending scenes, top-right for descending scenes) was selected.

As discussed, a known limitation of the InSAR technique is that atmospheric effects remain in the interferometric phase and are often ignored rather than removed, which can introduce significant errors in displacement measurements [44]. To address this limitation, we corrected the displacement measurements for atmospheric delays using the Generic Atmospheric Correction Online Service (GACOS). GACOS provides Zenith Total Delay (ZTD) maps by employing the Iterative Tropospheric Decomposition (ITD) model [45, 46], which separates stratified and turbulent components within tropospheric delays. After generating the ZTD maps corresponding to the acquisition dates of the ascending and descending SAR images, additional post-processing steps were performed to prepare the atmospheric correction:

Temporal differencing The ZTD maps from the two acquisition dates (Z) were differenced to obtain the relative delay per geometry:

$$D_{(\text{date1,date2})} = Z_{\text{date2}} - Z_{\text{date1}} \tag{3.1}$$

Spatial referencing The delay maps were spatially differenced for each pixel i using the same reference point employed in the InSAR phase processing to ensure consistency in phase referencing. Consider a reference point R with coordinates (lon_R, lat_R), the spatially differenced delay at pixel i is given by:

$$SD(lon_i, lat_i) = D(lon_i, lat_i) - D(lon_R, lat_R) \tag{3.2}$$

Projection to LOS direction The zenith delays were projected into the LOS direction using the following equation:

$$Z_{LOS} = SD \cdot \cos(\theta) \tag{3.3}$$

where θ is the local incidence angle in radians.

LOS displacement correction If the interferogram was estimated using a later date (secondary image) minus an earlier one (primary image), LOS displacements $Disp_{LOS}$ were corrected by removing the projected zenith delays Z_{LOS}:

$$\widehat{Disp}_{LOS} = Disp_{LOS} - Z_{LOS} \tag{3.4}$$

Atmospherically corrected displacements in the LOS direction ($\widehat{Disp}_{LOS}$) for both ascending and descending geometries were used as InSAR-derived displacement features for subsequent damage classification. Figure A.1 in Appendix A shows the LOS displacement maps after atmospheric correction for both ascending and descending geometries obtained from the InSAR processing for the regions of interest. Each pixel of the displacement maps indicates a change in distance along the LOS between pre- and post-event acquisitions. Positive values, which are shown in blue tones, show displacements toward the satellite, while negative values, shown in red tones, indicate displacements away from the satellite.

3.4.1.2. InSAR coherence

Coherence provides a complementary source of information for earthquake damage assessment by quantifying the similarity of the radar signal between pre- and post-event acquisitions [39, 47]. Areas experiencing significant structural changes, such as building collapse or heavy debris deposition, typically exhibit a loss of coherence, appearing as low-coherence zones in the post-earthquake scene [48, 49]. Conceptually, coherence is valuable because it captures changes in surface scattering properties that are not always reflected in displacement fields. By integrating coherence alongside displacement, the framework leverages both the mechanistic link to structural loading (displacement) and the observational evidence of surface disruption (coherence), providing a more comprehensive basis for classifying building damage.

Coherence reflects the temporal stability of the SAR backscatter from ground targets, with values ranging from 0 (complete decorrelation) to 1 (perfect correlation). High coherence values indicate that the scattering properties of the ground surface have remained stable between acquisitions, resulting in reliable phase measurements. In contrast, low coherence suggests significant changes in surface scattering due to large surface displacement and earthquake-induced damage [48, 49].

Coherence is estimated by calculating the normalised cross-correlation of the complex SAR signals within a local window around each pixel across the pre-event and post-event images [50]. Mathematically, it is expressed as:

$$\gamma = \frac{\left|\langle s_1 s_2^* \rangle\right|}{\sqrt{\langle |s_1|^2 \rangle \langle |s_2|^2 \rangle}} \tag{3.5}$$

where s_1 and s_2 are the complex pixel values of the pre-event and post-event SAR images, s_2^* denotes the complex conjugate, and the angled brackets represent local averaging over a defined window to reduce speckle noise.

Co-seismic coherence maps were generated during the InSAR processing chain described in Section 3.4.1.1. InSAR displacement and coherence maps were generated through the Alaska Satellite Facility (ASF) platform [51], which enables on-demand processing of Sentinel-1 data [52] and delivers pre-processed displacement and coherence maps rapidly via cloud computing.

3.4.1.3. LABELLED DAMAGE AND STRUCTURAL DATA PREPARATION

As the Central Italy earthquakes consisted of multiple events, the building damage observations were filtered spatially and temporally to isolate those corresponding to the Amatrice and Norcia events. For Amatrice, observations from August 24 to October 26, 2016, were used, while for Norcia, data from October 30, 2016, to January 17, 2017, were considered.

Structural, InSAR-derived, and site-related features were extracted for each building observation location and stored in a tabular format, with each row representing an observation and each column representing a feature. The data for all three regions were organised using this structure. Missing values and duplicate entries were removed during data preparation to ensure data quality and consistency. For cases with identical spatial coordinates (X, Y), only a single record was retained (the first occurrence) to enforce a one-to-one correspondence between each location and its damage label, reducing label ambiguity and improving alignment with the spatial resolution of the InSAR-derived features. For model training, the damage categories of both datasets were further harmonised into three common classes: No Damage (DG0–DG1), Moderate Damage (DG2–DG3), and Severe Damage (DG4–DG5). These labels were prepared consistently across all regions to maintain comparability in model training. The distribution of damage levels across building typologies for the three regions is presented in Figure 3.3. RC structures and good-quality masonry buildings consistently experienced lower levels of damage compared to poor-quality masonry constructions. This trend is observed across all three events, highlighting the critical role of construction quality in determining seismic damage to buildings. The distribution of the three damage classes across the rest of the features is illustrated in the feature space in Figures A.2, A.3, and A.4 in Appendix A. These plots provide a visual representation of how damage severity correlates with seismic (i.e., InSAR-derived) features, building characteristics, and site-related factors for each earthquake region.

Before model training, feature preprocessing was conducted to prepare the data for analysis. Numerical features were standardised using z-score normalisation [53] via the StandardScaler function in Python scikit-learn library [54], to produce data with a mean of zero and a standard deviation of one. This step ensures that variables with different physical units and scales are directly comparable, improves numerical stability during model training, and reduces potential bias from features with larger magnitudes while maintaining consistency across cross-validation folds and different geographical regions. The categorical feature (building typology) was one-hot encoded. One-hot encoding is a technique that converts categorical variables into a binary vector format, where each category is represented by a unique combination of zeros and a single one, with one indicating the presence of the category and zero indicating its absence [54].

3.4.2. REGION-SPECIFIC LEARNING

A multi-class classification framework was developed to assess building damage for each region individually, implementing a region-specific learning strategy to capture patterns unique to each seismic scenario. Separate models were trained and evaluated using randomly selected data from each region, allowing the algorithm to focus on locally relevant structural typologies, construction practices, and seismic responses.

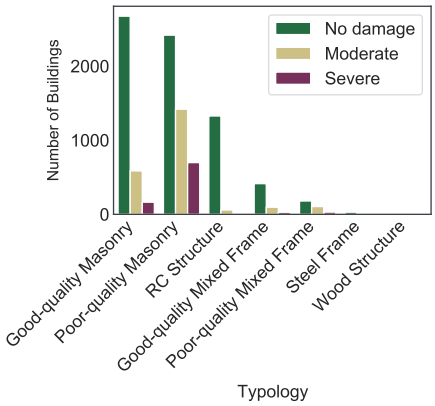

(a) Amatrice

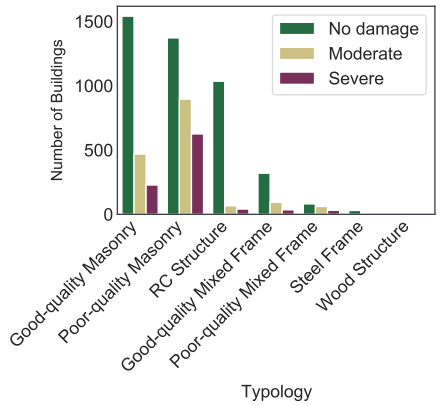

(b) Norcia

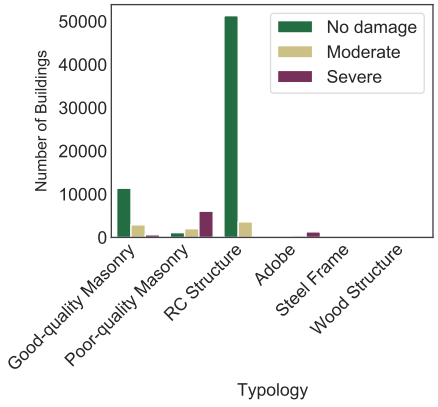

(c) Nepal

Figure 3.3.: Distribution of damage classes across different building typologies for (a) Amatrice, (b) Norcia, and (c) Nepal.

This region-specific learning approach allows the models to adapt to local building characteristics and seismic conditions and to capture damage patterns specific to each regional context.

To classify the building damage levels, an RF classifier was trained using InSAR-derived features combined with structural and site-related parameters. We selected RF due to its strong performance in handling complex, high-dimensional data [55] and its demonstrated effectiveness in previous building damage classification studies [8, 56]. RF is also particularly well-suited for applications involving highly imbalanced class distributions, common in post-earthquake damage datasets, where the No Damage class often dominates. Prior research has also demonstrated RF's robustness in similar settings, where it consistently outperformed other ML algorithms for damage prediction tasks [14, 57], further justifying its selection for this study.

Multiple train-test splits (80%–20%) were applied to each regional dataset to assess the stability of model performance across different data partitions and ensure a robust evaluation. Within the 80% training portion, hyperparameter tuning was conducted using a grid search within a nested cross-validation framework to optimise key parameters of the classification models and reduce bias in performance estimates. Nested cross-validation was implemented with five outer folds and three inner folds. The grid search targeted critical hyperparameters, including the number of trees, the minimum number of samples required to split an internal node, and the minimum number of samples required to reach a leaf node. Within the OvO framework, hyperparameter optimisation was further performed independently for each pairwise classifier, allowing the RF configuration to adapt to the characteristics of each pair of damage classes. Consequently, the selected hyperparameter values varied across pairwise classifiers and models. The selected optimal values ranged from 50 to 200 for the number of trees, 2 to 12 for the minimum number of samples required to split an internal node, and 1 to 8 for the minimum number of samples required at a leaf node. All other hyperparameters were retained at their default scikit-learn settings.

The framework explicitly addresses two major challenges in supervised, data-driven earthquake damage classification: class imbalance, where certain damage levels are underrepresented, and overlapping damage categories, which reduce separability and make accurate classification more difficult. These challenges primarily arise in the labelled training data, where severe damage cases are less frequent, and damage grades exhibit gradual transitions rather than sharp boundaries. To address these challenges, a Balanced Random Forest (BRF) was employed to counteract class imbalance (Section 3.4.2.1). In contrast, a One-vs-One (OvO) multi-class strategy was implemented to enhance the model's ability to distinguish closely related damage classes (Section 3.4.2.2). This combination ensures that the framework not only captures general damage patterns but also enhances the model's ability to detect underrepresented and ambiguous damage categories, strengthening predictive performance across heterogeneous seismic contexts.

3.4.2.1. BALANCED RANDOM FOREST (BRF) CLASSIFIER

To address the class imbalance inherent in damage datasets, this study employed the BRF algorithm [58]. BRF extends the classical RF framework by modifying the bootstrap sampling procedure used to train individual decision trees. In standard RF, each tree is trained on a bootstrap sample drawn from the training set and the final classification is obtained by majority voting across all trees [59]. Although this strategy improves generalisation, the bootstrap samples tend to reflect the original class distribution. In imbalanced datasets, this can lead to model bias toward majority classes and reduced performance for minority classes.

BRF addresses this limitation by enforcing balanced class representation within the training data of each tree. During tree construction, all available samples from the minority class are retained. An equal number of samples is randomly drawn from the remaining classes to form balanced bootstrap subsets [58]. In this study, the sampling strategy was set to "not minority". Under this setting, only the non-minority classes were resampled, while all minority-class samples were always included. This design preserves all information from underrepresented damage categories while reducing the dominance

of the No Damage class. The prevalence of the No Damage class across the datasets reflects the spatial distribution of earthquake impacts: a large proportion of the building stock experienced no or only limited damage. In contrast, moderate and severe damage affected a smaller proportion of buildings. As a result, the classifier is encouraged to learn decision boundaries that are more sensitive to higher damage levels, thereby improving its ability to discriminate among damage classes in imbalanced seismic datasets.

3.4.2.2. Overlapping categories

In the dataset, the damage categories exhibited considerable overlap in the feature space, meaning that different damage classes (e.g., Moderate Damage and No Damage or Severe Damage) sometimes shared similar values of the predictor variables. This can be due to class aggregation in the EMS-98 scale, intra-class variability, and the limited ability of InSAR-derived features (e.g., LOS displacement and coherence) to fully capture subtle structural differences. For example, neighbouring buildings may exhibit similar values for some predictor features, such as ground displacement, coherence, or building height, while being assigned different observed damage states. As a result, cases labelled as Moderate Damage may overlap in feature space with either No Damage or Severe Damage buildings, making it challenging to clearly distinguish between categories in the multi-class damage classification. To address challenges associated with overlapping classes in multi-class damage classification, this study employed the OvO binary decomposition strategy. OvO splits a dataset with C classes into $C(C-1)/2$ binary classification problems. Each classifier is trained using only the training samples corresponding to the specific pair of classes (c_i, c_j) with $i < j$. New samples are classified by being submitted to all pairwise classifiers. This approach improves class separability and stability, particularly when class boundaries are not well-defined, as observed in the building damage data.

Inspired by the implementation described in [60], we applied the OvO strategy within the RF framework, using majority voting for final class assignment. In this scheme, each classifier outputs a confidence score r_{ij} indicating the preference for class c_i over c_j, and the final predicted class for each sample is determined by aggregating the votes across all pairwise classifiers as follows:

$$\text{Class} = \arg\max_{i=1,\ldots,C} \sum_{1 \le j \ne i \le C} s_{ij}, \tag{3.6}$$

where,

$$s_{ij} = \begin{cases} 1 & \text{if } r_{ij} > r_{ji} \\ 0 & \text{otherwise} \end{cases} \tag{3.7}$$

3.4.2.3. Performance evaluation

To evaluate model performance per region, the 20% unseen test data was used. Performance was assessed using Overall Accuracy (OA), precision, recall, F1-score, and Cohen's kappa, which are widely used metrics in classification tasks [61]:

- OA measures the proportion of correctly classified samples among all samples.

- Precision quantifies the proportion of true positive predictions among all positive predictions, indicating the model's exactness.
- Recall measures the proportion of true positive predictions among all actual positive cases, indicating the model's ability to capture positive instances.
- F1-score is the harmonic mean of precision and recall, providing a single measure that balances both metrics, especially useful under class imbalance.
- Cohen's kappa measures the classifier's performance in predicting target classes relative to the ground-truth labels.

Given the class imbalance typical of damage datasets, these metrics were either macro- or weighted-averaged to capture overall model performance while also reflecting class-specific predictive capabilities [61]. Confusion matrices were also generated to quantify misclassifications across damage categories, aiding in interpreting model performance for each damage grade.

In a separate experiment, conventional seismic indicators, such as PGV and PGA, were used to evaluate the predictive performance of InSAR-derived features. The objective was to examine whether InSAR-based inputs, ground displacement and coherence measures can yield comparable results within similar modelling frameworks. This evaluation was intended to determine whether ground displacements, as captured by satellite observations, can be considered equally effective representations of seismic effects as conventional intensity- and acceleration-based metrics.

To carry out this evaluation, we trained and tested classification models using InSAR-derived features alongside structural and site-related parameters, and compared their performance against models that used conventional seismic indicators with the same complementary inputs. Furthermore, we also trained models with all features combined and analysed their feature importances to assess the relative contribution of each type. This comparison helps determine whether InSAR-derived features are valid and reliable for use in building damage assessment tasks. If their predictive performance is comparable to that of conventional indicators, this would suggest that InSAR could serve as an alternative input, particularly in settings where conventional data are unavailable or difficult to obtain.

3.4.3. COMBINED LEARNING

To test the generalisability of the trained models across different seismic contexts, combined learning was designed by merging the datasets from Italy and Nepal into a single training workflow. This approach allows the model to learn generalised damage patterns across varying building typologies and seismic settings [8].

Only buildings with typologies common to all three regions were included, namely RC structures, good- and poor-quality masonry buildings, mixed-frame structures, and wood structures. For these shared typologies, all features, including building attributes, site-related variables, and InSAR-derived seismic indicators, were retained within each region and then combined; features from non-shared typologies were excluded. The combined dataset was split into 80% for training and 20% for testing, with multiple

iterations performed using different random splits to ensure the model was exposed to diverse building and ground-motion scenarios during training while retaining sufficient data for robust validation. The same training and evaluation procedure described in Section 3.4.2 was followed, including feature preprocessing, BRF model training based on OvO strategy, hyperparameter tuning using nested cross-validation, and performance evaluation using OA, precision, recall, and F1-score metrics.

This combined learning strategy aids in developing a generalised model capable of predicting building damage in different regional and seismic contexts, with potential for future application in other earthquake-prone regions where building-level damage datasets are limited.

3.5. Results

We assessed the performance of the proposed models across three urban areas affected by different earthquake events. A total of 10,253 buildings in Amatrice, 6,938 in Norcia, and 82,233 in Nepal were used in this study. Table 3.2 summarises the distribution of buildings across the No Damage, Moderate, and Severe Damage classes for each study area. Twenty models were trained and tested on randomly selected building subsets from each regional dataset, ensuring that hyperparameter tuning and evaluation were conducted independently for each case. To assess generalisation, an additional twenty models were trained and tested on randomly selected subsets from a combined dataset encompassing all three regions. The performance results of both analyses are presented below.

3.5.1. Performance evaluation of region-specific learning

Twenty OvO-based BRF models were trained using 80% of the data and evaluated on the remaining 20%. In each iteration, the dataset was randomly split into training and testing subsets. The models incorporated InSAR-derived features together with structural and site-specific attributes. The performance metrics for each region are presented in Figure 3.4. The bars in the figure display the precision, recall, and F1-score for each damage class obtained from the best-performing model, i.e., the model achieving the highest OA among the twenty tested. For comparison, the figure also reports the average values and standard deviations of these metrics over all twenty models. The standard deviations reflect the variability in model performance across different random train-test partitions, thereby indicating model stability with respect to data partitioning.

Table 3.2.: The distribution of buildings across damage levels for each study area.

	No Damage	Moderate	Severe
Amatrice	7051	2266	936
Norcia	4389	1587	962
Nepal	64395	9378	8460

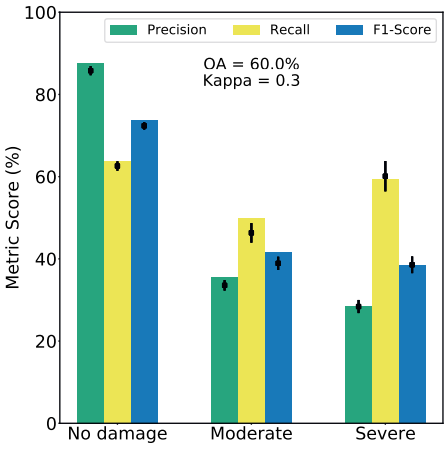

(a) Amatrice

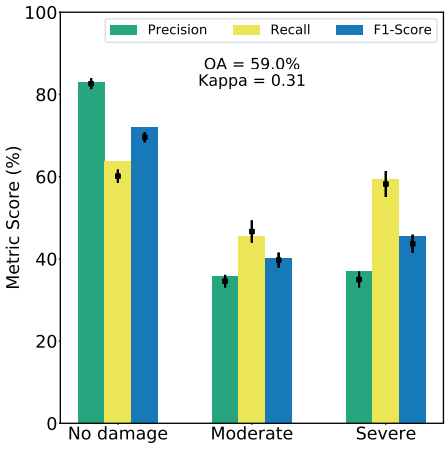

(b) Norcia

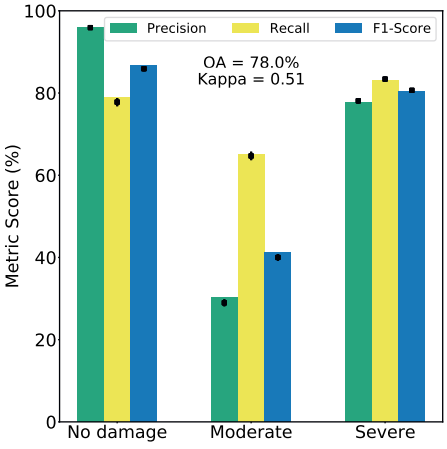

(c) Nepal

Figure 3.4.: Comparison of metric scores for each damage class across (a) Amatrice, (b) Norcia, and (c) Nepal, with a separate model trained for each region. The square within each bar indicates the average performance over twenty tests, and the vertical error bars represent the standard deviation for each metric. The models were trained using InSAR-derived, site-related, and building features, employing hyperparameter tuning through nested cross-validation, combined with an OvO strategy and a BRF classifier.

For the best-performing model, results confirmed strong performance in detecting the No Damage class across all regions. In Amatrice, the model achieved a precision of 88%, a recall of 64%, and an F1-score of 74%, while in Norcia, performance was slightly lower with values of 83%, 64%, and 72%, respectively. Nepal recorded the highest scores, with precision 96%, recall 79%, and F1-score 87%, reflecting an excellent ability to correctly identify intact structures.

For the Moderate Damage class, performance was lower. In Amatrice, precision, recall, and F1-score were 36%, 50%, and 42%, respectively; Norcia yielded similar values (36%, 46%, 40%), while Nepal showed a slightly better balance, with precision 30%, recall 65%, and F1-score 41%. These results indicated that the model could detect a considerable portion of moderately damaged buildings, even though misclassifications remain frequent.

The Severe Damage class showed clearer trends across sites. In Amatrice, precision, recall, and F1-score were 28%, 59%, and 38%, respectively; in Norcia, 37%, 59%, and 46%; and in Nepal, 78%, 83%, and 80%. These results indicate that the model was particularly effective in identifying heavily damaged buildings in Nepal. In terms of overall performance, the best model achieved 60% OA and 0.3 kappa in Amatrice, 59% OA and 0.31 kappa in Norcia, and substantially higher scores in Nepal (78% OA and 0.51 kappa).

These results suggest that the framework is capable of delivering robust performance in contexts where damage signals are more distinct and region-specific features are well represented in the data. Importantly, iterative model training on the Nepal dataset produced nearly negligible error bars, indicating high stability across training and testing splits. Conversely, the Italian regions exhibited larger error bars, reflecting relatively greater uncertainty. This reduced performance can be attributed to smaller sample sizes and stronger spatial intermixing of damage categories in the Italian datasets, which reduces class separability. Overall, these findings highlight the data-dependent nature of supervised classification and the importance of sufficiently large, representative, and reliable training datasets for achieving stable and reliable model performance.

When examining the overall performance of the trained models across regions, varying levels of classification performance were observed, as summarised in Figure 3.5. In this figure, precision, recall, and F1 scores are weighted by the number of samples in each class and averaged across all twenty tests, while OA and Cohen's Kappa are averaged over the iterations. Weighting by class size is adopted to account for the unequal distribution of damage classes and to provide an aggregate measure of model performance across the full dataset. These metrics are considered alongside OA and Cohen's Kappa to provide complementary measures of classification performance.

Based on these metrics, overall accuracy is similar for the Amatrice and Norcia case studies, at approximately 59% and 57%, respectively, while a substantially higher value of about 77% is achieved for Nepal. Cohen's Kappa shows the same trend, with relatively low agreement for Amatrice (~ 0.28) and Norcia (~ 0.29), and moderate agreement for Nepal (~ 0.50). Weighted precision reaches around 69% for Amatrice and 65% for Norcia, and is notably higher for Nepal at approximately 86%. A comparable pattern is observed for weighted recall, with values of roughly 57–59% for the Italian case studies and about 77% for Nepal. Consequently, the weighted F1-score remains close to 60–62%

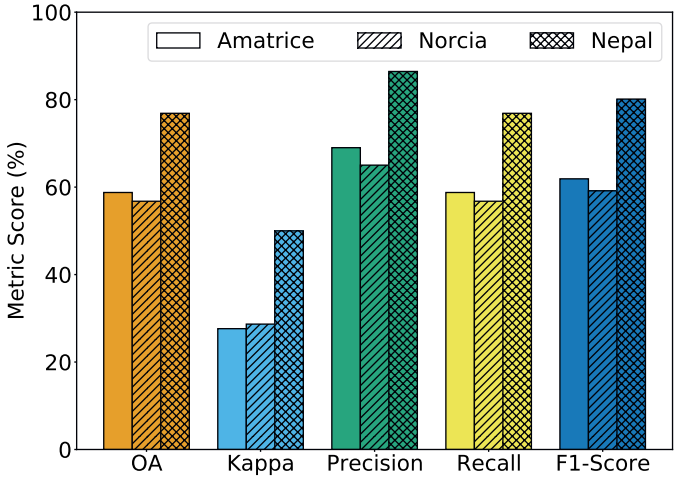

Figure 3.5.: Comparison of average model performance across the three regions. For each region, the bars show the mean weighted Precision, Recall, and F1-Score (weighted by class sample sizes across all test iterations), along with OA and Kappa, both averaged across iterations. All metrics were computed using building, site-related, and InSAR-derived features, employing an OvO strategy and a BRF classifier.

for Amatrice and Norcia, while rising to nearly 80% for Nepal. Overall, these results indicate consistently stronger classification performance for the Nepal dataset across all evaluation metrics. In contrast, the two Italian regions exhibit similar but comparatively lower levels of accuracy and agreement.

Cohen's Kappa values range from approximately 0.2 to 0.6 across the study areas, corresponding to fair to moderate agreement between predicted and observed damage classes. Unlike OA, the Kappa statistic accounts for the level of agreement that could occur by chance, based on the class distributions of the predictions and the ground truth data. This distinction is particularly relevant for imbalanced damage datasets, where relatively high OA may partly reflect correct predictions of a dominant class. The lower Kappa values for Amatrice and Norcia therefore indicate that agreement beyond chance is more limited in these datasets than OA alone would suggest, consistent with the greater classification difficulty observed in the Italian case studies.

The matrices illustrate the model's overall classification behaviour across all target classes, highlighting both correctly classified instances and systematic misclassifications. Figure 3.6 illustrates the confusion matrices of the best-performing models, each applied to its corresponding regional dataset. The diagonal elements represent the number of correctly predicted samples for each class, while the off-diagonal elements indicate misclassifications.

As illustrated in the matrices, a notable source of error arises when Severe Damage cases are misclassified as Moderate Damage, indicating that the model sometimes underestimates the extent of structural damage. At the same time, in other cases,

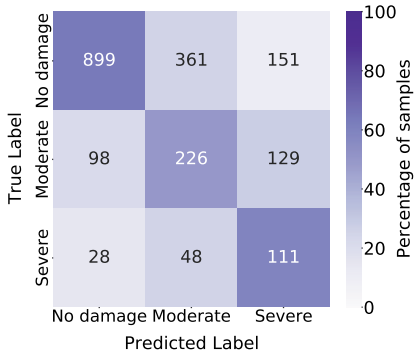

(a) Amatrice

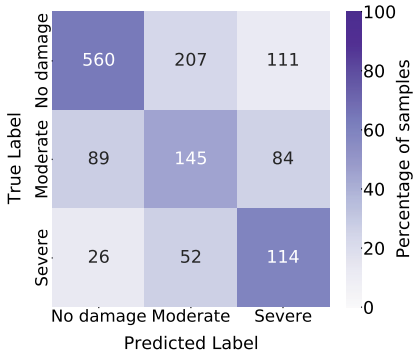

(b) Norcia

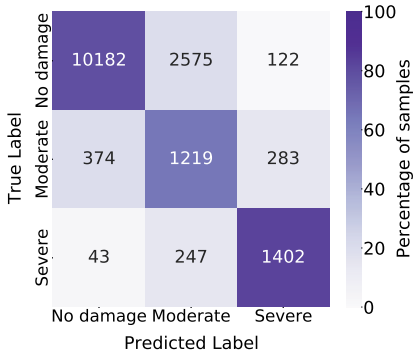

(c) Nepal

Figure 3.6.: Confusion matrices resulted from the best-performing model of region-specific learning for (a) Amatrice, (b) Norcia, and (c) Nepal. Rows represent the true damage classes, and columns represent the predicted damage classes. Diagonal cells indicate correctly classified samples, while off-diagonal cells indicate misclassifications between damage classes. Cell values show the number of samples assigned to each true–predicted class combination.

misclassifications from the No Damage class to the Moderate Damage class indicate that the model can also overestimate damage for otherwise undamaged structures.

Figure 3.7 presents the feature importance scores obtained from the best-performing model for each earthquake scenario.

The importance values reflect the relative contribution of each input variable to the model's predictive performance. In RF, this is estimated from the average reduction in impurity, a measure of how mixed or uncertain the class labels are within a tree node, across all trees in the ensemble. Features that consistently produce larger impurity reductions enable more effective separation of damage classes and therefore contribute

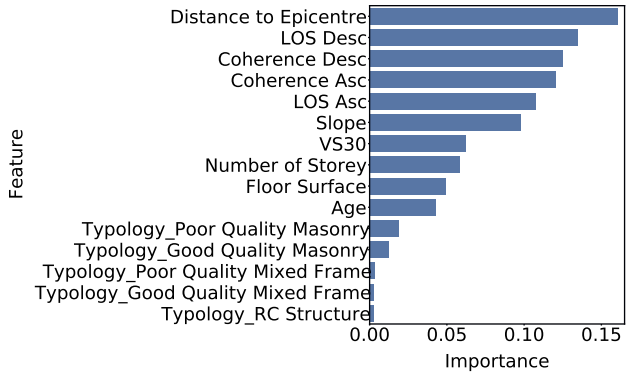

(a) Amatrice

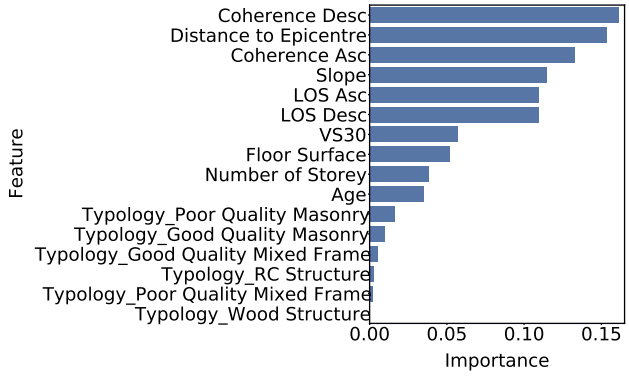

(b) Norcia

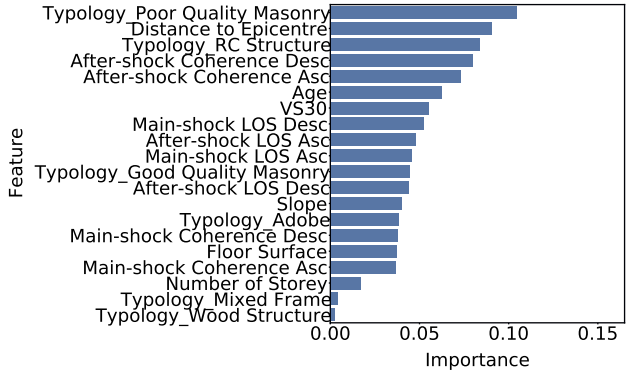

(c) Nepal

Figure 3.7.: Feature importance maps resulted from the best-performing model in the region-specific learning for (a) Amatrice, (b) Norcia, and (c) Nepal. Each bar shows the importance scores of features used in the training process.

more strongly to accurate classification. Higher scores thus indicate features that played a greater role in reducing classification error, whereas lower scores suggest a minimal influence. It is important to note, however, that feature importance reflects model-specific associations and does not imply direct causality. In other words, a feature may be important for prediction because it is correlated with damage patterns in the data, even if it is not a direct physical driver of damage.

For Amatrice (Figure 3.7a), the most influential feature was the distance to the epicentre, followed closely by LOS displacements and coherence measures. This highlights the significant role of proximity to the source and ground deformation patterns in explaining the observed building damage. Terrain slope and Vs30 also contributed meaningfully, whereas building-related attributes such as typology, number of storeys, and age showed relatively low importance.

In Norcia (Figure 3.7b), coherence maps, both ascending and descending, emerged as the most important features, slightly ahead of the distance to the epicentre. Slope and LOS displacements also ranked highly, reaffirming the importance of InSAR-derived features in capturing earthquake-induced impacts. Similar to Amatrice, building typology and other structural parameters contributed minimally. This suggests that in affected areas of Italy, ground displacement and site-related factors dominated the distribution of damage, while structural variability appeared less influential. However, this does not necessarily imply that structural features are inherently less important in controlling damage. Rather, within the building attributes available in the datasets, the building stock in Amatrice and Norcia (Figures A.2 and A.3) is relatively homogeneous compared to affected areas in Nepal (Figure A.4), exhibiting narrower ranges in typology, number of storeys, construction age, and floor surface. This lower variability may reduce the relative influence of these variables in the model. Other characteristics relevant to seismic performance, such as structural detailing and previous strengthening or retrofit interventions, are not explicitly represented in the available building attributes and may contribute to differences in observed damage.

For Nepal (Figure 3.7c), the ranking differed considerably. Here, structural features, particularly poor-quality masonry and RC structures, were among the top contributors, alongside distance to the epicentre and aftershock coherence features. Building age and Vs30 also ranked highly. Unlike in Italy, building-related variables played a much greater role in explaining damage patterns, likely reflecting the more heterogeneous building stock and the stronger influence of construction practices on the observed damage distribution in Nepal (Figure A.4). The presence of aftershock InSAR-derived coherence maps among the top features further highlights the cumulative effects of the earthquakes in this region.

Overall, the training strategy adopted in this study demonstrated a good capacity to learn the patterns associated with the three damage classes from the selected features. More specifically, InSAR-derived displacements and coherence showed promising results, indicating their potential to distinguish between damage levels. Building on these findings, an additional experiment was conducted to evaluate the performance of InSAR-derived features for multi-level damage assessment in direct comparison with conventional seismic intensity and acceleration-based indicators.

Conventional seismic indicators commonly used in post-earthquake building damage assessment include PGV, PGA, Pseudo-Spectral Accelerations (PSAs), and Modified Mercalli Intensity (MMI). PGV measures the maximum ground velocity during shaking and is more sensitive to longer-period motions, which tend to affect taller or more flexible buildings. PGA quantifies the maximum ground acceleration and is most relevant for short-period structures, which respond strongly to high-frequency shaking [62]. PSAs provide frequency-dependent measures of seismic demand at specified periods (0.3 s, 1.0 s, and 3.0 s), complementing PGV and PGA by characterising structural responses across different frequencies. MMI offers a qualitative assessment of earthquake impacts on people, structures, and the environment, ranging from 1 (not felt) to 10 (extreme) [63]. These indicators have been widely applied in post-earthquake damage classification studies [57, 64–66]. However, the applicability of PGV, PGA, and PSAs is often constrained by their reliance on dense ground-based seismic networks, which are unavailable or unevenly distributed in many regions, particularly in data-scarce environments. MMI, while not dependent on extensive instrumental coverage and therefore more broadly available, is inherently coarser and more subjective, with limited ability to capture frequency-dependent ground-motion characteristics or local site effects.

To evaluate InSAR's effectiveness as an alternative data source, classification models were trained using (i) InSAR-derived features with structural and site-related variables and (ii) conventional seismic indicators with the same structural and site-related variables. To ensure comparability, the same train–test splits and random seeds were applied across all analyses, using the region-specific learning strategy described in Section 3.4.2.

Model performance was assessed using macro-averaged precision, recall, and F1-scores across three damage classes. As illustrated in Figure 3.8, results show that InSAR-derived features provide predictive performance comparable to, and in some cases exceeding, that of conventional seismic indicators. For instance, in Norcia, InSAR features achieved macro-averaged precision, recall, and F1-scores of 50%, 55%, and 50%, respectively, with an overall accuracy of 55%. In Nepal, performance increased to 67%, 75%, and 68%, and an overall accuracy of 76%. Across all regions, the combination of LOS displacements and coherence effectively distinguished between damage classes, performing comparably to conventional seismic metrics. These results highlight the potential of InSAR as a scalable alternative for damage assessment, offering greater data availability and spatial coverage in areas where seismic intensity measures are unavailable or sparse. Given that InSAR products, such as those from Sentinel-1, are globally available, free of charge, and rapidly produced after an event, they provide a robust and physically meaningful basis for post-earthquake damage assessment, extending applicability beyond regions with dense ground-based seismic networks.

3.5.2. PERFORMANCE EVALUATION OF COMBINED LEARNING

To evaluate the generalisability of the proposed model across different earthquake scenarios, a combined learning strategy was adopted. All regional datasets were merged into a single pool and randomly split into 80% for training and 20% for testing. To avoid bias toward the larger Nepal dataset, a randomly selected subset of a similar size to the Italian datasets was used, ensuring balanced representation across regions. Before model

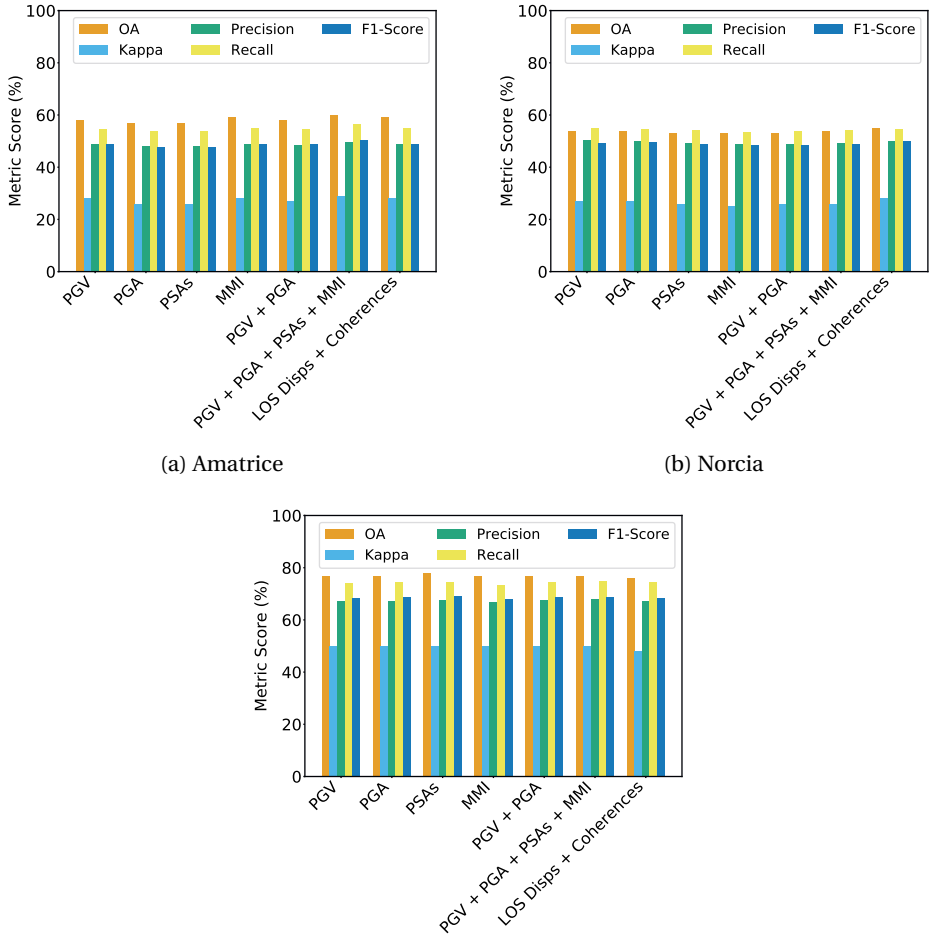

(a) Amatrice

(b) Norcia

(c) Nepal

Figure 3.8.: Comparison of overall metric scores for models trained using building and site features, combined either with conventional intensity/acceleration measures or with InSAR-derived features, for (a) Amatrice, (b) Norcia, and (c) Nepal. All models were developed using a BRF classifier, with hyperparameter optimisation performed through nested cross-validation and an OvO strategy. Recall, precision, and F1 scores are reported as macro-averaged across all classes. For Nepal, the InSAR-derived features include both mainshock and aftershock LOS displacements and coherence.

training, feature preprocessing and harmonisation were performed to ensure consistency across datasets. Only building typologies common to all datasets, i.e. RC structures, good- and poor-quality masonry, mixed-frame, and wood structures, were retained, establishing a standardised typology set applicable to all regions. These categories were harmonised based on the structural categories provided in the source datasets; however, buildings within the same broad typology may still exhibit region-specific differences in construction characteristics. In the Italian datasets, good- and poor-quality mixed frames classes were combined into a single unified category, as the Nepal dataset did not provide a corresponding quality-based distinction for mixed-frame buildings, thereby ensuring a consistent typology classification across the datasets. Regarding InSAR-derived features, only coherence and LOS displacement measurements from the main shock were included to maintain consistency with the Italian datasets. The same training procedure outlined in Section 3.4.2 was applied, and the resulting performance metrics are presented in Figure 3.9.

The best-performing model among the twenty test runs demonstrated excellent accuracy in identifying undamaged buildings, achieving a precision of 81%, a recall of 74%, and an F1-score of 77%. The Moderate Damage class, typically the most challenging to classify, achieved a recall of 53% and an F1-score of 50%, indicating a reasonable detection capability across sites. The Severe Damage class exhibited strong performance,

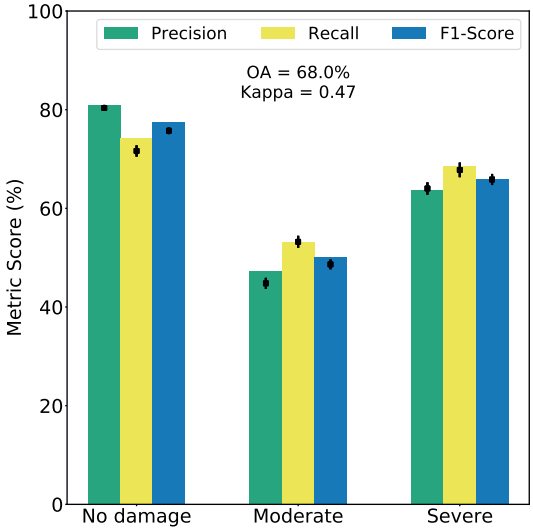

Figure 3.9.: Comparison of performance metrics for each damage class obtained from the combined dataset. The square within each bar indicates the average performance over twenty tests, and the vertical error bars represent the standard deviation for each metric. The models were trained using InSAR-derived, site, and building features, with hyperparameter tuning through nested cross-validation, employing an OvO strategy and a BRF classifier.

achieving 64% precision, 69% recall, and 66% F1-score. Weighted-average metrics confirmed the classifier's overall effectiveness, with 68% OA and a kappa of 0.47.

When examining the results over the twenty test runs, the model exhibited remarkable consistency across all classes. The No Damage class consistently achieved the highest precision, recall, and F1-scores, reflecting the model's ability to reliably identify intact structures. The Severe Damage class also showed stable performance, with slightly lower precision but high recall, indicating that the model successfully captured most buildings falling in this class, even if some false positives occurred. The Moderate Damage class exhibited greater variability across iterations, yet recall remained consistently above 50% and F1-scores clustered around 47%, highlighting that the model detected a substantial portion of moderately damaged buildings. The narrow spread of metrics across multiple test runs demonstrated that the combined training approach was robust, providing reliable performance regardless of random data splits, while effectively balancing sensitivity to each damage class.

Overall, these results demonstrate that the combined model generalises well across multiple datasets, reliably identifying undamaged buildings while achieving notable improvements in detecting moderate and severe damage compared to region-specific models. Unlike models trained separately on individual earthquake datasets, which may not generalise well beyond their original region, the combined model benefits from learning across diverse conditions, leading to more consistent distinctions between damage levels across different earthquake scenarios.

Figure 3.10 shows the distribution of predicted versus observed damage classes for the best-performing combined model for the events in Italy and Nepal. The comparison highlights how well the model captured the observed damage patterns across damage categories and regions.

These observations are further supported by Figure 3.11, which presents the confusion matrices of the same best-performing combined model for the complete test dataset and separately for the Central Italy and Nepal subsets.

Overall, across the combined test dataset, the model achieved higher classification performance for the extreme classes (No Damage and Severe). In contrast, the Moderate Damage class remained the most challenging, with a notable proportion of samples misclassified into adjacent categories. Out of all the true No Damage class samples, 2113 (74.2%) were correctly predicted, while 612 (21.5%) were misclassified as the Moderate Damage class and 123 (4.3%) as the Severe Damage class. The model correctly identified 713 (53.1%) samples as the Moderate Damage class, but misclassified 380 (28.3%) as the No Damage class and 249 (18.6%) as the Severe Damage class, suggesting some ambiguity in identifying the Moderate Damage class. For the Severe Damage class, 651 samples (68.5%) were correctly classified, with 184 (19.4%) misclassified as Moderate Damage and 115 (12.1%) as No Damage.

The regional evaluation of the same combined model (Figure 3.11) shows that performance remained higher for Nepal than for Central Italy. The model correctly classified 71.9% of the Nepal test samples compared with 65.5% of the Central Italy samples. This difference was particularly evident for the Moderate and Severe Damage classes: 67.4% and 88.1% of these samples, respectively, were correctly classified in Nepal, compared with 42.3% and 38.7% in Central Italy. In contrast, the No Damage class was

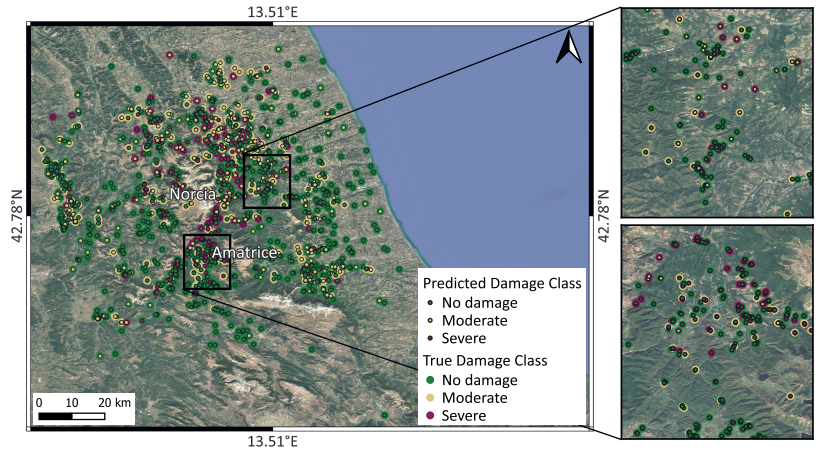

(a)

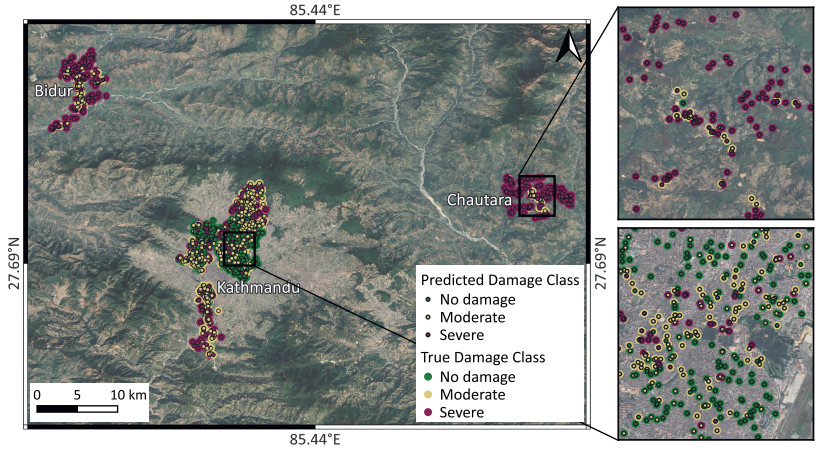

(b)

Figure 3.10.: Distribution of predicted and true damage classes obtained from the best-performing combined model for (a) the central Italy and (b) the Gorkha earthquake events

more accurately identified in Central Italy (77.7%) than in Nepal (60.0%). These results indicate that, although the combined model was applied across both regional contexts, its performance is not uniform across them.

Given the consistently greater classification difficulty associated with Moderate Damage, this class was examined further across the regional subsets. Confusion between Moderate and No Damage was considerably greater in Central Italy than in Nepal. The misclassified samples also showed systematic differences in building typologies. For example, Moderate cases classified as No Damage were more frequently associated

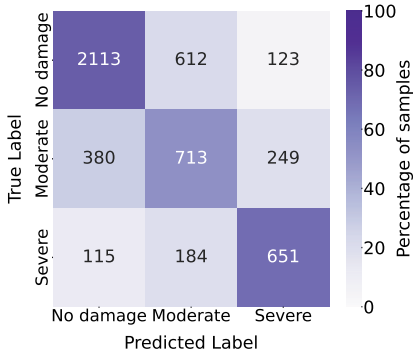

(a) Combined

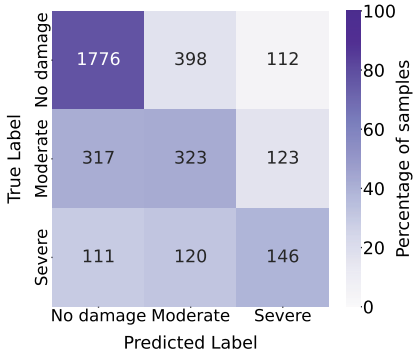

(b) Italy

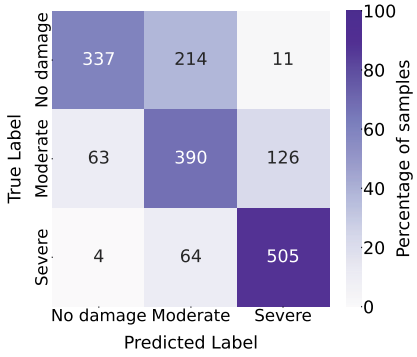

(c) Nepal

Figure 3.11.: Confusion matrices of the best-performing model using the combined-learning approach, evaluated on (a) the complete combined test dataset, (b) the Central Italy subset, comprising the Amatrice and Norcia test samples, and (c) the Nepal test subset. All panels correspond to predictions from the same best-performing combined model. Rows represent the true damage classes, and columns represent the predicted damage classes. Diagonal cells indicate correctly classified samples, while off-diagonal cells indicate misclassifications between damage classes. Cell values show the number of samples assigned to each true–predicted class combination.

with good-quality masonry in Italy and with RC structures in Nepal, whereas those classified as Severe Damage were predominantly associated with poor-quality masonry. Considerable overlap was also observed in the InSAR-derived and site-related feature values among the Moderate Damage groups, particularly between correctly classified samples and those classified as No Damage. These patterns suggest that the difficulty in classifying the Moderate Damage class is influenced by both the typology and damage-class composition of the regional datasets and the limited separability of the Moderate Damage class within the current feature space.

Given these differences in the typological composition of the misclassified samples, model classification performance was also examined separately for the main building typologies. In Central Italy, the model achieved the highest overall correct classification rates for RC buildings, followed by good-quality masonry buildings, whereas lower rates were observed for poor-quality masonry buildings. However, these differences in model performance cannot be attributed solely to building typology, because the damage-class distributions differ substantially among the typology subsets. RC buildings in Amatrice and Norcia were predominantly classified as No Damage in the reference data (96.2% and 90.9%, respectively). In contrast, the Nepal RC subset contained a substantially larger proportion of Moderate Damage cases. Conversely, poor-quality masonry in Nepal was predominantly associated with Severe Damage (78.9%), whereas this typology exhibited a more heterogeneous distribution of damage in the Italian datasets.

Figure 3.12 presents the feature importance scores obtained from the best-performing model trained on the combined dataset.

The figure shows a more balanced distribution of feature importance compared to the region-specific results. The distance to the epicentre, coherence, and LOS displacements remained the most influential factors, but building typology (e.g., poor-quality masonry, RC structures) and floor surface gained greater importance. This contrasts with the Italian regions (Figures 3.7a and 3.7b), where structural attributes played a relatively minor role. In the combined learning setting, their relative importance increased, probably

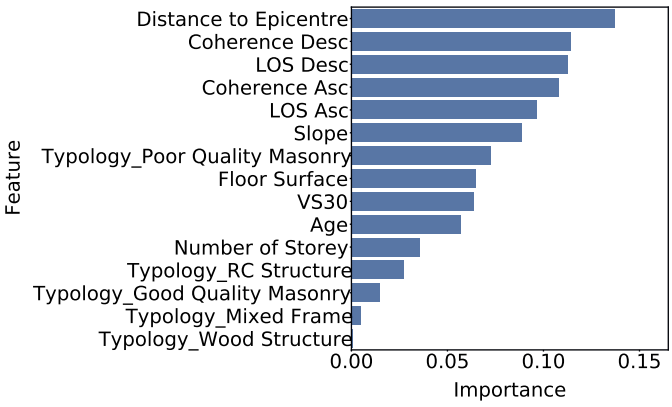

Figure 3.12.: Feature importance map resulted from the best-performing model trained on the combined dataset.

reflecting the influence of regions such as Nepal, where construction practices have a strong impact on damage outcomes.

3.6. Discussion

This study advances post-earthquake assessment of building damage by integrating InSAR-derived displacement and coherence with structural and site-related variables into an ML framework for multi-level damage classification. Unlike previous research, which primarily focused on binary classification, distinguishing only between collapsed and standing structure, this work enables classification into three classes of damage: No Damage, Moderate, and Severe. This represents a step forward toward developing operationally relevant tools for post-earthquake reconnaissance.

A key strength of the framework lies in the physical interpretability of the features. InSAR displacement provides a physically interpretable measure of earthquake-induced surface deformation, while coherence captures surface-level structural disruption. Together, these features provide a richer and more physically meaningful representation of earthquake impacts. The results further showed that InSAR-derived features achieved predictive performance comparable to conventional seismic indicators, such as PGV and PGA, highlighting their potential as an effective alternative in regions where seismic networks are sparse or unavailable.

This study also contributes methodologically by directly addressing class imbalance and overlap, two challenges that frequently undermine earthquake damage classification. We employed a BRF with undersampling strategies and combined this with an OvO decomposition strategy to better separate adjacent classes. This design improved the model's sensitivity to underrepresented and ambiguous categories, particularly in detecting the Moderate Damage class. Oversampling was intentionally avoided to prevent the generation of synthetic displacement or related features that could produce physically unrealistic data. Although the ML algorithms themselves are established methods, the novelty of this work lies in integrating physically grounded InSAR features, multi-source data, and a scalable learning design tailored specifically for operational post-earthquake multi-class damage assessment.

An additional methodological consideration concerns the spatial integration of field observations with remotely sensed features. Features were extracted at field observation points rather than building footprints to ensure direct spatial correspondence with the documented field conditions. This choice also reduced potential mismatches arising from positional and temporal inaccuracies in the available building-footprint data, which could otherwise lead to incorrect associations between input feature pixels and damage labels. Working at the point level also retained fine-scale variability in displacement and other features, which might otherwise be diluted when aggregating to building footprints. Overall, the point-based approach reduced uncertainties in building assignment and enabled the consistent integration of pixel-based RS products.

The proposed approach was tested on datasets from three earthquake events with distinct seismic characteristics and building conditions in Amatrice, Norcia, and Nepal. The results demonstrate the potential of the proposed framework for scalable application and generalisation across the seismic and structural contexts represented in this study.

Both region-specific and combined learning schemes were evaluated, showing that the model can adapt to different seismic and structural contexts. Region-specific learning revealed consistent performance across the Italian datasets, reflecting their similar building stocks and damage patterns, while the Nepal case achieved substantially higher scores. A key contribution of this study is also the systematic validation of physically informed InSAR features across multiple earthquake events rather than within a single regional case study. By comparing separate regional models with a combined multi-event framework, the analysis further shows how the predictive value of displacement and coherence varies with regional data characteristics and class separability. This strengthens the case for using InSAR-derived features as reliable inputs for scalable multi-class post-earthquake damage assessment.

The performance results collectively highlighted the model's varying capability across damage categories. The consistently high precision and recall for the No Damage class indicated that the model reliably identified intact buildings while keeping false alarms low, which is crucial for avoiding unnecessary allocation of inspection resources. In contrast, the Moderate Damage class showed weaker and less balanced performance. Although recall values suggested that a fair proportion of moderately damaged buildings were detected, the low precision revealed that many predictions were misclassified, reducing confidence in this category. Importantly, the implications of these errors were not symmetric. When the Moderate Damage class is misclassified as the Severe Damage class, the consequence is generally conservative, since such buildings would still be flagged for attention. However, when Moderate Damage cases are incorrectly classified as No Damage class, the risk increases because potentially unsafe structures might be overlooked. For the Severe Damage class, the model demonstrated strong recall across all sites, especially in Nepal, indicating that most heavily damaged buildings were successfully identified, although lower precision in Italy suggests some false positives.

Performance differences between Nepal and the Italian regions highlighted the model's sensitivity to data quality and regional characteristics. The notably higher accuracy and stability observed for Nepal under region-specific learning reflected the substantially larger sample size, more distinct spatial damage patterns, and greater heterogeneity in structural typologies. In contrast, the relatively homogeneous building stock in Amatrice and Norcia, together with smaller sample sizes and stronger spatial intermixing of damage categories, limited class separability and increased uncertainty. These findings emphasise that data richness and local building characteristics are key determinants of classification performance. However, building-level structural and exposure data are not consistently available, which can limit the model's operational deployment in emergency contexts. The regional evaluation of the combined-learning framework further supported its generalisability across the seismic and structural contexts represented in this study, as the same model maintained predictive capability in both Central Italy and Nepal. Nevertheless, the higher performance retained for Nepal indicates that generalisation is not uniform and remains influenced by regional data characteristics and class separability.

Feature importance analysis provided further insight into the drivers of model predictions. In all regions, InSAR-derived and site-related variables, such as the distance to the epicentre, LOS displacement, and coherence, consistently ranked among the most

influential. The role of structural attributes, however, varied. In Nepal, heterogeneous construction quality and seismic design practices made structural variables highly predictive, while in Italy, their contribution was more limited due to the relative uniformity of the building stock. The structural features do not capture all characteristics relevant to seismic performance; factors such as structural detailing and previous strengthening or retrofit interventions were not explicitly represented in the datasets and may also influence observed damage. The combined learning reinforced these observations, showing that when data from multiple regions are pooled, both structural and seismic/site-related features contribute meaningfully to generalisation across diverse contexts. These variations indicate that the relative importance of predictor variables is context-dependent and can vary with building stock, construction practices, site conditions, and earthquake characteristics. Therefore, no single set of features can be assumed to be universally dominant, highlighting the importance of local model calibration or training on sufficiently diverse datasets to support generalisation across different seismic contexts. The present feature-importance analysis is evaluated at the regional scale and does not resolve variations among individual building typologies. Different structural typologies may therefore be associated with different combinations of influential seismic, site-related, and structural predictors, potentially contributing to variations in predictive performance. Further typology-specific model interpretation would be required to investigate these relationships. The combined learning results nevertheless demonstrated that the proposed approach can balance these contributions across the investigated datasets, supporting its potential for scalable application across diverse earthquake contexts.

The results also highlight several limitations of the proposed framework. The Moderate Damage class was consistently the most difficult to classify, with frequent confusion with both the No Damage and Severe Damage classes. Several factors may contribute to this difficulty. First, the intermediate nature of Moderate Damage can result in overlapping characteristics with neighbouring damage states, reducing class separability. Uncertainty in field-assigned damage labels may further increase ambiguity near the boundaries between damage states. Further examination of the misclassified Moderate Damage samples supported this interpretation, revealing differences in building typologies and overlapping ranges across several continuous features. Second, the available feature set may not fully capture the characteristics associated with moderate damage. InSAR measures permanent surface deformation between acquisitions and may therefore have limited sensitivity to transient or internal processes, such as cumulative cyclic effects or partial structural degradation, that do not manifest as clear, persistent deformation. Consequently, some manifestations of moderate damage may not be sufficiently represented by the available InSAR-derived features, further reducing their separability from neighbouring damage classes.

Future work should therefore prioritise features and modelling strategies that capture subtler deformation behaviour, including higher-resolution InSAR products and three-dimensional displacement decomposition to better resolve localised deformation patterns and both vertical and horizontal motion components. For regional-scale emergency response, the current framework remains advantageous because it relies on consistently available InSAR-derived features and enables efficient mapping over large

areas. Higher-resolution InSAR products may be more suitable for targeted urban-scale assessments that require detailed spatial information, as they can improve detection of localised deformation associated with individual structures; however, their availability, acquisition timing, and spatial coverage may limit their operational use immediately after an earthquake. Similarly, three-dimensional displacement decomposition could improve the interpretation of complex ground motion by resolving horizontal and vertical components, but it requires additional SAR observations with suitable acquisition geometries. For detailed building-level damage assessment, the fusion of complementary data sources, such as cloud-free optical imagery, LiDAR, and detailed building inventory information, could provide damage indicators beyond what is directly observable from SAR measurements alone. However, these data sources are dependent on factors such as cloud conditions, acquisition availability, and processing requirements. Therefore, while these approaches may improve moderate-damage detection, their application involves trade-offs among accuracy, spatial scale, data availability, and response time, and they are most suitable as complementary approaches when operational conditions permit.

A further limitation concerns the supervised learning framework's dependence on labelled damage data. In the present analysis, field-assessed damage labels were required to train the models for each earthquake context. If a model were to be trained entirely from scratch following every new earthquake, obtaining sufficient field-assessed damage data could reduce the time advantage of remote-sensing-based assessment. The longer-term objective is therefore to reduce this dependence by developing models from existing earthquake datasets that can subsequently be transferred or adapted to new events using a smaller amount of representative event-specific damage information. The present work provides an initial basis for this direction by developing and evaluating region-specific and combined-learning models across multiple earthquake contexts. However, transfer to a new earthquake not represented in the training data was not evaluated and remains an important direction for future research.

A related challenge concerns the availability, consistency, and transferability of structural building information across geographical regions. Building inventories may differ in the attributes they contain, their level of detail, classification schemes, and data quality. Consequently, structural variables available in one region may be unavailable, defined differently, or not directly comparable in another. Harmonisation of structural building information across regional datasets is therefore needed to assess how differences in the availability and definition of these attributes affect model performance and transferability.

To address these regional dependencies and reduce reliance on extensive event-specific damage data, future research should investigate the transferability of models to new earthquake events. Transfer learning could leverage models trained across previous earthquake events and adapt them to a new event using a limited amount of representative event-specific damage data, reducing the need to train a model entirely from scratch. For example, models trained on data-rich regions, such as Nepal, could be adapted to improve performance in data-scarce settings, such as Central Italy. Domain adaptation techniques, including adversarial domain discriminators, could further address distributional shifts associated with differences in construction practices, seismic conditions, displacement patterns, and damage distributions.

Incorporating physics-informed features, such as proxies for structural fragility or strain, could also improve model interpretability and reduce reliance on purely empirical correlations identified during training. Finally, extending the analysis to a larger set of earthquake events across diverse seismic environments, building typologies, and damage distributions would enable a more comprehensive evaluation of model robustness and transferability beyond the earthquake contexts considered in this study.

A further limitation relates to the spatial resolution of the InSAR data used in this study. Sentinel-1 imagery has an approximate ground resolution of $\sim 5 \times 20$ m, which, after multilooking, corresponds to an effective resolution of ~ 40 m. At this scale, individual pixels may include multiple buildings or land-cover types, leading to mixed-pixel effects. This spatial averaging reduces sensitivity to localised and small-scale structural changes, which are particularly important for distinguishing Moderate Damage, and contributes to reduced separability between Moderate and Severe classes. Sentinel-1 was intentionally selected for this study because it provides globally consistent, freely available, and high-revisit SAR observations, making it particularly suitable for scalable post-earthquake damage assessment across different regions. However, higher-resolution SAR satellites such as TerraSAR-X or COSMO-SkyMed could improve the detection of fine-scale deformation and potentially enhance class separability, although their limited spatial coverage and reduced operational availability constrain their use in large-scale applications.

To preserve the total displacement vector and capture the combined influence of all directions, we therefore retained LOS in our analysis. Future work could refine the displacement representation by combining multiple SAR acquisitions with different orbits or satellites, or by integrating complementary geodetic data such as GPS, to enable a more precise decomposition of three-dimensional motions. Offset tracking, although less accurate than interferometry, could also serve as a useful alternative when very large displacements occur or when accuracy demands are lower. Additionally, displacement estimates remain sensitive to atmospheric noise, phase unwrapping errors, and decorrelation, particularly in areas with steep topography, severe damage, or dense vegetation cover. Although atmospheric correction was applied, residual artefacts cannot be fully excluded.

These methodological and data-related constraints do not operate uniformly across space, and their influence can vary substantially with regional characteristics, building practices, and the distribution of damage. This interplay between local conditions and sensor limitations contributes to the class-dependent uncertainties observed in the results. With this in mind, extending the analysis to additional earthquake events in different geographical regions becomes necessary to assess whether the relationships identified in this research hold across different tectonic settings and structural contexts. Such testing will help clarify whether the observed patterns reflect general physical mechanisms or are shaped by region-specific factors.

3.7. Conclusion

In this chapter, we developed a novel Machine Learning (ML) framework for classifying multi-level building damage after earthquakes using Synthetic Aperture

Radar Interferometry (InSAR) data. The proposed approach integrates co-seismic InSAR displacement and coherence with site-related and building parameters, employing a One-vs-One (OvO) strategy and a Balanced Random Forest (BRF) classifier to enable multi-level damage prediction. The framework was designed in two progressive components. First, we developed region-specific learning models, training them on datasets from each region separately, and we investigated the effectiveness of co-seismic InSAR displacement and coherence as indicators of seismic ground motion and impact in predicting multi-level building damage. Second, we developed a combined-learning model by integrating datasets from multiple earthquake events to assess the generalisability of the proposed training approach across different regions. This framework aims to support stakeholders and decision-makers in conducting more efficient post-earthquake building assessment, particularly in scenarios where conventional seismic indicators such as Peak Ground Velocity (PGV) and Peak Ground Acceleration (PGA) are unavailable.

The framework was evaluated on three earthquake events in Amatrice and Norcia, Italy, and Gorkha in Nepal, which were characterised by distinct seismic and structural conditions. The results showed that InSAR-derived displacement and coherence, when combined with building and site-related features, provide strong predictive capability for multi-level building damage assessment. The region-specific learning approach, implemented with the BRF and OvO strategy, achieved satisfactory overall accuracies, with performance varying across events. The most robust results were obtained for the Nepal case study, where the larger dataset and clearer spatial damage patterns contributed to improved prediction performance.

The best-performing models in the region-specific learning consistently achieved high accuracy in detecting undamaged buildings, with precision between 83–96%, recall between 64–79%, and F1-score between 72–87%. They also showed strong ability to detect the Severe Damage class, particularly in Nepal, where F1-scores reached up to 80%. The Moderate Damage class remained more challenging to classify, with F1-scores typically between 40–42%, although the models still captured a substantial proportion of affected structures. Overall accuracies ranged from 59–60% for the Amatrice and Norcia events to 78% for Nepal, with corresponding Cohen's kappa values between 0.3 and 0.51, confirming moderate agreement and highlighting the benefit of richer datasets and clearer spatial damage patterns.

The combined-learning model further demonstrated the framework's ability to integrate information from earthquakes characterised by different building typologies and seismic conditions. The best-performing combined model showed excellent predictive ability for intact buildings (F1-score 77%) and robust detection of the Severe Damage class (F1-score 66%), while the Moderate Damage class remained the most challenging category (F1-score 50%). These results demonstrate that the proposed approach can learn across the different seismic and structural contexts represented in the combined dataset, although its performance varies across regions and damage classes.

Feature importance analysis revealed that InSAR-derived displacement and coherence, along with the distance to the epicentre, were the most influential variables in the region-specific models. In contrast, building typologies and structural attributes gained greater prominence in the combined-learning configuration. These findings emphasise

the value of InSAR displacement and coherence as reliable indicators of seismic impact and building damage, particularly when conventional ground-motion parameters such as intensity or acceleration are unavailable.

Overall, this study contributes a novel, interpretable, and scalable framework for multi-level earthquake damage classification using InSAR and ML. The proposed framework offers a promising solution for regional-scale assessment of building damage in the immediate aftermath of earthquakes. By leveraging InSAR data, influential site-related and structural features, and robust ML techniques, the approach effectively complements traditional seismic measures and field-based assessments. Importantly, it demonstrates the potential to capture moderate damage levels, address overlapping damage categories, and support data-driven decision-making for emergency response and recovery planning.

Data Availability

The datasets supporting the findings of this study are available through public, third-party, and licensed repositories. The earthquake-related features, including PGV, PGA, PSAs, and MMI, were retrieved from the USGS event pages for the Gorkha (https://earthquake.usgs.gov/earthquakes/eventpage/us20002926/), Amatrice (https://earthquake.usgs.gov/earthquakes/eventpage/us10006g7d/), and Norcia (https://earthquake.usgs.gov/earthquakes/eventpage/us1000731j/) earthquakes, with global Vs30 data sourced from the USGS Vs30 archive (https://earthquake.usgs.gov/data/vs30/). Regarding building damage data, the Central Italy datasets are available upon request through the Database of Observed Damage (DaDO) platform (https://egeos.eucentre.it/danno_osservato/web/danno_osservato?lang=EN). The National Society for Earthquake Technology-Nepal (NSET) provided building damage data for the Gorkha, Nepal earthquake, which is not publicly available due to third-party confidentiality restrictions. The pre-trained ML models, InSAR-derived products (displacement and coherence maps), and other feature datasets generated during this study are archived in the 4TU.ResearchData repository (https://doi.org/10.4121/12ea8c26-9dcc-423d-a4e9-72ffde2ad8af.v1).

REFERENCES

[1] A. Moreira, P. Prats-Iraola, M. Younis, G. Krieger, I. Hajnsek and K. P. Papathanassiou. 'A tutorial on synthetic aperture radar'. In: *IEEE Geoscience and Remote Sensing Magazine* 1.1 (2013), pp. 6–43. DOI: 10.1109/MGRS.2013.2248301.

[2] H. Cruz, M. Véstias, J. Monteiro, H. Neto and R. P. Duarte. 'A review of synthetic-aperture radar image formation algorithms and implementations: A computational perspective'. In: *Remote Sensing* 14.5 (2022), p. 1258. DOI: 10.3390/rs14051258.

[3] L. Meng, C. Yan, S. Lv, H. Sun, S. Xue, Q. Li, L. Zhou, D. Edwing, K. Edwing, X. Geng *et al.* 'Synthetic aperture radar for geosciences'. In: *Reviews of Geophysics* 62.3 (2024). DOI: 10.1029/2023RG000821.

[4] C.-H. Lu, C.-F. Ni, C.-P. Chang, J.-Y. Yen and R. Y. Chuang. 'Coherence difference analysis of Sentinel-1 SAR interferogram to identify earthquake-induced disasters in urban areas'. In: *Remote Sensing* 10.8 (2018), p. 1318. DOI: 10.3390/rs10081318.

[5] M. Matsuoka and F. Yamazaki. 'Use of satellite SAR intensity imagery for detecting building areas damaged due to earthquakes'. In: *Earthquake Spectra* 20.3 (2004), pp. 975–994. DOI: 10.1193/1.1774182.

[6] H. Miura, S. Midorikawa and M. Matsuoka. 'Building damage assessment using high-resolution satellite SAR images of the 2010 Haiti earthquake'. In: *Earthquake Spectra* 32.1 (2016), pp. 591–610. DOI: 10.1193/033014eqs042m.

[7] S. Karimzadeh, M. Matsuoka, M. Miyajima, B. Adriano, A. Fallahi and J. Karashi. 'Sequential SAR coherence method for the monitoring of buildings in Sarpole-Zahab, Iran'. In: *Remote Sensing* 10.8 (2018), p. 1255. DOI: 10.3390/rs10081255.

[8] V. Macchiarulo, G. Giardina, P. Milillo, Y. D. Aktas and M. R. Whitworth. 'Integrating post-event very high resolution SAR imagery and machine learning for building-level earthquake damage assessment'. In: *Bulletin of Earthquake Engineering* (2024), pp. 1–27. DOI: 10.1007/s10518-024-01877-1.

[9] L. Ge, A. H.-M. Ng, X. Li, Y. Liu, Z. Du and Q. Liu. 'Near real-time satellite mapping of the 2015 Gorkha earthquake, Nepal'. In: *Annals of GIS* 21.3 (2015), pp. 175–190. DOI: 10.1080/19475683.2015.1068221.

[10] M. Watanabe, R. B. Thapa, T. Ohsumi, H. Fujiwara, C. Yonezawa, N. Tomii and S. Suzuki. 'Detection of damaged urban areas using interferometric SAR coherence change with PALSAR-2'. In: *Earth, Planets and Space* 68.1 (2016), p. 131. DOI: 10.1186/s40623-016-0513-2.

[11] S. Karimzadeh and M. Mastuoka. 'Building damage assessment using multisensor dual-polarized synthetic aperture radar data for the 2016 M 6.2 Amatrice earthquake, Italy'. In: *Remote Sensing* 9.4 (2017), p. 330. DOI: 10.3390/rs9040330.

[12] P. Mazzanti, S. Scancella, M. Virelli, S. Frittelli, V. Nocente and F. Lombardo. 'Assessing the performance of multi-resolution satellite SAR images for post-earthquake damage detection and mapping aimed at emergency response management'. In: *Remote Sensing* 14.9 (2022), p. 2210. DOI: 10.3390/rs14092210.

[13] X. Wang, G. Feng, L. He, Q. An, Z. Xiong, H. Lu, W. Wang, N. Li, Y. Zhao, Y. Wang *et al.* 'Evaluating urban building damage of 2023 Kahramanmaras, Turkey earthquake sequence using SAR change detection'. In: *Sensors* 23.14 (2023), p. 6342. DOI: 10.3390/s23146342.

[14] A. Rao, J. Jung, V. Silva, G. Molinario and S.-H. Yun. 'Earthquake building damage detection based on synthetic aperture radar imagery and machine learning'. In: *Natural Hazards and Earth System Sciences Discussions* 23 (2023), pp. 1–32. DOI: 10.5194/nhess-23-789-2023.

[15] L. Gong, C. Wang, F. Wu, J. Zhang, H. Zhang and Q. Li. 'Earthquake-induced building damage detection with post-event sub-meter VHR TerraSAR-X staring spotlight imagery'. In: *Remote Sensing* 8.11 (2016), p. 887. DOI: 10.3390/rs8110887.

[16] D. Brunner, G. Lemoine and L. Bruzzone. 'Earthquake damage assessment of buildings using VHR optical and SAR imagery'. In: *IEEE Transactions on Geoscience & Remote Sensing* 48.5 (2010), pp. 2403–2420. DOI: 10.1109/TGRS.2009.2038274.

[17] L. Dong and J. Shan. 'A comprehensive review of earthquake-induced building damage detection with remote sensing techniques'. In: *ISPRS Journal of Photogrammetry and Remote Sensing* 84 (2013), pp. 85–99. DOI: 10.1016/j.isprsjprs.2013.06.011.

[18] F. Foroughnia, V. Macchiarulo, L. Berg, M. DeJong, P. Milillo, K. W. Hudnut, K. Gavin and G. Giardina. 'Quantitative assessment of earthquake-induced building damage at regional scale using LiDAR data'. In: *International Journal of Disaster Risk Reduction* 106 (2024), p. 104403. DOI: 10.1016/j.ijdrr.2024.104403.

[19] D. K. Singh, V. Hoskere and P. Milillo. 'Multiclass post-earthquake building assessment integrating high-resolution optical and SAR satellite imagery, ground motion, and soil data with transformers'. In: *Earthquake Spectra* 41.5 (2025), pp. 3365–3392. DOI: https://doi.org/10.1177/87552930251377778.

[20] A. K. Gabriel, R. M. Goldstein and H. A. Zebker. 'Mapping small elevation changes over large areas: Differential radar interferometry'. In: *Journal of Geophysical Research: Solid Earth* 94.B7 (1989), pp. 9183–9191. DOI: 10.1029/JB094iB07p09183.

[21] D. Massonnet, M. Rossi, C. Carmona, F. Adragna, G. Peltzer, K. Feigl and T. Rabaute. 'The displacement field of the Landers earthquake mapped by radar interferometry'. In: *Nature* 364.6433 (1993), pp. 138–142. DOI: 10.1038/364138a0.

[22] Q. Li, W. Wang, J. Wang, J. Zhang and D. Geng. 'Exploring the relationship between InSAR coseismic deformation and earthquake-damaged buildings'. In: *Remote Sensing of Environment* 262 (2021), p. 112508. DOI: 10.1016/j.rse.2021.112508.

[23] A. Kumar, P. Lal, A. Prasad, P. Tripathy, P. Saikia *et al.* 'Analyzing urban damage and surface deformation based hazard-risk in Kathmandu city occurred during Nepal earthquake (2015) using SAR interferometry'. In: *Advances in Space Research* 70.12 (2022), pp. 3892–3904. DOI: 10.1016/j.asr.2022.02.003.

[24] X. Sun, X. Chen, L. Yang, W. Wang, X. Zhou, L. Wang and Y. Yao. 'Using InSAR and POLSAR to assess ground displacement and building damage after a seismic event: Case study of the 2021 Baicheng earthquake'. In: *Remote Sensing* 14.13 (2022), p. 3009. DOI: 10.3390/rs14133009.

[25] Y.-N. Du, D.-C. Feng and G. Wu. 'InSAR-based rapid damage assessment of urban building portfolios following the 2023 Turkey earthquake'. In: *International Journal of Disaster Risk Reduction* 103 (2024), p. 104317. DOI: https://doi.org/10.1016/j.ijdrr.2024.104317.

[26] F. Villani, R. Civico, S. Pucci, L. Pizzimenti, R. Nappi and P. M. De Martini. 'A database of the coseismic effects following the 30 October 2016 Norcia earthquake in Central Italy'. In: *Scientific Data* 5.1 (2018), pp. 1–11. DOI: 10.1038/sdata.2018.49.

[27] D. Cheloni, V. De Novellis, M. Albano, A. Antonioli, M. Anzidei, S. Atzori, A. Avallone, C. Bignami, M. Bonano, S. Calcaterra *et al.* 'Geodetic model of the 2016 Central Italy earthquake sequence inferred from InSAR and GPS data'. In: *Geophysical Research Letters* 44.13 (2017), pp. 6778–6787. DOI: 10.1002/2017GL073580.

[28] K. Goda, T. Kiyota, R. M. Pokhrel, G. Chiaro, T. Katagiri, K. Sharma and S. Wilkinson. 'The 2015 Gorkha Nepal earthquake: insights from earthquake damage survey'. In: *Frontiers in Built Environment* 1 (2015), p. 153814. DOI: 10.3389/fbuil.2015.00008.

[29] USGS, Earthquake Hazards Program. *M 7.8 - 67 km NNE of Bharatpur, Nepal*. 2025. URL: https://earthquake.usgs.gov/earthquakes/eventpage/us20002926/executive#scientific_finitefault/ (visited on 21/07/2025).

[30] ESA. *S1 Mission*. 2025. URL: https://sentiwiki.copernicus.eu/web/s1-mission (visited on 24/07/2025).

[31] Civil Protection Department website - Presidency of the Council of Ministers. *Da.D.O. (Database of Observed Damage)*. 2025. URL: https://egeos.eucentre.it/danno_osservato/web/danno_osservato?lang=EN (visited on 24/07/2025).

[32] G. Grünthal. *European Macroseismic Scale 1998 (EMS-98)*. Tech. rep. European Seismological Commission (ESC), 1998. DOI: 10.2312/EMS-98.full.en.

[33] M. Dolce, E. Speranza, F. Giordano, B. Borzi, F. Bocchi, C. Conte, A. Di Meo, M. Faravelli and V. Pascale. 'Observed damage database of past Italian earthquakes: the Da. DO WebGIS'. In: *Bollettino di Geofisica Teorica ed Applicata* 60.2 (2019). DOI: 10.4430/bgta0254.

[34] D. C. Heath, D. J. Wald, C. B. Worden, E. M. Thompson and G. M. Smoczyk. 'A global hybrid VS 30 map with a topographic slope-based default and regional map insets'. In: *Earthquake Spectra* 36.3 (2020), pp. 1570–1584. DOI: 10.1177/8755293020911137.

[35] E. H. P. USGS. *Vs30 Models and Data*. 2025. URL: https://earthquake.usgs.gov/data/vs30/ (visited on 22/07/2025).

[36] OpenTopography. *Global & Regional DEM*. 2025. URL: https://portal.opentopography.org/datasets (visited on 22/07/2025).

[37] H. A. Zebker and R. M. Goldstein. 'Topographic mapping from interferometric synthetic aperture radar observations'. In: *Journal of Geophysical Research: Solid Earth* 91.B5 (1986), pp. 4993–4999. DOI: 10.1029/JB091iB05p04993.

[38] D. Massonnet and K. L. Feigl. 'Radar interferometry and its application to changes in the Earth's surface'. In: *Reviews of Geophysics* 36.4 (1998), pp. 441–500. DOI: 10.1029/97RG03139.

[39] R. F. Hanssen. *Radar interferometry: data interpretation and error analysis*. Springer, 2001. DOI: 10.1007/0-306-47633-9.

[40] R. M. Goldstein and C. L. Werner. 'Radar interferogram filtering for geophysical applications'. In: *Geophysical Research Letters* 25.21 (1998), pp. 4035–4038. DOI: 10.1029/1998GL900033.

[41] R. M. Goldstein, H. A. Zebker and C. L. Werner. 'Satellite radar interferometry: Two-dimensional phase unwrapping'. In: *Radio Science* 23.4 (1988), pp. 713–720. DOI: 10.1029/RS023i004p00713.

[42] D. Guiglia and M. Pritt. *Two-dimensional phase unwrapping: Theory, algorithm, and software*. 1998.

[43] C. Werner, U. Wegmüller, T. Strozzi and A. Wiesmann. 'GAMMA SAR and interferometric processing software'. In: *Proceedings of the ERS-ENVISAT symposium, Gothenburg, Sweden*. Vol. 1620. 2000, p. 1620.

[44] A. Ferretti, C. Prati and F. Rocca. 'Permanent scatterers in SAR interferometry'. In: *IEEE Transactions on Geoscience & Remote Sensing* 39.1 (2002), pp. 8–20. DOI: 10.1109/IGARSS.1999.772008.

[45] C. Yu, N. T. Penna and Z. Li. 'Generation of real-time mode high-resolution water vapor fields from GPS observations'. In: *Journal of Geophysical Research: Atmospheres* 122.3 (2017), pp. 2008–2025. DOI: 10.1002/2016JD025753.

[46] C. Yu, Z. Li and N. T. Penna. 'Interferometric synthetic aperture radar atmospheric correction using a GPS-based iterative tropospheric decomposition model'. In: *Remote Sensing of Environment* 204 (2018), pp. 109–121. DOI: 10.1016/j.rse.2017.10.038.

[47] H. Zebker and J. Villasenor. 'Decorrelation in interferometric radar echoes'. In: *IEEE Transactions on Geoscience & Remote Sensing* 30.5 (1992), pp. 950–959. DOI: 10.1109/36.175330.

[48] R. C. Sharma, R. Tateishi, K. Hara, H. T. Nguyen, S. Gharechelou and L. V. Nguyen. 'Earthquake Damage Visualization (EDV) technique for the rapid detection of earthquake-induced damages using SAR data'. In: *Sensors* 17.2 (2017), p. 235. DOI: 10.3390/s17020235.

[49] R. Natsuaki, H. Nagai, N. Tomii and T. Tadono. 'Sensitivity and limitation in damage detection for individual buildings using InSAR coherence—A case study in 2016 Kumamoto earthquakes'. In: *Remote Sensing* 10.2 (2018), p. 245. DOI: 10.3390/rs10020245.

[50] R. Bamler and P. Hartl. 'Synthetic aperture radar interferometry'. In: *Inverse Problems* 14.4 (1998), R1. DOI: 10.1088/0266-5611/14/4/001.

[51] Alaska Satellite Facility (ASF). *ASF Data Search Vertex*. 2025. URL: https://search.asf.alaska.edu/#/ (visited on 24/07/2025).

[52] Alaska Satellite Facility (ASF). *On Demand Sentinel-1 Processing in Vertex*. 2025. URL: https://hyp3-docs.asf.alaska.edu/using/vertex/ (visited on 24/07/2025).

[53] H. Abdi, L. J. Williams *et al.* 'Normalizing data'. In: *Encyclopedia of Research Design* 1 (2010), pp. 935–938.

[54] F. Pedregosa, G. Varoquaux, A. Gramfort, V. Michel, B. Thirion, O. Grisel, M. Blondel, P. Prettenhofer, R. Weiss, V. Dubourg *et al.* 'Scikit-learn: Machine learning in Python'. In: *Journal of Machine Learning Research* 12 (2011), pp. 2825–2830.

[55] C. Geiß, P. A. Pelizari, M. Marconcini, W. Sengara, M. Edwards, T. Lakes and H. Taubenböck. 'Estimation of seismic building structural types using multi-sensor remote sensing and machine learning techniques'. In: *ISPRS J. Photogramm. Remote Sens.* 104 (2015), pp. 175–188. DOI: https://doi.org/10.1016/j.isprsjprs.2014.07.016.

[56] M. Al-Rawashdeh, M. Al Nawaiseh, I. Yousef, M. Bisharah, S. Alkhadrawi and H. Al-Bdour. 'Predicting building damage grade by earthquake: A Bayesian optimization-based comparative study of machine learning algorithms'. In: *Asian Journal of Civil Engineering* 25.1 (2024), pp. 253–264. DOI: 10.1007/s42107-023-00771-6.

[57] S. Ghimire, P. Guéguen, S. Giffard-Roisin and D. Schorlemmer. 'Testing machine learning models for seismic damage prediction at a regional scale using building-damage dataset compiled after the 2015 Gorkha Nepal earthquake'. In: *Earthquake Spectra* 38.4 (2022), pp. 2970–2993. DOI: 10.1177/87552930221106495.

[58] C. Chen, A. Liaw, L. Breiman *et al.* 'Using random forest to learn imbalanced data'. In: *University of California, Berkeley* 110.1-12 (2004), p. 24.

[59] L. Breiman. 'Random forests'. In: *Machine Learning* 45.1 (2001), pp. 5–32. DOI: 10.1023/A:1010933404324.

[60] J. A. Sáez, M. Galar and B. Krawczyk. 'Addressing the overlapping data problem in classification using the one-vs-one decomposition strategy'. In: *IEEE Access* 7 (2019), pp. 83396–83411. DOI: 10.1109/ACCESS.2019.2925300.

[61] M. Sokolova and G. Lapalme. 'A systematic analysis of performance measures for classification tasks'. In: *Information Processing & Management* 45.4 (2009), pp. 427–437. DOI: 10.1016/j.ipm.2009.03.002.

[62] USGS, Earthquake Hazards Program. *Earthquake Hazards 201 - Technical Q&A*. 2019. URL: https://www.usgs.gov/programs/earthquake-hazards/science/earthquake-hazards-201-technical-qa (visited on 06/08/2019).

[63] USGS, Earthquake Hazards Program. *The Modified Mercalli Intensity Scale*. 2025. URL: https://www.usgs.gov/programs/earthquake-hazards/modified-mercalli-intensity-scale (visited on 23/07/2025).

[64] S. Mangalathu, H. Sun, C. C. Nweke, Z. Yi and H. V. Burton. 'Classifying earthquake damage to buildings using machine learning'. In: *Earthquake Spectra* 36.1 (2020), pp. 183–208. DOI: 10.1177/8755293019878137.

[65] K. Kostinakis, K. Morfidis, K. Demertzis and L. Iliadis. 'Classification of buildings' potential for seismic damage using a machine learning model with auto hyperparameter tuning'. In: *Engineering Structures* 290 (2023), p. 116359. DOI: 10.1016/j.engstruct.2023.116359.

[66] L. Li, A. Chang-Richards, M. Boston, K. Elwood and D. Brunsdon. 'A machine learning-supported rapid classification of building damage following the 2010-2011 Canterbury earthquakes'. In: *Journal of Building Engineering* (2025), p. 112807. DOI: 10.1016/j.jobe.2025.112807.

4

ASSESSMENT OF POST-EARTHQUAKE BUILDING RECONSTRUCTION BASED ON MT-INSAR: THE NEPAL CASE STUDY

Evaluating long-term building reconstruction is essential to strengthening resilience to earthquakes. Field investigations provide detailed and accurate information for building assessments, but are often labour-intensive, costly, and time-consuming, particularly when considering the regional-scale impact of earthquakes. In contrast, satellite Remote Sensing (RS) techniques provide frequent data across vast areas, making them ideal for regional-scale post-earthquake assessments, which can complement field surveys. Despite this, most RS studies have relied on manual change detection of satellite data before and after the event, limiting their potential for automated assessment and reducing their support for field investigations. In this chapter, we developed a novel RS method designed to assist field investigations of post-earthquake building reconstruction on a regional scale. The method automatically identifies target buildings for field teams to investigate, locating collapsed structures and those altered by post-earthquake reconstruction efforts. We applied Multi-Temporal Synthetic Aperture Radar Interferometry (MT-InSAR) for the first time to evaluate post-earthquake building reconstruction. The proposed method involves a two-stage analysis: first, a grid-level assessment on a regional scale to detect areas with reconstruction activities following an earthquake, and then a detailed building-level analysis to identify individual buildings that have undergone changes as part of the reconstruction process within these areas. The method was used to assess building reconstruction efforts in Nepal after the 2015 Gorkha earthquake. For the MT-InSAR

The work presented in this chapter was published in Foroughnia, F., Macchiarulo, V., Milillo, P., Whitworth, M.R., Gavin, K. and Giardina, G., 2025. InSAR-based assessment of post-earthquake building reconstruction: The Nepal case study. *International Journal of Applied Earth Observation and Geoinformation*, 144, p.104883.

analysis, we acquired two stacks of 3-m-resolution SAR images, one before and one after the earthquake. The grid-level analysis detected multiple urban areas with significant changes, which were then subjected to a building-level analysis. This analysis pinpointed the locations of affected buildings and determined the extent of changes related to reconstruction activities. A comparison of the building-level results with field observations confirmed that the method successfully identified buildings that have undergone changes. These changes included buildings that were left collapsed, demolished, under construction, or fully reconstructed. The MT-InSAR-based approach introduced in this chapter has the potential to serve as a valuable tool to guide future field surveys related to post-earthquake reconstruction, significantly reducing the time and effort needed for such assessments.

4.1. Introduction

While Chapters 2 and 3 focus on assessing earthquake-induced building damage in the short-term post-event phase, the recovery process extends well beyond the immediate aftermath of an earthquake. A key component of this longer-term phase is the reconstruction of damaged buildings, which may continue for several years and requires systematic assessment to evaluate reconstruction progress and support reconstruction planning.

Post-earthquake reconstruction of buildings involves repairing, reinforcing, or demolishing and rebuilding damaged structures [1]. Typically, this process begins a few months after the earthquake and can last several years [1, 2]. For example, the reconstruction process was still in progress in Bam, Iran, six years after the 2003 earthquake [3]. During the reconstruction process, there is an opportunity to identify and address structural weaknesses, including poor-quality materials and inadequate construction practices, that increase buildings' vulnerability to future disasters [4]. By doing so, it is possible to mitigate risks that could compromise the resilience and sustainability of future buildings, ensuring safer and more resilient structures [5]. Assessment of the reconstruction process ensures it aligns with the established recovery strategy and plans [6, 7]. Additionally, it helps gather lessons to improve future post-disaster management and reconstruction efforts [7].

As discussed in Chapter 1, field-based building assessment is resource-intensive when applied over large affected regions. Similar limitations arise during the reconstruction phase, where conventional monitoring relies on building-by-building inspections [8], household surveys, and interviews [9, 10]. Although these approaches provide detailed, context-specific information on reconstruction progress, their repeated application over several years and across many buildings is required for recovery, a process that demands substantial time, personnel, and resources. Consequently, there is a growing need to explore new methods for post-earthquake assessments that can cover extensive regions more efficiently and help enhance traditional field surveys by identifying priority locations.

As discussed in Chapter 1, Remote Sensing (RS) provides spatially extensive and frequent observations that can complement field-based assessment. Most RS studies have focused on the early phase of assessment, particularly on damage evaluation [11–16] and immediate demolition [12, 17]. Fewer studies have focused on the later

reconstruction phase. These studies have primarily used change detection approaches to identify alterations resulting from reconstruction activities. At broader spatial scales, time-series optical imagery has been used to track reconstruction by classifying built-up areas and measuring changes in them over time. For instance, Landsat observations following the Christchurch, L'Aquila, and Bam earthquakes enabled monitoring of changes in total built-up area over several years [18]. While this approach provides information on the overall progression of reconstruction, it does not identify which individual buildings have changed, limiting its usefulness for supporting targeted field surveys.

In contrast, other research has specifically focused on tracking changes at the level of individual buildings. Four months after the 2010 Haiti earthquake, changes in heavily damaged and collapsed buildings identified by the Global Earth Observation Catastrophe Assessment Network (GEO–CAN) were manually classified into four reconstruction stages: unchanged, rubble removal, under construction, and rebuilding [19]. The reconstruction process was found to vary both spatially and temporally, with most buildings remaining unchanged. This indicated that reconstruction extended beyond the four-month observation period, highlighting the need for longer-term assessment. Longer-term evaluations of post-earthquake building reconstruction have subsequently been conducted using RS techniques. In Bam, Iran, reconstruction following the 2003 earthquake was assessed using high-resolution optical imagery acquired before the earthquake, immediately afterwards, and eight years later, with land-cover changes manually classified within selected areas [20]. Similarly, building-level reconstruction following the 2009 L'Aquila earthquake was assessed by comparing classified building maps derived from optical satellite imagery acquired in 2009 and 2011 using manual and semi-automated change detection methods [21, 22]. While these studies enabled reconstruction to be assessed at the building level, their reliance on manual or semi-automated interpretation makes the assessment time- and labour-intensive.

An alternative to manual interpretation is the use of automated Machine Learning (ML) classification methods for building-level reconstruction assessment. Following the 2007 Peru earthquake, a Maximum Likelihood classification method was applied in Pisco to identify changes in the ratios between buildings and vacant areas from 2007 to 2011 [23]. While automated classification can reduce the reliance on manual interpretation, supervised approaches require representative labelled samples of reconstruction states for model training and validation [24, 25]. Obtaining such reference data over large affected regions and at multiple stages of the reconstruction process may require substantial field-based data collection, limiting the practicality of repeatedly retraining or updating supervised models for long-term reconstruction monitoring.

A well-established method that provides building-level information is Multi-Temporal Synthetic Aperture Radar Interferometry (MT-InSAR), which uses stacks of SAR images. Thanks to the all-weather image acquisition capability of SAR sensors and their ability to cover large areas with short revisit times [16], MT-InSAR can monitor extensive regions affected by earthquakes using frequent SAR data. Additionally, high-resolution SAR data can be freely available through open data programs [26], making it well suited to accurate building-level assessments [16]. The MT-InSAR technique identifies stable points, known as Persistent Scatterers (PSs), by analysing stacks of SAR images taken over time from the

same area. These PSs typically correspond to artificial objects such as buildings, enabling detailed monitoring of changes at the building level. MT-InSAR has been widely used for long-term displacement monitoring in urban areas [27–29]. However, no study has yet explored this technique to assess post-earthquake building reconstruction, nor has it been utilised to support field investigations.

In this study, we aim to develop a novel MT-InSAR-based tool to support post-earthquake field investigations by assessing building reconstruction progress, including buildings that are collapsed, demolished, under construction, or reconstructed. Compared with image-based change detection methods that rely on a single pre-event image and long-term post-event imagery, this approach leverages a time series of SAR data to better capture the gradual and location-specific nature of reconstruction. MT-InSAR enables continuous monitoring of structural changes by detecting variations in PSs associated with buildings over time. This enables automated identification of demolition, collapse, or reconstruction without supplementary datasets, providing a more robust and targeted method for tracking post-disaster building reconstruction. The proposed method can guide field surveys by automatically identifying the locations of buildings that have changed from their pre-event state due to reconstruction efforts or that are still collapsed years after an earthquake. This approach provides target locations for field teams to investigate, significantly reducing the time and effort required for on-site assessments.

The proposed method was used to assess building reconstruction in Nepal following the 2015 Gorkha earthquake. Stacks of high-resolution Cosmo–SkyMed (CSK) SAR images were acquired before and after the earthquake for the MT-InSAR analysis. PSs associated with buildings were identified for both pre- and post-event time frames. A two-stage PS differential analysis was then conducted to locate buildings that had changed. First, a grid-level analysis was performed to determine urban areas that showed significant changes, representing zones of extensive damage or active reconstruction. Second, a building-level PS differential analysis was conducted within these areas to pinpoint specific buildings affected by reconstruction activities. This building-level analysis not only identified the locations of these buildings but also assessed the extent of the changes. Results were validated using field observations collected during reconnaissance missions.

4.2. METHODOLOGY

This section describes the MT-InSAR technique, the parameters used to generate PSs, and the PS differential analysis developed for reconstruction assessment. The proposed method is based on the principle that a PS will cease to persist if its corresponding target undergoes changes, such as collapses or modifications. Using this concept, the study applies a grid-level PS differential analysis at a regional scale, along with a building-level analysis, to detect significant changes and identify building locations that have undergone substantial changes, such as collapse, demolition, or reconstruction.

4.2.1. MULTI-TEMPORAL SYNTHETIC APERTURE RADAR INTERFEROMETRY (MT-INSAR)

MT-InSAR is an advanced RS technique that uses the temporal phase information of SAR data to measure ground surface displacements [30]. The core objective of MT-InSAR is to identify PSs that consistently return strong backscatter signals to the satellite and exhibit stable phase over time [30], typically corresponding to natural features such as rocks or artificial structures like buildings. The MT-InSAR technique uses a stack of SAR images to identify PSs.

To initiate this process, a primary set of points is selected as PS Candidates (PSCs) based on their amplitude stability. This stability is quantified using the Amplitude Dispersion Index (ADI), estimated as:

$$ADI = \frac{\sigma_A}{m_A} \simeq \sigma_v, \tag{4.1}$$

where σ_A is the amplitude standard deviation, m_A is the mean amplitude, and σ_v is the phase standard deviation of the SAR data stack. A point is chosen as a PSC if its amplitude consistently exceeds a defined threshold. [30] proved that assuming sufficient data images, ADI below 0.25 indicates sufficient point stability and a high signal-to-noise ratio.

Once the PSCs are selected, InSAR is used to estimate their displacements. MT-InSAR compares the interferometric phase between a primary image and secondary SAR images of the stack, acquired at different times over the same area. The interferometric phase consists of different components: displacement, topography, atmosphere, the Earth's curvature, and noise [31]. To isolate the displacement component, other phase components are removed, as detailed by [30, 32, 33]. The effects of Earth's curvature and topography are corrected using orbital data and an external Digital Elevation Model (DEM). Depending on the DEM's accuracy, a residual topographic effect may remain in the interferometric phase, which is later estimated with displacements. The atmospheric effect, known as the Atmospheric Phase Screen (APS), is removed based on a two-step procedure. First, a temporal low-pass filter is applied to the residuals to separate unmodeled displacement (temporally correlated) from the atmospheric signal and noise, which are uncorrelated in time. Second, a spatial low-pass filter is used to extract the spatially correlated atmospheric signal from the remaining residuals, effectively isolating and removing the APS [33]. After the APS removal, a second set of PSs is selected using a higher threshold on ADI. Displacements are then re-estimated for all PSs. The amount of remaining noise in the interferometric phase per PS is used to calculate the Temporal Coherence (TC) as a reliability metric. Higher TC values indicate more accurate and stable PS estimates, ensuring the reliability of the analysis.

In this study, the MT-InSAR processing was performed using the SARPROZ software [34]. Although displacement measures were not the primary focus, the complete MT-InSAR process was crucial to identify reliable PSs corresponding to buildings. To select PSCs, we applied a threshold on the Amplitude Stability Index (ASI), implemented in the software as $1 - ADI$. Specifically, ASI values above 0.8 were used in the first processing stage and then reduced to 0.6 for the final PS selection. Only PSs with a TC higher than 0.7 were considered valid for the PS differential analysis. These thresholds are commonly adopted in standard MT-InSAR approaches, as established in the literature

[30, 35, 36]. The following section outlines the PS differential analysis developed in this study to assess building reconstruction.

4.2.2. PERSISTENT SCATTERER (PS) DIFFERENTIAL ANALYSIS

During seismic events, damaged or collapsed buildings no longer exhibit the characteristics of PSs. Normally, an undamaged building maintains a consistent signal to the satellite over time. However, after an earthquake, a severely damaged or collapsed building exhibits irregular and disrupted signals. This disruption occurs because the building either no longer exists in its original form or undergoes further demolition and reconstruction, preventing it from being tracked as a PS. We leveraged this property of PSs to detect changes in buildings, first at a grid level and then at the level of individual structures, as shown in Figure 4.1.

The grid-level analysis aims to identify urban areas that have undergone significant changes in the years following an earthquake. These areas can be prioritised for further evaluation to locate changed buildings through the building-level PS-differential analysis. To perform the grid-level analysis, we divided the area of interest into $100 \times 100 m^2$ grid cells. Within each grid cell, we quantified the number of PSs derived from pre- and post-event time-series images processed with MT-InSAR. The difference in PS numbers at the grid level was determined by subtracting the post-event PS count from the pre-event PS count.

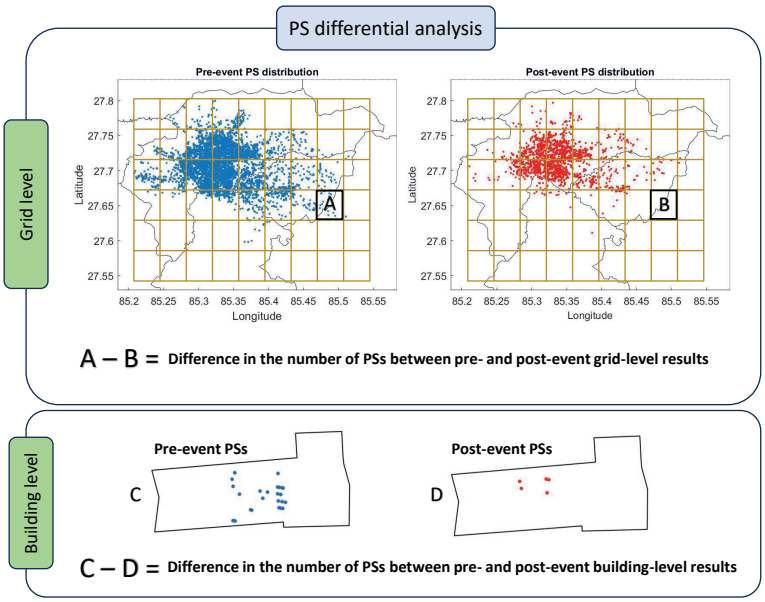

Figure 4.1.: Schematic representation of the PS differential analysis at grid and building levels.

To identify grid cells with significant changes in PS numbers, we normalised these differences to a representative number of PSs from the entire area of interest obtained from the pre-event series (Eq. 4.2). This process involved dividing the number of pre-event data points within each grid cell into equal quartiles and excluding the outliers. The normalisation was based on the upper bound UB of the distribution of the number of PSs within each grid cell (from the pre-event data), defined as the largest data point excluding the outliers, and estimated as follows:

$$UB = Q_3 + 1.5\,(Q_3 - Q_1) \tag{4.2}$$

where Q_1 denotes the first quartile, which is the median of the lower half of the dataset, below which 25% of the data points fall. Similarly, Q_3 is the third quartile, the median of the upper half of the dataset, meaning that 75% of the data points fall below this value. This approach helps prevent outliers from skewing the analysis of PS differences. Figure A.5 in Appendix A illustrates the distribution of the number of PSs obtained from the pre-event time series and the parameter $UB\left(N_{\text{pre}}\right)$. The differences in the number of PSs at the grid level, D_{Grid}, are then estimated as follows:

$$D_{\text{Grid}} = \frac{N_{\text{pre}} - N_{\text{post}}}{UB\left(N_{\text{pre}}\right)} \tag{4.3}$$

where N_{pre} and N_{post} are the number of PSs identified in each grid from the pre- and post-event time series, respectively. $UB\left(N_{\text{pre}}\right)$ refers to the upper bound of the number of points in the grid cells obtained from the pre-event time series. D_{Grid} indicates the relative change between the pre- and post-event conditions in each grid cell, compared to the other grid cells in the area of interest.

The grid-level analysis was designed to prioritise grid cells with more or larger buildings over those with fewer or smaller ones at equivalent levels of PS loss. Since larger buildings and a higher number of buildings typically generate more PSs [30, 37, 38], this approach emphasises grid cells with higher PS counts when similar levels of PS loss are observed. Figure 4.2 provides examples of how the grid-level analysis operates. A grid cell with more pre-event PSs and a certain percentage of point loss due to reconstruction will be prioritised over a grid cell with fewer pre-event PSs in case of the same percentage of point loss. For example, according to Figure 4.2, and assuming $UB\left(N_{\text{pre}}\right)$ is equal to 100 for simplicity, Grid 1 in the first example has 50 points and a 50% point loss (25 points disappeared), resulting in a 25% differential change. In contrast, Grid 2, with 26 points and 13 points disappeared, shows a 13% differential change. In other examples, where the percentage of point losses differs, the differential changes directly depend on the level of point losses. For example, in the same figure, Grid 2, even with 100% point loss, exhibits a smaller differential change (26%) than Grid 1 (40%) with 80% point loss.

Importantly, the $100 \times 100 m^2$ grid resolution was chosen to balance spatial granularity with computational efficiency. The methodology remains robust across different grid sizes because it relies on a normalised change metric that adjusts for variations in the number of PSs per grid. The approach remains flexible and can be adapted to alternative grid configurations depending on specific research needs.

The outcomes of the grid-level analysis served as a guiding framework for a more detailed investigation at the building level. The building-level PS differential analysis

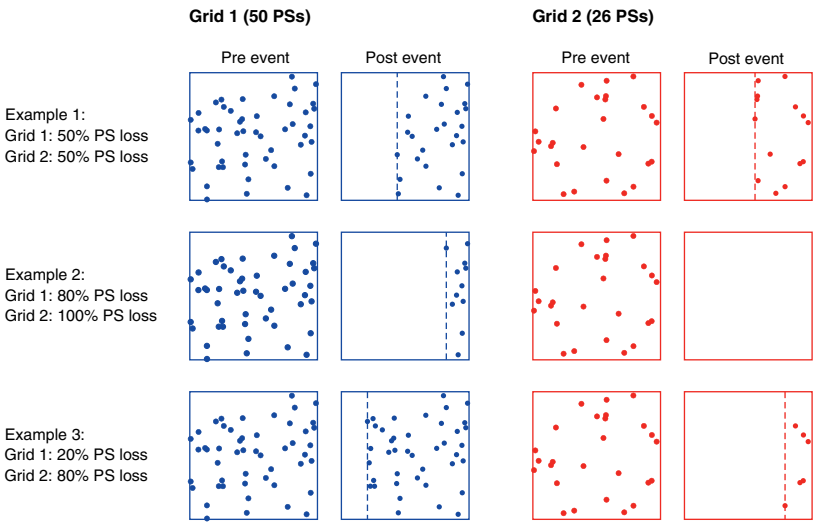

Figure 4.2.: Examples of grid-level differential analysis. In Example 1, 50% of points have disappeared in a denser grid cell due to reconstruction years after the earthquake. Example 2 shows an 80% point loss in Grid 1 compared to a 100% loss in Grid 2. In Example 3, 20% of points in Grid 1 and 80% in Grid 2 have disappeared. The analysis indicates greater changes in the denser Grid 1 for Example 1, while in Examples 2 and 3, the differential changes depend on the degree of point loss in each grid.

identifies buildings that have undergone significant changes during the reconstruction process following the earthquake. These building-level changes can include structures that remain collapsed, have been demolished, are under construction, or are fully reconstructed. We conducted the PS differential analysis for buildings located in zones with high concentrations of grid cells exhibiting significant changes. Building footprints from the OpenStreetMap (OSM) database [39] were used to quantify the presence of PSs within each building for both pre- and post-event data. The change in the number of PSs for each building was estimated by subtracting the post-event count from the pre-event count. Similar to the grid-level analysis, the percentage of PS differences was normalised by the ratio of each building's area and the upper bound of the building area dataset, which acted as a weighting factor.

The percentage of PS differences at the building level, D_{building} was estimated as follows:

$$D_{\text{building}} = \frac{N_{\text{pre-bu}} - N_{\text{post-bu}}}{N_{\text{pre-bu}}} \times \frac{area_{\text{bu}}}{UB\,(area_{\text{bu}})} \times 100, \tag{4.4}$$

where $N_{\text{pre-bu}}$ and $N_{\text{post-bu}}$ are the number of PSs identified from the pre- and pos-event time series for each building footprint, respectively, $area_{\text{bu}}$ represents the area

of each building rooftop, calculated using the OSM building footprints, and $UB(area_{\text{bu}})$ is the upper bound of the building areas distribution (the largest value of areas without outliers) in the detected zones. Similar to the grid-level analysis, this upper bound was calculated using Equation 4.2, but with the building sizes. The values of $UB(area_{\text{bu}})$ used in this study are reported in Table A.1 in Appendix A.

The weighting factor ensures that larger buildings have a greater influence on the magnitude of change associated with reconstruction. For example, a larger building unit will show a higher amount of D_{building} compared to a smaller building with the same normalised difference (as described in the first ratio in Eq. 4.4). Additionally, for buildings with the same area, as in the grid-level analysis, D_{building} depends entirely on the normalised difference, i.e., the percentage of PS point loss during reconstruction. This approach is based on the principle that larger buildings often represent high-value infrastructure and densely populated areas, which can be more critical to overall urban functionality than smaller buildings. By applying a weighting factor based on building area, we ensure that larger buildings receive appropriate emphasis in the analysis. The weighting factor may vary depending on the case study and its specific purposes. For example, if residential buildings are of particular interest, smaller buildings may also be prioritised by defining a different weighting factor. This flexibility allows the method to adapt to different contexts and focus on the most relevant types of buildings.

4.3. CASE STUDY AND DATASETS

On April 25, 2015, Nepal was struck by a moment magnitude (Mw) 7.8 earthquake. The epicentre was situated near Gorkha, approximately 80 km northwest of Kathmandu, the capital city. The earthquake occurred at a focal depth of 19 km [40], and its impact was extensive, resulting in widespread destruction in areas extending from the epicentre to the east, including Kathmandu. Many aftershocks followed the main earthquake, with the largest one occurring on May 12, 2015, recording a moment magnitude of Mw 7.3 [40]. Both urban and rural areas suffered significant damage to buildings and infrastructure from the main shock. By May 26, 2015, the earthquake's toll in Nepal included 8,510 reported deaths and 199 missing people [41].

According to [42], the earthquake caused extensive damage to residential and governmental buildings, heritage sites, schools, roads, bridges, water systems, and agricultural areas. Many ancient cultural buildings were severely damaged or destroyed, along with over 500,000 houses. The Centre for Disaster Management and Risk Reduction Technology [43] estimated the economic loss to be around 10 billion U.S. dollars, which accounted for approximately half of Nepal's gross domestic product [41]. Figure 4.3 shows the selected region of interest, covering the most affected areas in 2015.

4.3.1. REMOTE SENSING DATA

We used Single Look Complex (SLC) from CSK, an Italian constellation of SAR satellites dedicated to Earth imaging. The purpose of this constellation is to provide high-resolution SAR data within the X-band frequency range for various applications, including Earth observation, environmental monitoring, and disaster management [44].

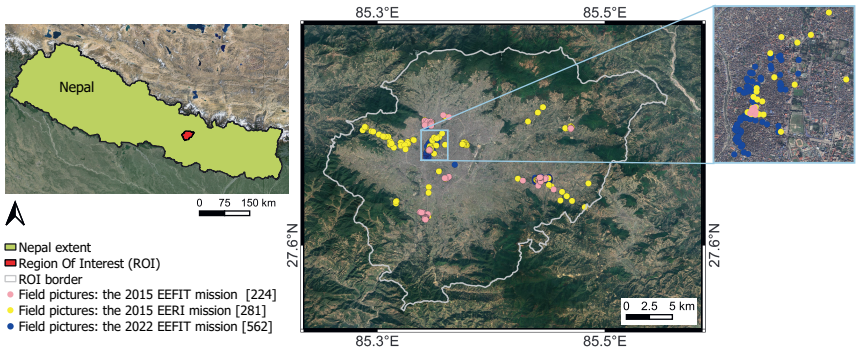

Figure 4.3.: A view of the region of interest, highlighting the locations where field pictures were taken. The close-up image on the right-hand side of the figure shows the distribution of these field pictures within Kathmandu. Google satellite imagery is used as a background layer.

For this study, we collected two temporal series of SAR images in Stripmap mode before and after the event. The post-event time series started following the largest aftershock on May 12, 2015. All images were acquired from a descending orbit in HH polarisation with a minimum revisit time of four days and a spatial resolution of 3 m. The pre-event series comprised 30 SAR images acquired from June 2014 to January 2015. For the post-event series, we considered different time intervals with varying numbers of images to assess the impact of time-series length on the differential analysis. These time intervals were selected to correspond to different phases of reconstruction activities. The shortest post-event time series begins nearly a year after the earthquake, when collapsed buildings may have entered the late stages of reconstruction, such as being under construction or fully reconstructed. The other two time series start closer to the earthquake date and also capture the initial stages of reconstruction, such as debris removal and demolition. Figure 4.4 shows the temporal distribution of the pre-event and post-event time series. The post-event datasets, labelled 1 through 3, consist of 29, 47, and 140 images, respectively. SAR image acquisition dates with corresponding perpendicular and temporal baselines, and Doppler Centroid (DC) relative to the primary image of the post-event series number 2 are reported in Table A.3 in the Appendix.

4.3.2. Field Data

To validate the results, we used field pictures collected by the Earthquake Engineering Research Institute (EERI) and the Earthquake Engineering Field Investigation Team (EEFIT) during their post-reconnaissance missions in 2015, as well as data from the 2022 EEFIT return mission.

EERI is a nonprofit technical society focused on advancing the science and practice of earthquake engineering. It actively contributes to post-earthquake reconnaissance efforts by conducting field investigations to assess the performance of structures and infrastructure following seismic events [45]. EEFIT is a collaborative initiative involving

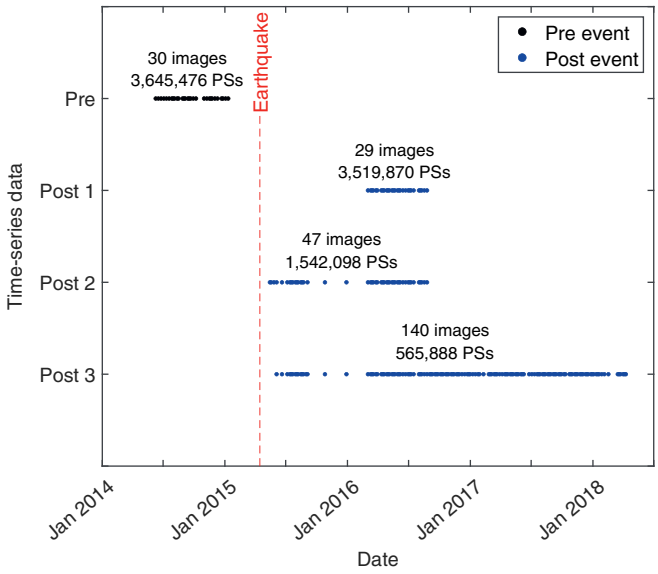

Figure 4.4.: Temporal distribution of CSK data images for the different time series before and after the earthquake. The number of PSs detected with Temporal Coherence higher than 0.7 is specified for each pair.

industry and academic institutions, dedicated to conducting comprehensive field investigations following significant earthquakes.

Two months after the 2015 Gorkha earthquake, EEFIT initiated a reconnaissance mission to investigate the earthquake's on-site impact [46]. In May 2022, EEFIT returned to Nepal for a follow-up mission to gain insights into the country's recovery process and evaluate the effectiveness of the Build Back Better approach to disaster recovery [47]. During their building assessments, the field team had two primary objectives: first, to verify any changes in structures affected by the earthquake, and second, to document the status of these buildings, noting the process of reconstruction efforts. Some of their observations were gathered in Kathmandu and Bhaktapur, where extensive damage was recorded in 2015. The pictures they collected depicted various changes to buildings, including those that had remained collapsed, been demolished, were under reconstruction, or were newly constructed. The locations of the field pictures within the area of interest are represented in Figure 4.3.

4.4. RESULTS

The following sections present the results of the PS differential analysis conducted at both the grid and building levels, along with the validation of the identified buildings using the field data.

4.4.1. GRID-LEVEL ANALYSIS

The MT-InSAR technique was applied to process one pre-event and three distinct post-event CSK datasets, as presented in Figure 4.4. The figure also indicates the number of PSs with TC higher than 0.7 that were identified for each time series used in the PS differential analysis. Due to variations in the number of SAR images in the pre- and post-event time series, the number of PSs identified in each pair differs. This is explained by Eq. 4.1, which indicates that in a longer time series, the likelihood that a point changes (e.g., due to vegetation growth, construction, or other environmental factors) increases, reducing its stability as a PS. In this study, the varying time periods for each pair affect the temporal coverage of building reconstruction activities, which in turn influences the number of PSs associated with buildings as they undergo physical changes. Hereafter, we label the pre- and post-event time-series pairs, each comprising the pre-event dataset paired with one of the post-event datasets, as Pairs 1, 2, and 3.

The outcomes of the PS differential analysis conducted at the grid level are illustrated in Figure 4.5. This analysis provides a regional-scale overview of differences in PS numbers, highlighting significant spatial patterns of changes resulting from reconstruction activities years after the earthquake. Each point in the figure corresponds to a grid cell, with the colour indicating the magnitude of the normalised difference between the pre- and post-earthquake PSs available for that grid cell. The variation in the number of PSs across different time series influences the level of PS changes observed between the pre-event and the three post-event situations.

To effectively highlight areas of significant changes, we categorised the PS differences into three levels using different colour scales: green for small changes, yellow for moderate changes, and red for extensive changes. Due to the variation in the number of PSs across the different time-series pairs (Figure 4.4) and the different patterns of change observed in each pair, the colour scales were adjusted individually for each pair. This approach ensures that the concentration of PS differences is accurately reflected for each period, allowing for a more meaningful comparison of changes across the various time-series pairs.

The results of the grid-level analysis revealed distinct spatial patterns in the distribution of PS differences across the study area (Figure 4.5). The majority of grid cells were classified as small change and were primarily located on the outskirts of urban areas. These regions experienced minimal alterations in PS point density, suggesting little to no reconstruction activities. Some grid cells exhibited moderate changes, indicating urban regions with moderate overall changes. For example, these changes can correspond to structures that sustained moderate damage during the earthquake, followed by moderate levels of repair and modification activities. A significant number of grid cells exhibited extensive changes, primarily in areas where buildings had partially or totally collapsed. These extensive changes in these regions could refer to structures that have collapsed and been demolished or to structures undergoing reconstruction years after the earthquake.

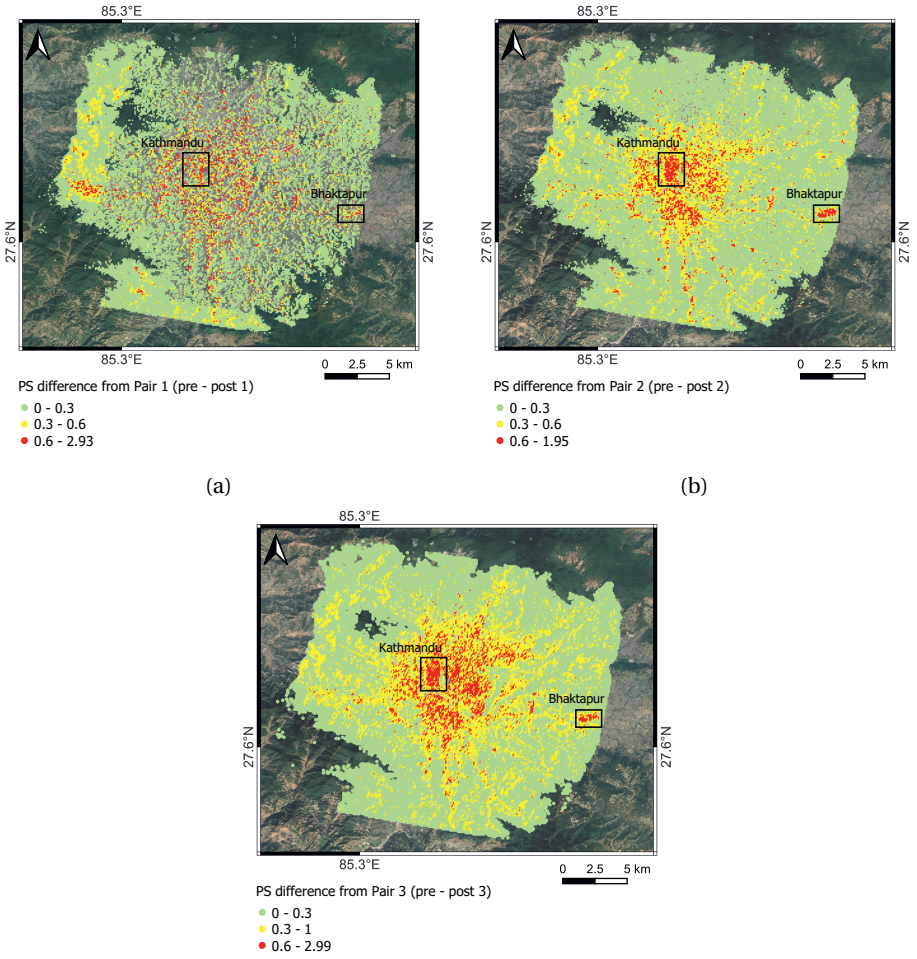

Figure 4.5.: Results of PS differential analysis on the regional scale in Nepal from (a) Pair 1, (b) Pair 2, and (c) Pair 3. Different colour scales were used to highlight the concentration of changed areas on the maps separately. The black rectangles show areas with a high concentration of grid cells with extensive changes, linked with two main affected areas in 2015, one in Kathmandu and one in Bhaktapur.

All pairs, except for Pair 1, show a consistent pattern of changes, with more changes observed in longer series. The extent of detected changes depends on the reconstruction activities during the periods covered by each pair, with buildings showing SAR signal instability throughout reconstruction. For example, Pair 3 has the longest post-event time series, starting about 20 days after the major aftershock and continuing for nearly 3 years. This longer coverage captured more changes associated with long-term reconstruction activities within the area of interest. The extended reconstruction efforts led to a significant reduction in the number of PSs, resulting in more grid cells showing extensive PS differences. This can be due to the gradual modification of collapsed buildings over time, including debris accumulation, debris removal, demolition, and reconstruction. While short gaps between acquisitions could potentially miss rapid reconstruction activities, the overall trend in PS loss still provides a robust indication of reconstruction dynamics.

In contrast, Pair 1, which has the shortest post-event time series, showed a different pattern of changes than the other longer series in the grid-level analysis (Figure 4.5a). This is likely because the post-event time series for Pair 1 started roughly a year after the earthquake and included fewer SAR images (Figure 4.4). As a result, there is a notable gap in data from the critical period immediately following the earthquake to one year later, possibly leaving reconstruction activities unrecorded. Any changes during this one-year gap are not reflected in the time series, limiting the understanding of building conditions. Additionally, shorter time series with fewer SAR images are less capable of capturing gradual reconstruction-related changes.

Figure 4.5 shows that extensive levels of changes are widely distributed across urban areas, with some zones having more grid cells exhibiting extensive changes. In particular, two such zones are located in central Kathmandu and Bhaktapur, as indicated by the black rectangles in Figures 4.5b and 4.5c. These zones were among the areas most severely affected by the earthquake, as confirmed by the field investigations conducted in 2015 [46]. Consequently, these zones were selected for a more detailed building-level analysis, as described in the next section.

4.4.2. BUILDING-LEVEL ANALYSIS

The PS differential analysis at the building level was performed in urban zones (Figure 4.6a) where a significant number of grid cells exhibited extensive changes, as a result of the grid-level analysis described in the previous section.

The distribution of the number of PSs within building footprints from the pre-event and the longest post-event time series is presented in Figure A.6 in Appendix A. As a result of changes in the physical condition of buildings after the event, the number of PSs detected post-event decreased. Figure 4.6 shows the outcomes of building-level PS differential analysis for the zones indicated, using Pair 3. The percentage of PS differences between the pre- and post-event time series was calculated for buildings within the selected zones. These PS differences were categorised into three levels of change, using consistent intervals across all categories. Different colours were used to represent varying levels of changes at the building level. Green represents a small percentage of changes, ranging from 0% to 33%, indicating minimal variations in PS point density associated with the building and suggesting stable building conditions

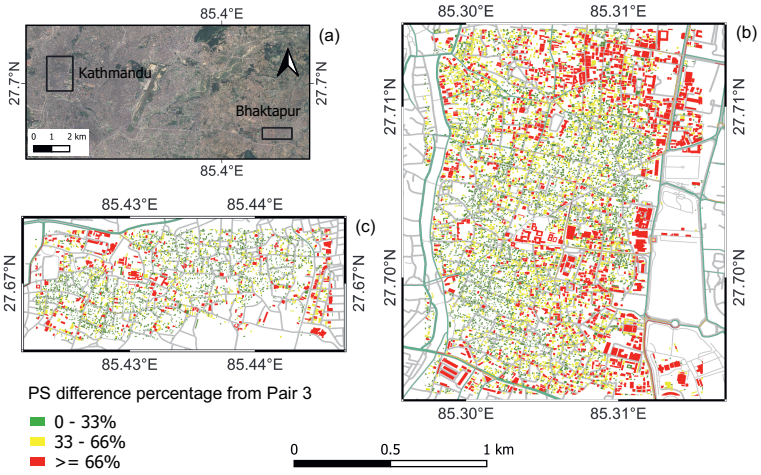

Figure 4.6.: Building-level PS differential results using Pair 3 across (a) two identified areas: (b) Kathmandu and (c) Bhaktapur.

with little to no reconstruction activities. Yellow indicates moderate changes, between 33% and 66%, corresponding to buildings that likely experienced moderate damage during the earthquake or have undergone some level of repair or modification. Red, representing changes above 66%, indicates extensive alterations, signifying buildings that likely suffered severe damage and are either undergoing significant reconstruction or remain damaged or collapsed. The division of the 0–100% range into equal intervals was selected solely for visualisation purposes. Figure 4.6 shows that three years after the earthquake, 58.11%, 29.55%, and 12.34% of the buildings within the regions of interest have experienced small ($0\% \leq D_{\text{building}} < 33\%$), moderate ($33\% \leq D_{\text{building}} < 66\%$), and extensive ($D_{\text{building}} \geq 66\%$) changes, respectively.

4.4.3. VALIDATION OF BUILDING-LEVEL RESULTS

We validated the building-level results using pictures taken by the EEFIT and EERI teams during the 2015 post-event reconnaissance mission and by the EEFIT team during the 2022 return mission. From the 2015 missions, only images of severely damaged or collapsed buildings were selected for validation, as those were the buildings expected to undergo reconstruction. A total of 115 and 59 field pictures were chosen from the 2015 EERI and EEFIT missions, respectively. Additionally, 531 pictures of collapsed, demolished, under-construction, or newly constructed buildings were used from the 2022 EEFIT mission. A total of 152 and 553 pictures were used to validate the results from Kathmandu and Bhaktapur, respectively.

For the validation, we extracted buildings with a relevant level of changes by applying a threshold to the percentage of PS differences at the building level. Specifically, buildings with a PS difference percentage (D_{building}) greater than 50% were selected for validation. The number of identified buildings is reported in Table A.2 in Appendix A. To associate

each field picture with a specific building, we applied a 25-m buffer around each picture's location. If multiple pictures were taken of the same building, the average location of those pictures was used. The 25-m buffer accounted for potential errors, such as the Global Positioning System (GPS) accuracy of the camera for picture locations and the distance between the surveyor and the building being photographed. A picture was considered to correspond to a building if its buffer zone intersected with the building's footprint. This counted as one positive correlation between the picture and the building, indicating a match between the method's identified buildings and the field observation. In cases where a picture intersected with multiple buildings, only one positive correlation was considered to ensure that each picture was associated with a single building.

The accuracy of the results was evaluated by the percentage of buildings detected as having undergone reconstruction, relative to the number of validation pictures. To obtain this, for each area, we calculated the ratio of positive correlations to the total number of validation pictures within the specific regions of interest. Figure 4.7 illustrates the estimated accuracy of the building-level results for each area, i.e., Kathmandu and Bhaktapur, using all pairs. Figure 4.7a shows the percentage of positive correlations per region and per pair. Additionally, Figure 4.7b illustrates the relationship between the accuracy of the building-level results and the duration of the post-event time series. In this graph, the X-axis represents the number of post-event images, while the Y-axis shows the percentage of positive correlations.

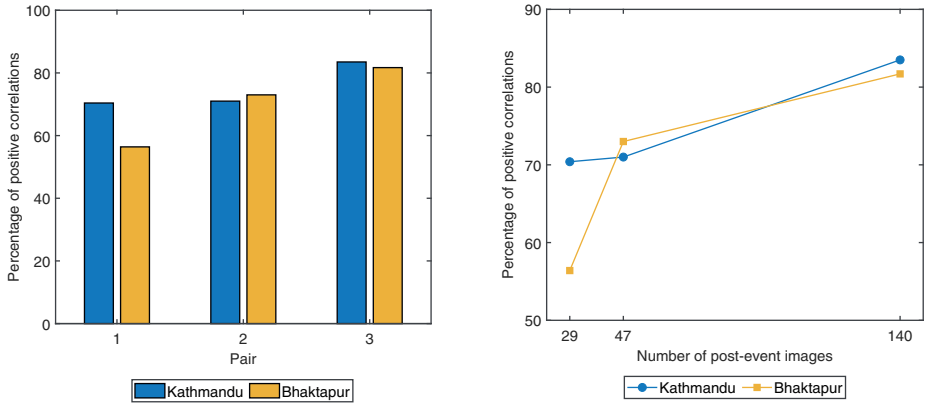

(a) (b)

Figure 4.7.: Accuracy of the building-level results: (a) histogram showing the percentage of positive correlations between field pictures and buildings with over 50% changes per pair and (b) line graph showing the percentage of positive correlations between field pictures and buildings with more than 50% changes, based on varying numbers of post-event images for Kathmandu and Bhaktapur.

The validation results revealed an increasing trend in the percentage of positive correlation across all regions as we progress from Pair 1 to Pair 3. The results from Pair 1, including the shortest post-event series, had fewer matches between the pictures and the buildings with more than 50% changes, resulting in correspondence rates between 56% and 70%. Conversely, Pair 3, which included the longest post-event time series, closely correlated with field observations, with matching rates from 81.7% to 83.5%. This confirms that longer post-event InSAR series are more effective at identifying buildings experiencing significant changes within the regions. The longer the post-event time series, the more changes in building conditions related to reconstruction activities are captured. As a result, more PS losses are detected in the longer time series. Furthermore, in a longer series of SAR images, coherent signal and incoherent noise components of the SAR data can be separated more effectively. This improves the signal-to-noise ratio and enhances the ability to detect changes in the scattering properties of buildings, resulting in more accurate detection of PSs [48] and better identification of changes associated with building reconstruction. The distribution of buildings with more than 50% changes, along with the distribution of field observations, is shown in Figure 4.8.

Figure 4.9 shows examples of field observations that positively correlated with buildings with more than 50% changes. The figure also illustrates the footprint of a reconstructed building with the corresponding PS loss. These positive correlations confirm that the buildings identified by the proposed method as experiencing high levels of change correspond to those observed in the field as undergoing significant post-earthquake modifications. The figure illustrates that the detected buildings are correctly associated with structures that were demolished, are under construction, have been reconstructed, or remain collapsed.

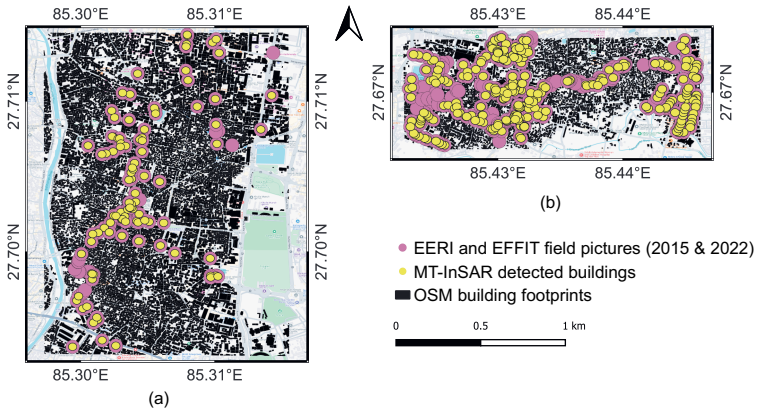

Figure 4.8.: Distribution of the detected buildings, which were in agreement with field pictures for areas (a) Kathmandu and (b) Bhaktapur.

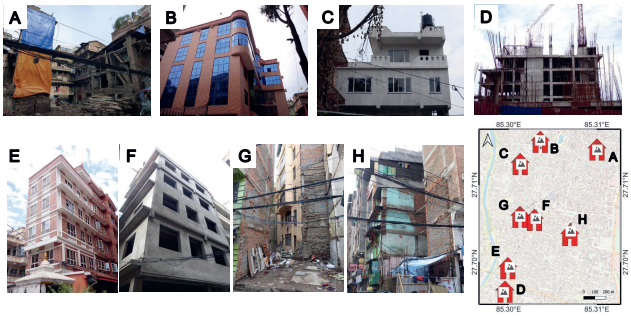

(a)

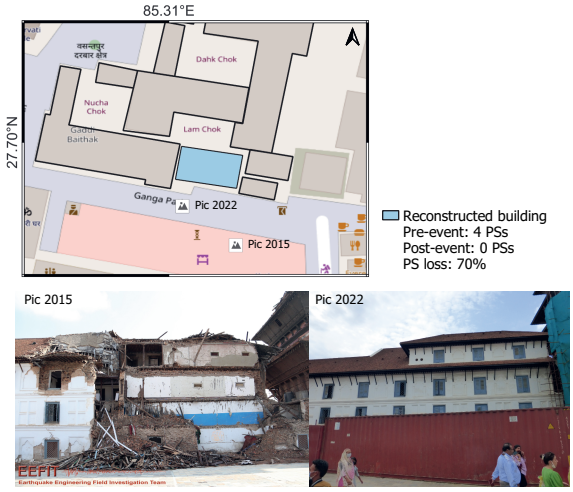

(b)

Figure 4.9.: Examples of surveyed buildings from the 2022 EEFIT mission that correspond to buildings with over 50% change. In (a), Figures A, G, and H correspond to demolished buildings; B, C, and E show reconstructed buildings; and D and F show buildings under construction. (b) An example of a reconstructed building in Kathmandu, showing the building footprint, corresponding field pictures, and the percentage of PS loss.

4.5. DISCUSSION

The research presented in this chapter develops a new RS approach that identifies reconstruction areas at a regional scale, followed by a detailed analysis at the individual building level. The building-level analysis identifies the locations of structures that have undergone reconstruction, particularly those heavily damaged during an earthquake and likely to have been reconstructed afterwards. In fact, the approach is most applicable to changes that alter the external geometry or radar scattering characteristics of buildings. Interventions with limited external manifestation, such as internal strengthening,

retrofitting, or minor repairs, may not produce a sufficiently distinct PS response to be detected.

To date, no studies have developed a tool specifically designed to support field surveys to assess building reconstruction. As confirmed by the validation results, this approach provides a valuable means of guiding field investigations for post-earthquake building reconstruction assessments, allowing on-site surveys to focus solely on identified locations. By pinpointing specific buildings, the tool facilitates more cost-effective, timely, and targeted field data collection during reconstruction assessments. In practical terms, identified building locations can be directly imported into a surveyor's mobile phone application, enabling surveyors to effectively track and visit each building individually. This streamlines the field investigation process by reducing the workload and time required to manually identify target areas. For applications that require only identifying buildings that have undergone substantial changes, the proposed approach can eliminate the need for initial field-based screening. However, where the status of building reconstruction, i.e. buildings that remain collapsed, or were demolished, reconstructed or newly built, is needed, targeted field investigation remains necessary.

A comparison between the proposed method and traditional field survey approaches highlights significant efficiency gains in identifying buildings that have changed over time and in terms of human resources. Specifically for this study, the proposed method, which includes SAR data processing and PS differential analysis, required a total of 32 hours, equivalent to 4 working days for a single person, to analyse 12387 buildings. In contrast, traditional field investigations are far more resource intensive. For instance, the post-earthquake reconnaissance of 5,790 structures in rural Turkish villages took 5 days and required multiple teams [49]. Similarly, [50] reported that the standardised assessment of 23,000 buildings took 60 days and involved 100 inspection teams, amounting to approximately 80,000 person-hours. For identifying buildings that have changed, this comparison demonstrates that the proposed InSAR-based approach offers a scalable and efficient alternative for assessing post-disaster building reconstruction.

The implementation of the proposed method requires a time series of high-resolution SAR imagery acquired before and after an earthquake, along with building footprint data for building-level analysis. Post-event acquisitions should also begin as early as possible to avoid missing reconstruction activities occurring immediately after the earthquake. High-resolution data is essential for individual building assessments [16, 51], particularly when the case study includes small buildings. In this study, we used X-band CSK data with a 3-m-resolution cell size, capturing PSs associated with both small and large buildings within the area of interest. The CSK data demonstrated good performance, successfully identifying buildings of various sizes and reflecting their reconstruction conditions, as shown in Figure 4.6.

The results highlight the importance of carefully selecting the post-earthquake time series period to effectively capture the full dynamics of reconstruction. Pair 1 did not provide reliable insights because its post-event time series began a year after the earthquake and covered only five months. As a result, both the early structural changes and much of the subsequent reconstruction activity were missed. For effective monitoring, the post-event time series should ideally start shortly after the disaster and include 20–25 images [38, 52], which is generally considered the minimum required for

reliable PS detection. Depending on the specific event and the pace of reconstruction, the time series should be extended as much as possible to fully capture all phases of the reconstruction process.

The method is inherently robust against environmental factors, such as vegetation growth, seasonal surface changes, or unrelated infrastructure modifications. It is particularly given its focus on persistent, long-duration changes indicative of post-earthquake reconstruction. These effects are relatively minor compared to the significant structural changes associated with building demolition or reconstruction. At the regional scale, MT-InSAR primarily captures signals from stable, reflective surfaces like buildings, minimising the influence of environmental noise. At the building level, the footprint-based approach further ensures that PS points are directly linked to the structure itself, reducing the likelihood of interference from surrounding vegetation or surface conditions.

Although the PS-selection thresholds adopted in this study follow established MT-InSAR processing practices, the temporal coherence threshold is application-dependent, and variations in this threshold may affect the number and spatial distribution of selected PSs. Future work could therefore investigate the sensitivity of the reconstruction assessment to variations in the temporal coherence threshold. In addition, the robustness of the building-level results could be evaluated by varying the 50% PS-difference criterion used to select buildings with substantial changes for validation.

It is also important to acknowledge that the proposed method involves certain uncertainties. The validation results relied heavily on the accuracy of the camera's GPS, which was used to determine the locations of the on-site pictures. The median horizontal error for high-sensitivity embedded GPS hardware in mobile phones is reported to be between 5 and 8.5 m [53]. As a result, it can sometimes be challenging to determine the exact building from which a picture was captured. In practice, additional spatial uncertainty was introduced because field pictures, although geotagged, were often taken from across the street or at a distance from the target buildings. Furthermore, pictures were captured using different devices with varying GPS accuracies, adding another layer of positional inaccuracy. The 25-meter buffer used in the validation was selected to account for these uncertainties.

Additional sources of uncertainty include layover and PS positioning errors. Layover distortion, which is particularly significant in dense urban areas with tall buildings, can be quantified using the building height and the local incidence angle of the SAR signal. In the absence of airborne Light Detection and Ranging (LiDAR) data for the study area, layover effects were estimated based on reported building heights and the local incidence angle of the central pixel in the SAR images. Assuming an average building height of 12 m [54, 55] and an incidence angle of 26.58 degrees, the average layover-affected area was estimated to be approximately 6 m. Furthermore, the PS positioning error is influenced by the accuracy of the DEM and the spatial resolution of the SAR sensor [56], with errors for the CSK sensor typically ranging within a few meters, ~2.7 m in the azimuth and ~1 m in the slant range directions [57]. Although these distortions may occasionally cause adjacent buildings to be misidentified, the estimated error margins are small enough that field teams can easily compensate for them during on-site inspections.

Finally, the OSM database is not always complete and may lack some building footprints. Consequently, these missing buildings might not be included in the building-level analysis, even if field pictures were obtained for them. The building-level assessment also depends on the positional accuracy of the building footprints used to associate PSs with individual structures. Incomplete or spatially misaligned polygons may exclude PSs belonging to a building or include PSs associated with neighbouring structures, potentially affecting the estimated pre- and post-event PS changes. The sensitivity of the reconstruction results to such footprint errors was not explicitly quantified in this study. Future work could quantify this sensitivity by systematically introducing positional offsets and footprint incompleteness and evaluating their effect on building-level change detection. However, OSM has generally proven to be a reliable base map for urban studies, with several studies showing that its quality is comparable to that of official regional maps [58, 59]. Alternative datasets, such as Microsoft Building Footprints [60] and Open Buildings Data [61], were evaluated but were found to be either less accurate or to require substantial modifications. OSM offered more precise building outlines, particularly for non-rectangular structures. We further validated OSM coverage against Google Earth VHR imagery and found no significant omissions. Therefore, despite its limitations, OSM remained the most appropriate and practical choice for our analysis.

While these uncertainties are present, integrating complementary datasets and techniques could mitigate their impact and enhance the methodology's overall robustness. For example, Building Information Modelling (BIM) datasets, when available, offer detailed architectural information that can validate and enrich SAR-based observations. Alternative georeferencing approaches, such as aligning field photos with high-resolution optical imagery, can reduce GPS-related inaccuracies and improve the spatial accuracy of field validations. Moreover, incorporating ground-truth datasets such as structural health monitoring data, governmental reconstruction reports, or drone-based imaging, if available, can provide further validation data. Furthermore, using datasets from additional earthquake events and extended reconstruction phases could improve its generalisability and applicability across a broader range of scenarios. With sufficient labelled field data, integrating machine learning models into the methodology could be a valuable extension, as these models have demonstrated strong performance in automating classification tasks in remote sensing applications.

Further automation of the framework could be achieved by incorporating ML at the building-level interpretation stage. While the current differential PS analysis automatically identifies buildings exhibiting substantial changes, ML could use features derived from the temporal behaviour of PSs to classify the detected changes into different reconstruction-related states. However, such an approach would still require representative ground-truth data for model training and validation.

The core principle of the proposed method, detecting changes in the number of PSs using MT-InSAR, is scalable and adaptable to various disaster scenarios beyond earthquakes, such as floods, urban fires, and landslides. For instance, in urban fires, severe damage or destruction of buildings leads to significant changes in radar backscatter, as affected structures lose the stability and surface characteristics needed for PS detection. The disappearance of these PSs over time indicates fire-induced damage and subsequent reconstruction. This behaviour is directly observable using the proposed

method and allows for effective post-fire building assessment. As long as a disaster results in substantial physical changes that impact radar reflectivity, the approach remains effective. While some adjustments, such as SAR data selection or temporal baseline tuning, may be necessary, the core concept is widely applicable.

Ultimately, the method provides systematic and scalable monitoring of urban areas in post-disaster scenarios, offering valuable insights to guide field teams, prioritise reconstruction efforts, and assess reconstruction progress over time. This ability to continuously track structural changes and reconstruction dynamics makes the method a valuable tool for long-term urban resilience planning. By analysing trends in building stability across multiple time periods, decision makers can better understand the pace of reconstruction and allocate resources more efficiently.

4.6. CONCLUSION

This chapter introduced a novel method for evaluating post-earthquake building reconstruction. Using the Multi-Temporal Synthetic Aperture Radar Interferometry (MT-InSAR) technique, we detected Persistent Scatterers (PSs) linked to buildings by processing a time series of SAR data collected before and after the earthquake. A two-stage differential analysis was then performed to compare the number of PSs in pre- and post-event scenarios. The method begins with a regional assessment, analysing urban grid cells to identify areas affected by reconstruction after the earthquake. In areas showing the most significant changes, a more detailed building-level analysis was conducted to pinpoint specific buildings that had undergone reconstruction or remained collapsed years after the event. The approach highlights building locations where substantial changes have occurred, either due to continued collapse or to reconstruction. These identified locations can help guide regional-scale field investigations to track reconstruction progress long after the earthquake.

The proposed method was applied to the 2015 Gorkha earthquake in Nepal using stacks of high-resolution Cosmo-SkyMed (CSK) SAR images acquired before and after the event. Through the grid-level analysis, several urban areas showing significant changes were identified, prompting further investigation at the building level. Time-series pairs of different lengths were analysed, revealing that longer time series detected more changes related to reconstruction activities in the PS differential analysis. This is because longer time series can capture a broader range of activities over time, including debris accumulation, removal, and other phases of the reconstruction process. The building-level analysis identified specific locations where buildings had changed years after the earthquake, indicating buildings that remained collapsed, had been demolished, were under construction, or had been reconstructed.

Field observations collected in 2015 and during a return mission to Nepal in 2022 were used to validate the buildings identified by the PS differential analysis. The validation results confirmed that the method successfully located buildings that had changed during the reconstruction phase, either remaining collapsed, being demolished, under construction, or reconstructed. The accuracy was higher with longer time series, suggesting a stronger correlation between the detected buildings and actual field observations. These results confirm the method's reliability in identifying locations

affected by reconstruction activities, providing valuable target areas for future field surveys.

This study marks the first application of the MT-InSAR Remote Sensing (RS) technique to support extensive field investigations, particularly in the context of post-earthquake building reconstruction. It highlights the potential of MT-InSAR to identify buildings affected by reconstruction, offering a practical tool to prioritise locations for field surveys. By doing so, this approach can significantly reduce the time and effort required for extensive investigations of building reconstruction progress across wide areas.

DATA AVAILABILITY

The datasets supporting this study include a combination of commercial, restricted, and publicly available resources. The CSK SAR imagery is proprietary and was used under license from the Italian Space Agency; these data are not available for public distribution but may be requested through the Italian Space Agency portal (https://www.asi.it/en/earth-science/cosmo-skymed/). Field data from the EEFIT for the 2015 and 2022 missions are restricted due to third-party confidentiality agreements and are not publicly available. Publicly accessible field documentation and photographic evidence for the Gorkha earthquake are available through the EERI Learning from Earthquakes archive (https://learningfromearthquakes.org/earthquakes/2015-04-25-nepal/). To support the reproducibility of the analysis, the underlying code and a demonstration dataset containing synthetic data are publicly available on 4TU.ResearchData repository at https://doi.org/10.4121/2a932e92-dc7d-4bd2-b775-a4d8c99b9028.v1.

References

[1] M. Polese, M. Di Ludovico and A. Prota. 'Post-earthquake reconstruction: A study on the factors influencing demolition decisions after 2009 L'Aquila earthquake'. In: *Soil Dynamics and Earthquake Engineering* 105 (2018), pp. 139–149. DOI: 10.1016/j.soildyn.2017.12.007.

[2] Y. Lu and J. Xu. 'Comparative study on the key issues of postearthquake recovery and reconstruction planning: Lessons from the United States, Japan, Iran, and China'. In: *Natural Hazards Review* 16.3 (2015), p. 04014033. DOI: 10.1061/(ASCE)NH.1527-6996.0000172.

[3] B. Omidvar, H. Zafari and S. Derakhshan. 'Reconstruction management policies in residential and commercial sectors after the 2003 Bam earthquake in Iran'. In: *Natural Hazards* 54 (2010), pp. 289–306. DOI: 10.1007/s11069-009-9468-y.

[4] I. Ahmed. 'Resilient housing reconstruction in the developing world'. In: *March A. and Kornakova M. (Eds), Urban Planning for Disaster Recovery*. Elsevier, Butterworth-Heinemann, 2017, pp. 171–188. DOI: 10.1016/B978-0-12-804276-2.00012-8.

[5] M. Lyons, T. Schilderman and C. Boano. *Building back better: Delivering people-centred housing reconstruction at scale*. Practical Action Publishing, 2010.

[6] W. J. Clinton. *Lessons learned from tsunami recovery: Key propositions for building back better*. New York: Office of the UN Secretary-General's Special Envoy for Tsunami Recovery, 2006.

[7] S. Mannakkara, S. Wilkinson and T. R. Francis. '"Build back better" Principles for reconstruction'. In: *Encyclopedia of Earthquake Engineering* (2014), pp. 1–12. DOI: 10.1007/978-3-642-36197-5_343-1.

[8] M. Eghbali, D. Samadian, M. Ghafory-Ashtiany and M. R. Dehkordi. 'Recovery and reconstruction of schools after M 7.3 Ezgeleh-Sarpole-Zahab earthquake; Part II: Recovery process and resiliency calculation'. In: *Soil Dynamics and Earthquake Engineering* 139 (2020), p. 106327. DOI: 10.1016/j.soildyn.2020.106327.

[9] S. Platt, D. Gautam and R. Rupakhety. 'Speed and quality of recovery after the Gorkha earthquake 2015 Nepal'. In: *International Journal of Disaster Risk Reduction* 50 (2020), p. 101689. DOI: 10.1016/j.ijdrr.2020.101689.

[10] L. Westoby, S. Wilkinson and S. Dunn. 'The road to recovery: Understanding the challenges affecting school reconstruction in rural Nepal following the 2015 Gorkha earthquake'. In: *International Journal of Disaster Risk Reduction* 56 (2021), p. 102120. DOI: 10.1016/j.ijdrr.2021.102120.

[11] D. Al-Khudhairy, I. Caravaggi and S. Giada. 'Structural damage assessments from IKONOS data using change detection, object-oriented segmentation, and classification techniques'. In: *Photogrammetric Engineerirng & Remote Sensing* 71.7 (2005), pp. 825–837. DOI: 10.14358/PERS.71.7.825.

[12] D. Brown, K. Saito, M. Liu, R. Spence, E. So and M. Ramage. 'The use of remotely sensed data and ground survey tools to assess damage and monitor early recovery following the 12.5. 2008 Wenchuan earthquake in China'. In: *Bulletin of Earthquake Engineering* 10 (2012), pp. 741–764. DOI: 10.1007/s10518-011-9318-7.

[13] R. Anniballe, F. Noto, T. Scalia, C. Bignami, S. Stramondo, M. Chini and N. Pierdicca. 'Earthquake damage mapping: An overall assessment of ground surveys and VHR image change detection after L'Aquila 2009 earthquake'. In: *Remote Sensing of Environment* 210 (2018), pp. 166–178. DOI: 10.1016/j.rse.2018.03.004.

[14] G. Giardina, V. Macchiarulo, F. Foroughnia, J. N. Jones, M. R. Whitworth, B. Voelker, P. Milillo, C. Penney, K. Adams and T. Kijewski-Correa. 'Combining remote sensing techniques and field surveys for post-earthquake reconnaissance missions'. In: *Bulletin of Earthquake Engineering* (2023), pp. 1–25. DOI: 10.1007/s10518-023-01716-9.

[15] B. Voelker, P. Milillo, A. Tavakkoliestahbanati, V. Macchiarulo, G. Giardina, M. Recla, M. Schmitt, M. Cescon, Y. D. Aktas and E. So. 'The EEFIT remote sensing reconnaissance mission for the February 2023 Turkey earthquakes'. In: *IEEE Journal of Selected Topics in Applied Earth Observations and Remote Sensing* (2024). DOI: 10.1109/JSTARS.2024.3476029.

[16] V. Macchiarulo, G. Giardina, P. Milillo, Y. D. Aktas and M. R. Whitworth. 'Integrating post-event very high resolution SAR imagery and machine learning for building-level earthquake damage assessment'. In: *Bulletin of Earthquake Engineering* (2024), pp. 1–27. DOI: 10.1007/s10518-024-01877-1.

[17] Y. Kushiyama and M. Matsuoka. 'Time series GIS map dataset of demolished buildings in Mashiki town after the 2016 Kumamoto, Japan earthquake'. In: *Remote Sensing* 11.19 (2019), p. 2190. DOI: 10.3390/rs11192190.

[18] S. Derakhshan, S. L. Cutter and C. Wang. 'Remote sensing derived indices for tracking urban land surface change in case of earthquake recovery'. In: *Remote Sensing* 12.5 (2020), p. 895. DOI: 10.3390/rs12050895.

[19] J. Bevington, S. Pyatt, A. Hill, M. Honey, B. Adams, R. Davidson, S. Brink, S. Chang, D. Panjwani, R. Mills, P. Amyx and R. T. Eguchi. *Uncovering community disruption using remote sensing: An assessment of early recovery in post-earthquake Haiti*. Tech. rep. Disaster Research Center, 2010. URL: http://udspace.udel.edu/handle/19716/5850.

[20] S. O. Hashemi Parast, F. Yamazaki and W. Liu. 'Monitoring and evaluation of the urban reconstruction process in Bam, Iran, after the 2003 Mw 6.6 earthquake'. In: *Natural Hazards* 85 (2017), pp. 197–213. DOI: 10.1007/s11069-016-2573-9.

[21] D. Contreras, T. Blaschke, D. Tiede and M. Jilge. 'Monitoring recovery after earthquakes through the integration of remote sensing, GIS, and ground observations: The case of L'Aquila (Italy)'. In: *Cartography and Geographic Information Science* 43.2 (2016), pp. 115–133. DOI: 10.1080/15230406.2015.1029520.

[22] D. Contreras, G. Forino and T. Blaschke. 'Measuring the progress of a recovery process after an earthquake: The Case of L'aquila, Italy'. In: *Internationl Journal of Disaster Risk Reduction* 28 (2018), pp. 450–464. DOI: 10.1016/j.ijdrr.2017.09.048.

[23] T. Hoshi, O. Murao, K. Yoshino, F. Yamazaki and M. Estrada. 'Post-disaster urban recovery monitoring in Pisco after the 2007 Peru earthquake using satellite image'. In: *Journal of Disaster Research* 9.6 (2014), pp. 1059–1068. DOI: 10.20965/jdr.2014.p1059.

[24] S. S. Matin and B. Pradhan. 'Challenges and limitations of earthquake-induced building damage mapping techniques using remote sensing images - A systematic review'. In: *Geocarto International* 37.21 (2022), pp. 6186–6212. DOI: 10.1080/10106049.2021.1933213.

[25] J. Jia and W. Ye. 'Deep learning for earthquake disaster assessment: Objects, data, models, stages, challenges, and opportunities'. In: *Remote Sensing* 15.16 (2023), p. 4098. DOI: 10.3390/rs15164098.

[26] ESA. *European Space Agency: COSMO-SkyMed Full Archive and Tasking*. 2024. URL: https://earth.esa.int/eogateway/catalog/cosmo-skymed-full-archive-and-tasking (visited on 18/06/2024).

[27] A. Ciampalini, F. Bardi, S. Bianchini, W. Frodella, C. Del Ventisette, S. Moretti and N. Casagli. 'Analysis of building deformation in landslide area using multisensor PSInSAR™ technique'. In: *International Journal of Applied Earth Observation and Geoinformation* 33 (2014), pp. 166–180. DOI: 10.1016/j.jag.2014.05.011.

[28] S. Bianchini, F. Pratesi, T. Nolesini and N. Casagli. 'Building deformation assessment by means of persistent scatterer interferometry analysis on a landslide-affected area: The Volterra (Italy) case study'. In: *Remote Sensing* 7.4 (2015), pp. 4678–4701. DOI: 10.3390/rs70404678.

[29] F. Foroughnia, S. Nemati, Y. Maghsoudi and D. Perissin. 'An iterative PS-InSAR method for the analysis of large spatio-temporal baseline data stacks for land subsidence estimation'. In: *International Journal of Applied Earth Observation and Geoinformation* 74 (2019), pp. 248–258. DOI: 10.1016/j.jag.2018.09.018.

[30] A. Ferretti, C. Prati and F. Rocca. 'Permanent scatterers in SAR interferometry'. In: *IEEE Transactions on Geoscience & Remote sensing* 39.1 (2001), pp. 8–20. DOI: 10.1109/36.898661.

[31] R. F. Hanssen. *Radar interferometry: data interpretation and error analysis*. Springer, 2001. DOI: 10.1007/0-306-47633-9.

[32] D. Perissin and T. Wang. 'Repeat-pass SAR interferometry with partially coherent targets'. In: *IEEE Transactions on Geoscience & Remote Sensing* 50.1 (2011), pp. 271–280. DOI: 10.1109/TGRS.2011.2160644.

[33] F. J. Van Leijen. 'Persistent scatterer interferometry based on geodetic estimation theory'. PhD thesis. Delft University of Technology, 2014. DOI: 10.4233/uuid:5dba48d7-ee26-4449-b674-caa8df93e71e.

[34] D. Perissin, Z. Wang and T. Wang. 'The SARPROZ InSAR tool for urban subsidence/manmade structure stability monitoring in China'. In: *Proceedings of the ISRSE, Sidney, Australia* 1015 (2011).

[35] V. Macchiarulo, P. Milillo, C. Blenkinsopp, C. Reale and G. Giardina. 'Multi-temporal InSAR for transport infrastructure monitoring: Recent trends and challenges'. In: *Proceedings of the Institution of Civil Engineers-Bridge Engineering*. Vol. 176. 2. Thomas Telford Ltd. 2021, pp. 92–117. DOI: 10.1680/jbren.21.00039.

[36] S. Wu, B. Zhang, X. Ding, N. Shahzad, L. Zhang and Z. Lu. 'A hybrid method for MT-InSAR phase unwrapping for deformation monitoring in urban areas'. In: *International Journal of Applied Earth Observation and Geoinformation* 112 (2022), p. 102963. DOI: 10.1016/j.jag.2022.102963.

[37] A. Hooper, H. Zebker, P. Segall and B. Kampes. 'A new method for measuring deformation on volcanoes and other natural terrains using InSAR persistent scatterers'. In: *Geophysical Research Letters* 31.23 (2004). DOI: 10.1029/2004GL021737.

[38] M. Crosetto, O. Monserrat, M. Cuevas-González, N. Devanthéry and B. Crippa. 'Persistent scatterer interferometry: A review'. In: *ISPRS Journal of Photogrammetry and Remote Sensing* 115 (2016), pp. 78–89. DOI: 10.1016/j.isprsjprs.2015.10.011.

[39] OpenStreetMap. 2023. URL: https://www.openstreetmap.org (visited on 01/06/2020).

[40] USGS. *M 7.8 - 67 km NNE of Bharatpur, Nepal*. 2015. URL: https://earthquake.usgs.gov/earthquakes/eventpage/us20002926/executive (visited on 02/07/2015).

[41] K. Goda, T. Kiyota, R. M. Pokhrel, G. Chiaro, T. Katagiri, K. Sharma and S. Wilkinson. 'The 2015 Gorkha Nepal earthquake: insights from earthquake damage survey'. In: *Frontiers in Built Environment* 1 (2015), p. 153814. DOI: 10.3389/fbuil.2015.00008.

[42] B. Lizundia, S. N. Shrestha, J. Bevington, R. Davidson, K. Jaiswal, G. K. Jimee, H. Kaushik, H. Kumar, J. Kupec, J. Mitrani-Reiser *et al. EERI earthquake reconnaissance team report: M7. 8 Gorkha, Nepal earthquake on April 25, 2015 and its aftershocks*. Tech. rep. EERI, Oakland, CA, USA, 2016.

[43] CEDIM. *Nepal Earthquakes – Report 3*. 2015. URL: https://www.cedim.de/english/index.php (visited on 02/07/2015).

[44] Italian Space Agency. 'COSMO-SkyMed mission and products description'. In: *Doc. N° ASI-CSM-PMG-NT-001, 8 July 2019, Issue 3* (2019).

[45] EERI. *Nepal Earthquake Clearinghouse*. 2015. URL: https://learningfromearthquakes.org/2015-04-25-nepal (visited on 18/07/2023).

[46] S. Wilkinson, M. DeJong, V. Novelli, P. Burton, S. Tallet-Williams, M. Whitworth, F. Guillermo, T. White, A. Trieu, B. Ghosh and S. Datla. *The Mw 7.8 Gorkha, Nepal earthquake of 25 April 2015: A field report by EEFIT*. Tech. rep. EEFIT, 2019.

[47] M. R. Whitworth, J. Pattison, G. Giardina, D. M. Contreras Mojica, R. K. Adhikari, S. Wilkinson, F. Foroughnia, V. Macchiarulo, P. Jaquin, P. Burton, K. Dönmez, G. Franco, S. Sharma, P. Milillo, K. Chandra and J. Jones. 'Shared knowledge on earthquake recovery and reconstruction: The Nepal EEFIT 2022 return mission'. In: *SECED 2023 Conference Earthquake Engineering & Dynamics for a Sustainable Future* (2023).

[48] D. D'Aria, A. Ferretti, A. M. Guarnieri and S. Tebaldini. 'SAR calibration aided by permanent scatterers'. In: *IEEE Transactions on Geoscience & Remote Sensing* 48.4 (2009), pp. 2076–2086. DOI: 10.1109/TGRS.2009.2033672.

[49] R. Livaoğlu, M. Ö. Timurağaoğlu, C. Serhatoğlu and M. S. Döven. 'Damage during the 6–24 February 2017 Ayvacık (Çanakkale) earthquake swarm'. In: *Natural Hazards and Earth System Sciences* 18.3 (2018), pp. 921–934. DOI: 10.5194/nhess-18-921-2018.

[50] A. Goretti and G. Di Pasquale. 'Building inspection and damage data for the 2002 Molise, Italy, earthquake'. In: *Earthquake Spectra* 20.1_suppl (2004), pp. 167–190. DOI: 10.1193/1.1769373.

[51] H. Miura, S. Midorikawa and M. Matsuoka. 'Building damage assessment using high-resolution satellite SAR images of the 2010 Haiti earthquake'. In: *Earthquake Spectra* 32.1 (2016), pp. 591–610. DOI: 10.1193/033014eqs042m.

[52] C. Colesanti, A. Ferretti, F. Novali, C. Prati and F. Rocca. 'SAR monitoring of progressive and seasonal ground deformation using the permanent scatterers technique'. In: *IEEE Transactions on Geoscience & Remote Sensing* 41.7 (2003), pp. 1685–1701. DOI: 10.1109/TGRS.2003.813278.

[53] P. A. Zandbergen and S. J. Barbeau. 'Positional accuracy of assisted GPS data from high-sensitivity GPS-enabled mobile phones'. In: *Journal of Navigation* 64.3 (2011), pp. 381–399. DOI: 10.1017/S0373463311000051.

[54] H. Chaulagain, H. Rodrigues, E. Spacone, H. Varum *et al.* 'Seismic response of current RC buildings in Kathmandu valley'. In: *Structural Engineering and Mechanics* 53.4 (2015), pp. 791–818. DOI: 10.12989/sem.2015.53.4.791.

[55] T. Ohsumi, Y. Mukai and H. Fujitani. 'Investigation of damage in and around Kathmandu Valley related to the 2015 Gorkha, Nepal earthquake and beyond'. In: *Geotechnical and Geological Engineering* 34 (2016), pp. 1223–1245. DOI: 10.1007/s10706-016-0023-9.

[56] N. Dörr, A. Schenk and S. Hinz. 'Analysis of heterogeneous PS-InSAR derived subsidence rates using categorized GIS objects-A case study in the Mekong Delta'. In: *2021 IEEE IGARSS*. IEEE. 2021, pp. 2655–2658. DOI: 10.1109/IGARSS47720.2021.9553297.

[57] D. O. Nitti, R. Nutricato, R. Lorusso, N. Lombardi, F. Bovenga, M. F. Bruno, M. T. Chiaradia and G. Milillo. 'On the geolocation accuracy of COSMO-SkyMed products'. In: *SAR Image Analysis, Modeling, and Techniques XV*. Vol. 9642. SPIE. 2015, pp. 69–80. DOI: 10.1117/12.2196870.

[58] H. Fan, A. Zipf, Q. Fu and P. Neis. 'Quality assessment for building footprints data on OpenStreetMap'. In: *International Journal of Geographical Information Science* 28.4 (2014), pp. 700–719. DOI: 10.1080/13658816.2013.867495.

[59] M. A. Brovelli and G. Zamboni. 'A new method for the assessment of spatial accuracy and completeness of OpenStreetMap building footprints'. In: *ISPRS International Journal of Geo-Information* 7.8 (2018), p. 289. DOI: 10.3390/ijgi7080289.

[60] Microsoft. *Global ML Building Footprints*. 2025. URL: https://github.com/microsoft/GlobalMLBuildingFootprints (visited on 08/04/2025).

[61] Open Buildings. *Open Buildings*. 2025. URL: https://sites.research.google/gr/open-buildings (visited on 08/04/2025).

5

CONCLUSIONS AND RECOMMENDATIONS

This thesis aimed to develop Remote Sensing (RS)-based methodologies for regional-scale assessment of post-earthquake building conditions, addressing both the short-term evaluation of multi-level damage and the longer-term monitoring of reconstruction. The research addressed the limitations of traditional on-site and image-based assessments of building damage by using differential airborne Light Detection and Ranging (LiDAR), SAR Interferometry (InSAR), and Machine Learning (ML) techniques. The research advances scalable and operational methodologies that bridge short-term emergency response with sustained reconstruction tracking.

Through three core methodological developments, this thesis demonstrated that:

1. RS techniques provide an effective means for time-efficient, regional-scale post-earthquake building assessments, overcoming many of the limitations of traditional on-site surveys. Their advantage lies in satellite missions' ability to deliver wide spatial coverage, frequent revisit times, and timely observations, thereby enabling large-area monitoring after an event (Chapters 2 and 3).

2. Differential LiDAR analysis enables accurate three-dimensional measurements of earthquake-induced building displacements, which can be directly translated into residual displacements and drift ratios. These quantitative LiDAR indicators can reveal not only severe but also moderate levels of building damage (Chapter 2).

3. InSAR displacement and coherence, when integrated with structural and site-related features within an ML framework, can achieve scalable, multi-level building damage classification (Chapter 3).

4. InSAR-derived features can serve as alternatives to traditional seismic intensity measures such as Peak Ground Velocity (PGV) and Peak Ground Acceleration (PGA), which might be unavailable due to their reliance on sparse ground-based stations (Chapter 3).

5. Multi-Temporal InSAR (MT-InSAR) time-series analysis can be used to systematically identify and monitor reconstruction dynamics at both regional and building levels. This approach enables the identification of buildings that remain collapsed, are under construction, have been demolished, or have already been reconstructed (Chapter 4).

6. The reconstruction assessment methodology proposed in this thesis, grounded in the MT-InSAR technique, can guide on-site investigators by identifying buildings that require field inspection, thereby significantly reducing the time and effort needed for post-earthquake surveys (Chapter 4).

Together, these developments establish a coherent set of complementary methodologies for post-earthquake damage assessment and reconstruction monitoring using RS data.

5.1. ANSWERS TO RESEARCH QUESTIONS

The findings of this thesis address the research questions formulated in Chapter 1. The questions were designed to reflect the different assessment objectives required across the

post-earthquake timeline, distinguishing between short-term damage evaluation and long-term reconstruction monitoring. Each research question is answered through the development and application of phase-specific RS methodologies, as detailed below.

(1) **How can RS–derived indicators of structural response be used as physically interpretable measures of short-term earthquake damage?**

This thesis demonstrated that RS-derived building displacements provide a physically interpretable and quantitative basis for short-term earthquake damage assessment. Permanent displacements measured after seismic events reflect the structural response of buildings to ground motion and are directly related to damage mechanisms such as residual drift and differential deformation. Unlike image-based approaches that rely on visual damage proxies or coherence loss, displacement-based indicators provide information about the physical deformation of structures, enabling a more physically interpretable and mechanism-informed assessment of damage. The assessment, therefore, focuses on damage that produces sufficient permanent deformation to be reflected in the measured displacement of the building. Damage mechanisms associated with limited or no permanent deformation, such as localised cracking or connection failures, might not be directly represented by these displacement-based indicators.

In Chapter 2, using pre- and post-event LiDAR data, lateral and vertical roof displacements were quantified to infer residual structural response and link it directly to damage severity. These physically interpretable indicators enabled the identification of multiple damage states at both the building and regional scales. Recognising the limited spatial and temporal availability of LiDAR data, the thesis further employed spaceborne Synthetic Aperture Radar (SAR) observations to extend displacement-based damage assessment to larger regions. Displacements derived through the InSAR technique were integrated with structural and site-related features within an ML-based classification framework, enabling automated and scalable multi-level damage assessment, as demonstrated in Chapter 3.

The results show that indicators capturing structural response, specifically building displacements, provide valuable information for assessing intermediate damage states that are often difficult to detect through visual inspection alone. However, Moderate Damage remained the most challenging class to distinguish, highlighting the limited separability of intermediate damage states and the need for further refinement of their classification. By linking remotely sensed displacements to structural performance concepts, the proposed methodologies provide a meaningful and scalable indicator of damage severity suitable for time-efficient post-earthquake assessment at both building and regional scales. Collectively, the use of LiDAR- and InSAR-derived displacements highlights their central role in short-term building damage assessment and advances beyond conventional RS studies that have primarily focused on severe damage or collapse.

(2) **How can LiDAR-based observations be used to quantify multi-level building damage at regional scales?**

The results of this thesis demonstrated that LiDAR-based displacement measurements can be systematically used to quantify multi-level earthquake-induced building damage at regional scales. In Chapter 2, a quantitative damage assessment methodology was developed that integrates differential three-dimensional point cloud analysis with structural

engineering principles to derive physically interpretable displacement indicators at the building level.

Pre- and post-event LiDAR point clouds were aligned using the Iterative Closest Point (ICP) algorithm to extract three-dimensional displacement vectors for individual buildings. These displacement measurements were subsequently translated into residual displacements and drift-related indicators, which are directly linked to established structural damage states. By applying physically interpretable thresholding criteria to these indicators, buildings were consistently and objectively classified into multiple damage levels.

Application of the methodology to the 2014 Napa Valley earthquake demonstrated that LiDAR-based displacement indicators enable reliable identification of moderate damage levels that are often difficult to detect solely through visual inspection or image-based change detection. The inferred damage levels represent deformation-based estimates of damage severity, as the adopted residual-drift indicator reflects global permanent building deformation rather than directly representing all possible damage mechanisms. Localised damage, connection failures, or other damage mechanisms that do not produce significant permanent deformation at the whole-building level may therefore not be adequately reflected in this indicator. The applicability of the approach depends on the availability of sufficiently dense and accurately registered pre- and post-event LiDAR data, which may not always be available following an earthquake. The case study predominantly comprised timber-frame buildings, with most exhibiting moderate damage and relatively few cases of severe damage or collapse. The demonstrated performance should therefore be interpreted in this context, and further validation across a more diverse range of structural typologies and damage states is required to establish the methodology's wider applicability. Nevertheless, when sufficient pre- and post-event coverage is available, the results confirmed the potential of LiDAR-derived displacement indicators for regional-scale, multi-level damage quantification, extending the role of LiDAR from qualitative damage mapping to quantitative structural performance assessment.

(3) **How can SAR-based features be employed to improve the detection and classification of multi-level building damage?**

Chapter 3 demonstrated that SAR observations can be effectively employed to improve the detection and classification of multi-level building damage through the combined use of interferometric displacement, coherence, and associated building- and site-related variables. Rather than relying on a single SAR-derived observable, the methodology exploits complementary seismic indicators extracted from SAR data to capture different manifestations of earthquake-induced damage.

To address variability across urban environments and seismic events, two learning strategies were developed. The first strategy, region-specific learning, trains classification models independently for each study area, allowing the learning process to adapt to local building characteristics and seismic response conditions. The second strategy, combined learning, integrates data from multiple earthquake events and regions into a single training dataset, enabling the development of a generalised model that captures damage patterns across the different geographic and structural conditions represented in the combined dataset.

Within both learning strategies, the classification models were trained using InSAR-derived seismic indicators, specifically Line-of-Sight (LOS) displacement and coherence, together with available building attributes and site-related variables. The building attributes include parameters such as building age, typology, floor surface, and number of storeys. At the same time, site-related variables account for local soil and geographic effects, including time-averaged shear-wave velocity to a depth of 30 m (Vs30), distance to the epicentre, and terrain slope.

A key finding of Chapter 3 is that incorporating InSAR-derived displacement provides physically meaningful information that significantly improves sensitivity to multiple damage states. This addresses a persistent limitation in prior RS-based damage assessment approaches, which predominantly rely on roof-level observations or image-derived features and therefore tend to focus on binary collapse/non-collapse classification rather than true multi-level damage characterisation. Nevertheless, moderate damage remained the most challenging class to distinguish. This difficulty can be attributed in part to the intermediate nature of this damage state, which results in overlapping characteristics with both no-damage and severe-damage states within the available feature space. In addition, uncertainty in assigning damage levels during field inspections may increase ambiguity near the boundaries between damage states, particularly for intermediate damage levels. Further improvements could be achieved through higher-resolution InSAR observations, three-dimensional displacement decomposition, and the integration of complementary data sources, such as optical imagery, LiDAR, and more detailed building inventory information, as discussed in Chapter 3.

Application of the proposed methodology to the 2015 Gorkha and 2016 Central Italy earthquakes demonstrated consistent and robust classification performance across different urban settings. The results confirm that exploiting multiple SAR-based seismic observables through appropriately designed learning strategies enables scalable, regional-scale damage assessment across diverse seismic and structural contexts, without reliance on external data sources, such as optical imagery. However, the regional differences in performance also showed that classification depends on the characteristics and quality of the available datasets, building stock, and damage patterns. In the case studies considered in this thesis, building-related attributes were obtained from field-derived datasets. For future applications, the developed models provide a basis for transferring the learned relationships to new earthquake events rather than training a new model entirely from scratch. A model trained on existing earthquake datasets could be adapted or calibrated to the conditions of a new event using a smaller amount of representative event-specific data, while the required building-related attributes could be obtained from available building inventories, cadastral records, open geospatial databases, or other regional data sources. This transfer to an unseen earthquake was not evaluated in the present thesis and therefore remains an important direction for future research.

(4) **How can regional-scale damage assessment be achieved using SAR-based information when detailed ground-based seismic data are unavailable?**

This thesis demonstrated that regional-scale damage assessment can be achieved using SAR-based displacement information when detailed ground-based seismic data are unavailable or sparse. Conventional seismic intensity measures such as PGV and PGA rely on dense networks of ground sensors, which might be lacking in earthquake-

prone regions. In contrast, satellite-based SAR observations provide spatially continuous measurements that are independent of ground instrumentation.

As demonstrated in Chapter 3, InSAR-derived displacement was used as an alternative indicator of seismic impact to conventional ground-based seismic measures such as PGA and PGV, and integrated within a data-driven classification framework to enable consistent damage assessment across large regions. By exploiting the spatial continuity and repeat-pass capability of satellite SAR data, the proposed approach supports damage mapping where detailed ground-based seismic observations are unavailable. The framework, therefore, does not require PGA or PGV observations but does require relevant building- and site-related information in addition to the InSAR-derived features. Validation across multiple earthquake case studies confirmed that SAR-based displacement indicators can effectively replace or complement traditional seismic intensity measures, enabling time-efficient and scalable damage assessment in data-scarce environments.

(5) **How can time-series SAR observations be systematically used to identify and monitor post-earthquake reconstruction processes?**

Chapter 4 addressed long-term post-earthquake reconstruction monitoring using time-series SAR observations derived from MT-InSAR analysis. Reconstruction was treated as a distinct assessment phase, characterised by gradual, progressive changes in the built environment, rather than as an immediate structural response to seismic loading. During this phase, changes in building geometry, surface properties, and construction activity manifest through variations in radar scattering behaviour over time, making multi-temporal SAR observations particularly suitable for reconstruction assessment.

To systematically capture these processes, a two-stage assessment strategy was developed. The first stage consisted of a regional-scale screening, in which urban areas were divided into grid cells to detect zones exhibiting significant temporal changes in Persistent Scatterer (PS) distributions. This step enabled the identification of neighbourhoods most affected by reconstruction activity, demolition, or ongoing structural collapse, providing an efficient means of prioritising areas for more detailed analysis.

In the second stage, the assessment was refined to the building level to identify individual structures exhibiting substantial changes in PS behaviour. By comparing pre- and post-event SAR time series, the methodology captured variations in building reflectivity and stability associated with different reconstruction states. This enabled the automatic identification of buildings that experienced substantial changes following the earthquake. Such changes may be associated with collapse, demolition, construction, or major reconstruction that substantially modifies building geometry or radar scattering characteristics. The scope of the methodology does not extend to interventions that do not produce substantial changes in PS behaviour. Therefore, activities such as internal strengthening, retrofitting, or minor repairs that leave the external geometry and radar scattering characteristics largely unchanged are not assessed by the proposed approach.

The methodology was applied to the Nepal Gorkha earthquake case study, where the results showed strong agreement with available field surveys and independent observations. The case study demonstrated that the MT-InSAR analysis provides a unique capability to monitor gradual reconstruction dynamics that are not detectable using bi-temporal imagery. Importantly, the proposed approach offers a scalable, operational

means of monitoring reconstruction progress across large regions, while also highlighting priority locations for targeted field investigations and post-disaster recovery planning.

(6) **How can RS-based observations support field investigations of post-earthquake building reconstruction at regional scales?**

The reconstruction monitoring methodology developed in this thesis demonstrated that RS-based observations can effectively support and guide on-site investigations by providing spatially explicit, regional-scale information on reconstruction progress. Time-series MT-InSAR analysis enables the identification of neighbourhoods and individual buildings undergoing significant change, allowing field teams to prioritise locations requiring detailed inspection. These locations can be exported as georeferenced datasets and imported into investigators' mobile devices, enabling direct navigation to targeted sites during field surveys.

By narrowing the focus of on-site investigations to areas flagged through RS analysis, the proposed approach reduces the time, cost, and logistical effort associated with large-scale post-earthquake surveys. This integration of RS–based screening with targeted, location-guided field verification enhances the efficiency and effectiveness of reconstruction monitoring, particularly in regions with limited access or constrained resources.

5.2. FUTURE RESEARCH

This thesis advances RS–based post-earthquake damage and reconstruction assessment by developing complementary, phase-specific methodologies. At the same time, these contributions demonstrate strong potential for regional-scale analysis; several conceptual and methodological limitations remain, opening directions for future research.

The displacement-based methodologies developed using LiDAR and InSAR provide physically interpretable indicators of structural response, yet they currently treat observed displacements primarily as empirical measures. The internal structural mechanisms linking these displacements to material degradation and the progression of failure remain implicit. Future research could bridge this gap by coupling RS-derived displacement indicators with numerical or analytical structural models, such as finite-element simulations or fragility-based approaches. Such integration would require more detailed building information than is considered in the present thesis, including the structural system and geometry, material properties, and structural detailing, as well as information on strengthening or retrofit interventions, where applicable. This would enable a deeper understanding of the mechanical processes underlying observed damage and support translation of observed deformation into physics-based performance metrics.

Another important direction for future research is to systematically investigate the minimum data requirements for operational implementation of the proposed methodologies across the different post-earthquake assessment phases. This should include determining the extent to which assessments can be performed using remotely sensed observations alone, which complementary building- and site-related information is essential, and how these requirements vary between short-term damage assessment and long-term reconstruction monitoring. The automatic derivation of required building information, such as building geometry and structural typology, from remotely sensed observations or existing geospatial datasets should also be investigated. Reducing reliance on manually

collected building inventories could improve the scalability and transferability of the proposed methodologies in regions where detailed building information is unavailable. Such analyses would help define the appropriate balance between remotely sensed observations, existing ancillary datasets, and field investigations across the post-earthquake assessment timeline.

Although the methodologies presented in this thesis address different phases of the post-earthquake timeline, they currently operate as analytically independent components, with their connection conceptual rather than operational. An important direction for future research is the development of temporal continuity across LiDAR- or InSAR-, and MT-InSAR-derived indicators, enabling consistent tracking of building and urban evolution over time. Establishing links between short-term damage indicators and long-term reconstruction signatures would allow assessment of recovery trajectories across multiple temporal phases, while preserving the methodological independence of the individual approaches. Future work should explore long-term, event-centred studies. Applying the full methodology to a single earthquake, from early post-event damage assessment using LiDAR or InSAR to later reconstruction analysis using MT-InSAR, would enable direct comparison of damage and reconstruction over time. This approach would allow direct verification of damage-to-reconstruction transitions and provide insight into how early damage states influence subsequent reconstruction outcomes.

While the thesis focuses on the physical aspects of damage and reconstruction, recovery outcomes are strongly influenced by social, economic, and institutional factors. Integrating socioeconomic data, such as population displacement, recovery funding, or building permits, with RS-derived indicators represents a critical direction for future research. This integration would enable a more holistic assessment of recovery and resilience, linking physical reconstruction to social equity and long-term sustainability.

Overall, this thesis contributes to a deeper scientific understanding of post-earthquake building behaviour and provides practical tools to support data-driven disaster response and recovery planning. By leveraging RS, situational awareness and building damage identification can be achieved in the short-term response phase, facilitating the assessment of impacts and the prioritisation of response actions, as well as identifying severely affected areas and buildings where reconstruction is not progressing well. This information can assist decision-makers in monitoring recovery dynamics and allocating resources more effectively. In addition, the proposed methodologies provide actionable guidance for targeted field inspections by helping field teams prioritise and plan on-site observations, both shortly after an event for damage verification and during later stages for monitoring reconstruction activities. site observations, both shortly after an event for damage verification and during later stages for monitoring reconstruction activities.

A

SUPPLEMENTARY MATERIAL

A.1. SUPPLEMENTARY MATERIAL FOR CHAPTER 3

See Figures A.1, A.2, A.3, A.4.

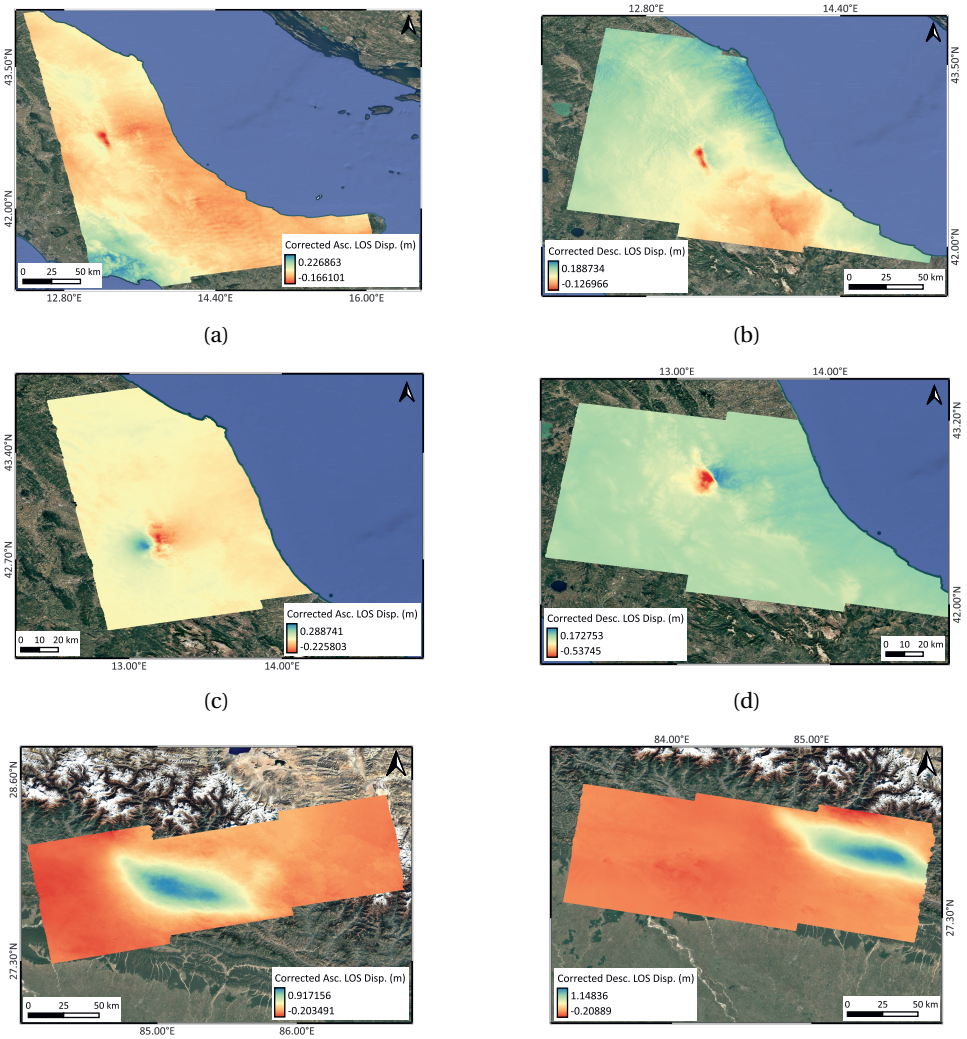

Figure A.1.: LOS Displacement maps derived from InSAR processing using the GAMMA software within the ASF platform [1], after atmospheric correction. Panels (a) and (b) correspond to the Amatrice event, (c) and (d) to the Norcia event, and (e) and (f) to the Nepal earthquake. For each region, ascending and descending tracks are shown in the left and right columns, respectively.

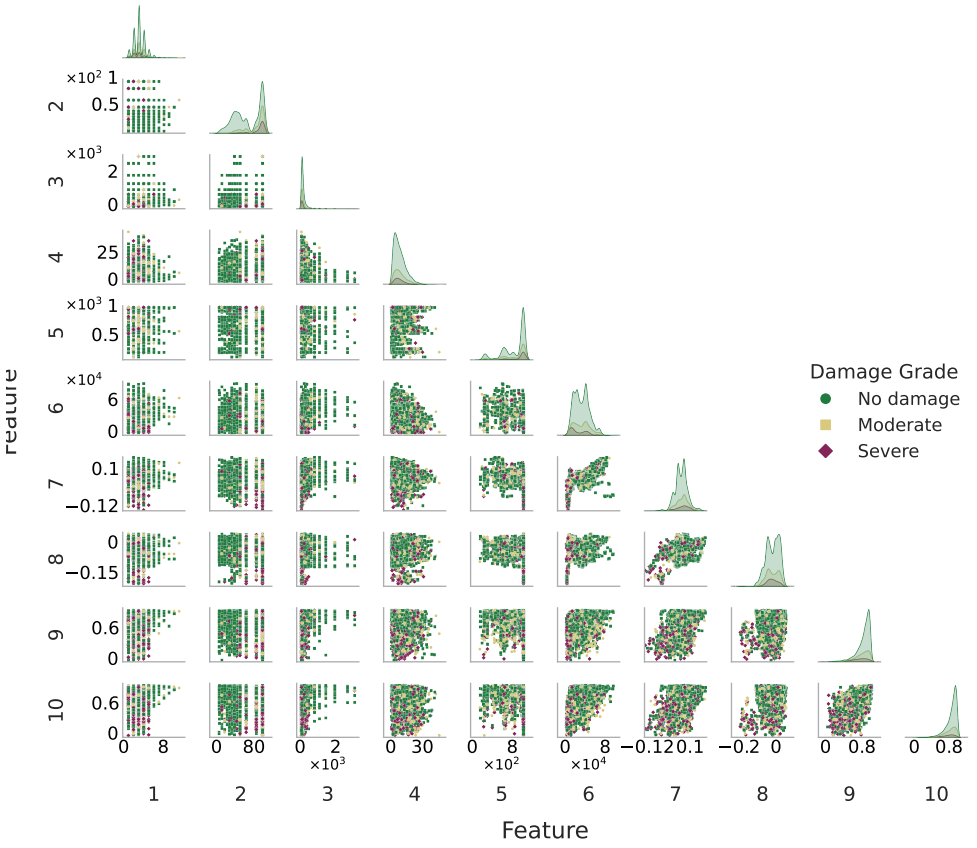

Figure A.2.: Pairwise relationships among key structural, site, and InSAR-derived features for the Amatrice dataset. Diagonal panels show the distribution of each individual feature, while off-diagonal panels show the pairwise relationships between features. Each panel is colour-coded by building damage level (No damage, Moderate, Severe). The numerical labels on the axes correspond to the following features: 1– Number of storeys, 2– Age, 3– Floor surface, 4– Slope, 5– Vs30, 6– Distance to the epicentre, 7– LOS descending, 8– LOS ascending, 9– Coherence descending, 10– Coherence ascending.

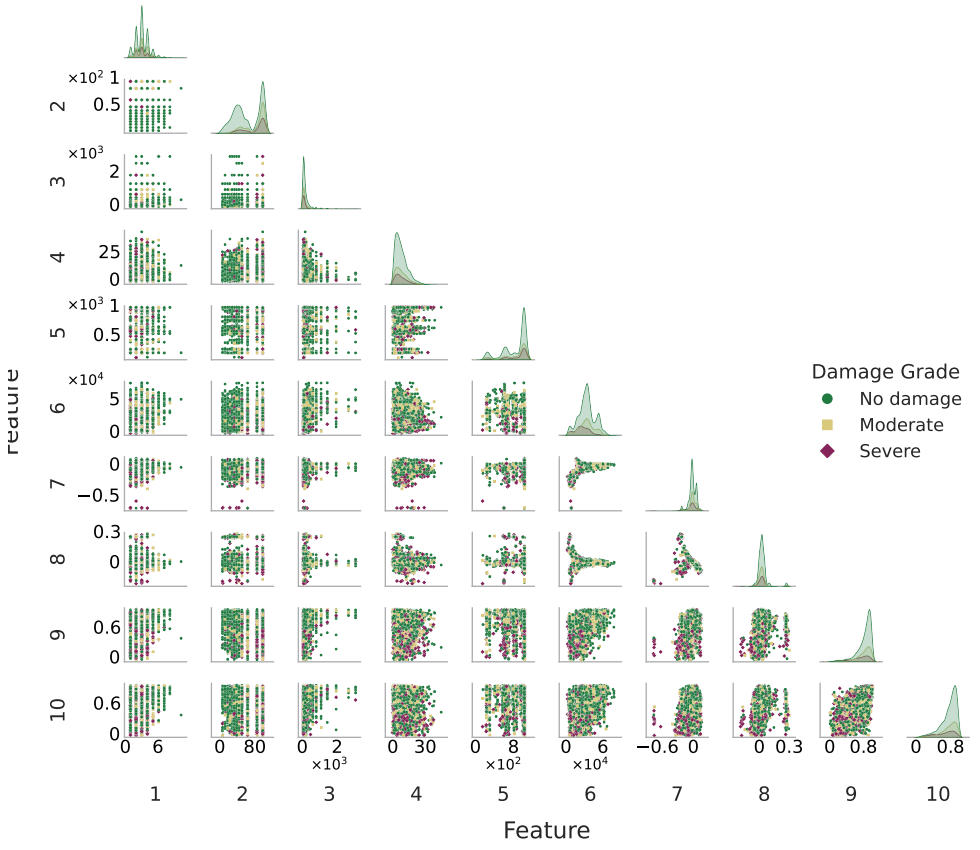

Figure A.3.: Pairwise relationships among key structural, site, and InSAR-derived features for the Norcia dataset. Diagonal panels show the distribution of each individual feature, while off-diagonal panels show the pairwise relationships between features. Each panel is colour-coded by building damage level (No damage, Moderate, Severe). The numerical labels on the axes correspond to the following features: 1– Number of storeys, 2– Age, 3– Floor surface, 4– Slope, 5– Vs30, 6– Distance to the epicentre, 7– LOS descending, 8– LOS ascending, 9– Coherence descending, 10– Coherence ascending.

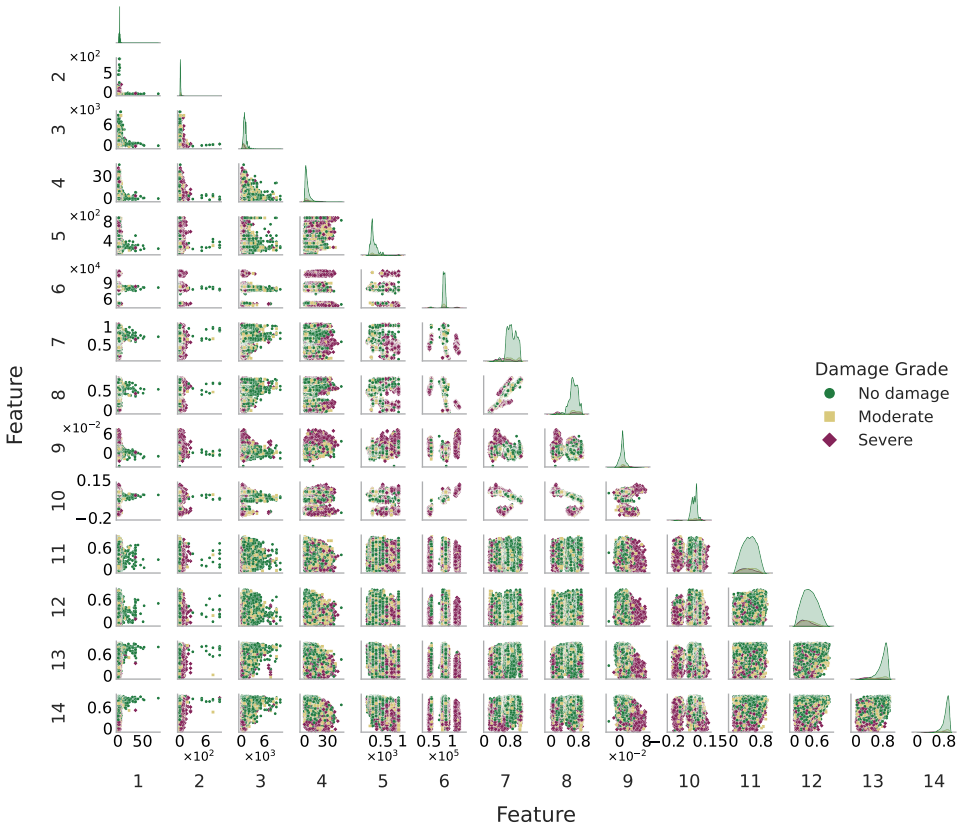

Figure A.4.: Pairwise relationships among key structural, site, and InSAR-derived features for the Nepal dataset. Diagonal panels show the distribution of each individual feature, while off-diagonal panels show the pairwise relationships between features. Each panel is colour-coded by building damage level (No damage, Moderate, Severe). The numerical labels on the axes correspond to the following features: 1– Number of storeys, 2– Age, 3– Floor surface, 4– Slope, 5– Vs30, 6– Distance to the epicentre, 7– Main-shock LOS descending, 8– Main-shock LOS ascending, 9- After-shock LOS descending, 10- After-shock LOS ascending 11– Main-shock coherence descending, 12– Main-shock coherence ascending, 13– After-shock coherence descending, 14– After-shock coherence ascending.

A.2. SUPPLEMENTARY MATERIAL FOR CHAPTER 4

See Figures A.5, A.6, and Tables A.1, A.2.

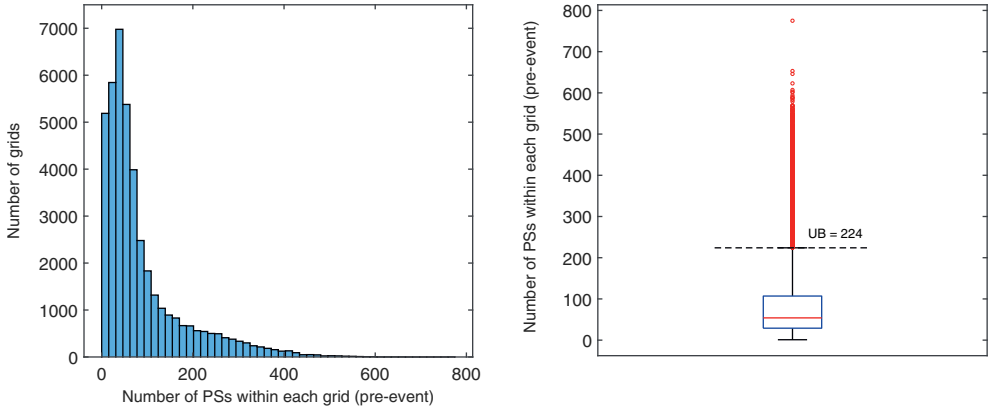

(a) (b)

Figure A.5.: Number of PSs per grid cell based on pre-event data: (a) histogram showing the frequency distribution and (b) box plot showing the variability of PS numbers (pre-event time series) per grid cell. The upper bound of the number of PSs (pre-event time series) used for grid-level analysis is 224.

Table A.1.: Upper bound values of building area distributions for each pair, used in the building-level analysis.

Pairs	$UB\,(area_{\mathrm{bu}})$
Pair 1	172
Pair 2	186.5
Pair 3	184

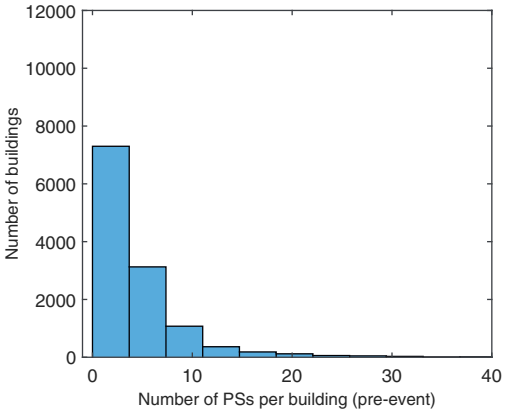

(a) Pre-event

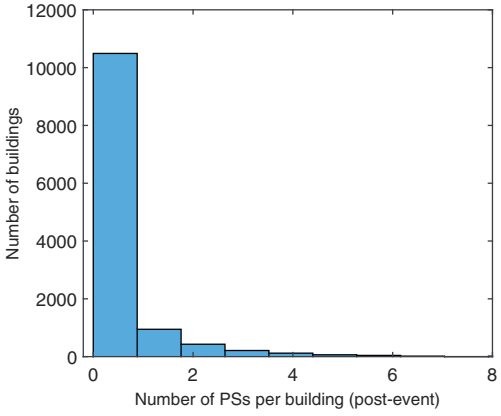

(b) Post-event

Figure A.6.: Number of PSs per building footprint from the (a) pre-event and (b) post-event data (Post 3).

Table A.2.: Number of buildings with over 50% change used for validation, categorised by pair and regions of interest.

Pairs	Kathmandu	Bhaktapur
Pair 1	1325	277
Pair 2	1186	323
Pair 3	2310	483

Table A.3.: Perpendicular and temporal baselines with Doppler Centroid (DC) differences for the time series of Post 2.

Date (yyyy-mm-dd)	Perpendicular Baseline (m)	Temporal Baseline (days)	DC (Hz/PRF)
2015-05-15	-163.999841	91.256504	-0.088485
2015-05-19	-159.999831	58.357024	0.105961
2015-05-27	-151.999865	614.610937	0.113940
2015-06-04	-143.999851	-196.962032	0.104766
2015-06-20	-127.999869	-325.837476	0.097149
2015-07-06	-111.999926	486.776836	0.140111
2015-07-14	-103.999943	264.811148	0.092809
2015-07-18	-99.999979	1192.506395	-0.045642
2015-07-22	-95.999926	-123.844859	0.110280
2015-07-30	-87.999966	467.612367	0.119710
2015-08-03	-83.999945	-534.329165	-0.074591
2015-08-07	-79.999975	1109.278368	0.136659
2015-08-15	-71.999961	-221.292560	0.087761
2015-08-19	-67.999988	623.834242	-0.059247
2015-08-23	-63.999964	389.072153	0.143078
2015-09-04	-51.999982	188.979467	-0.072350
2015-10-26	0.000000	0.000000	0.050749
2015-12-29	63.999856	907.377859	0.127257
2016-03-02	127.999720	-80.828071	0.110878
2016-03-10	135.999689	48.072930	0.137601
2016-03-14	139.999700	-495.239130	-0.072549
2016-03-18	143.999674	-125.467680	0.102930
2016-03-26	151.999649	-456.710045	0.115239
2016-03-30	155.999628	87.576926	-0.044917
2016-04-11	167.999586	-148.616509	0.142271
2016-04-15	171.999568	165.720698	-0.043453
2016-04-19	175.999542	548.992779	0.105197
2016-04-27	183.999523	-158.426957	0.141159
2016-05-05	191.999515	-757.475284	0.121716
2016-05-13	199.999446	76.252961	0.101724
2016-05-17	203.999461	-919.418826	-0.057127
2016-05-21	207.999421	-168.595003	0.078637
2016-05-29	215.999390	-660.762455	0.115580

ACKNOWLEDGEMENTS

Reaching this point has been a journey of growth, perseverance, and countless emotions. My PhD at TU Delft has been more than an academic pursuit; it has been a deeply personal experience, a story of distance, discovery, and the incredible people who stood beside me every step of the way.

Being away from my family, especially during difficult times, taught me the strength of solitude. Yet, in that distance, I found another kind of home, among kind people, in a culture that welcomed me, and in experiences that taught me independence, patience, and resilience. I will always carry a piece of the Netherlands with me, even if I never quite got used to its weather.

First and foremost, my deepest gratitude goes to **Dr. Giorgia Giardina**. Giorgia, you have been far more than a supervisor; you have been my mentor and often my closest friend in times when I needed one most. I will never forget the day you came to my home and stayed by my side through my illness and surgery. In that moment, it felt like I had my mother close to me again. Your kindness, care, and calm presence have carried me through the hardest parts of this journey. I learned from you not only how to think and write like a researcher, but also how to lead and support others with empathy and humanity. You helped me grow personally, shaping my confidence, my approach to challenges, and even aspects of myself that I was unsure how to develop. I will always be grateful for our walks, our long discussions, the many meetings we shared, and the countless moments spent brainstorming and reflecting on the work. Those conversations guided the direction of this thesis and helped me grow both academically and personally.

My heartfelt thanks also go to **Dr. Valentina Macchiarulo**, who has been both a colleague and a friend from the very beginning. Valentina, I have learned so much from your intelligence, your clarity, and your creativity. You have supported me in both the scientific and personal sides of this journey. Your office door was always open for me to stop by, interrupt you with my questions and doubts, and you were always welcoming, ready to share your thoughts and ideas. I will never forget our meetings, which were always full of brainstorming, laughter, and problem-solving. And, of course, I will always laugh when I remember NAC 2023, my first conference presentation, which almost turned into a comedy show of chaos right before my talk, until we somehow managed to fix everything together just in time! Thank you for being there, for your patience, and for sharing this journey with me.

I would also like to thank my promotor, **Prof. Kenneth Gavin**, for his official guidance and trust in my work throughout this project.

My gratitude extends to my collaborators and co-authors: **Dr. Pietro Milillo**, who was involved in some of the data processing that shaped important parts of my research, and also to **Dr. Kenneth Hudnut**, who generously provided additional essential data for my research, **Dr. Michael Whitworth**, whom I met during the EEFIT missions and who kindly

hosted me in London, and **Prof. Matthew DeJong** from Berkeley, whose expertise and collaboration on the project in Napa added depth to my project. I feel fortunate to have learned from such dedicated and talented scientists.

To my colleagues and friends in the department, **Murat**, **Hao**, **Dominika**, **Jan**, **Rafael**, and **Mauritz**, who made every lab meeting a moment of exchange, learning, and laughter. **Mauritz**, I especially want to thank you for the time we spent working together on your master's thesis. Being part of your supervisory team was a joy. We learned from each other, challenged ideas together, and had both fun and growth in the process.

Beyond the lab, I was lucky to find wonderful friends who made the Netherlands feel like home, **Yasamin**, **Pouriya**, **Anastasia**, **Amir**, **Tina**, **Aydin**, **Sarah**, **Elham**, **Safa**, **Yoosof**, **Parnian**, and **Nasim**. Thank you for your companionship, for the moments we shared, and for standing beside me when I needed it most. **Amir**, you have truly been like a brother to me.

To my dearest friend, **Sahar**, distance has never defined our friendship. Since our first days together at KNTU, your care and presence have remained constant, even across oceans. Your messages and calls reminded me that no matter how far we are, real friendship never fades.

To my partner, **Morteza**, thank you for being my calm in the storm. You joined me in the final, most demanding stage of this journey and filled my life with warmth and balance again. You never failed to make me smile, even on the hardest days, and your belief in me has been one of my greatest sources of strength.

And above all, my deepest and most heartfelt gratitude goes to my family, who are the roots of everything I am and everything I will ever be. To **Maman**, the legend of strength, whose WhatsApp message still greets me every morning and gives me energy to start the day. You have been the heartbeat of my life, the person who gave me courage when I doubted myself and comfort when I was far from home. Your love has crossed every distance, every silence, every day I was not there. To **Baba**, the legend of patience, whose quiet support has carried me through every challenge. You have always believed in me, pushed me forward, and given me the confidence to dream beyond what I thought possible. Without your sacrifices, none of this would have been real. To my brother, **Mahyar**, and sister-in-law, **Atefeh**, thank you for your constant love and for being there for me from afar.

This thesis belongs to all of you as much as it belongs to me. Every step, every page, every success carries your love within it.

Dedicated to my family, the true meaning of love and sacrifice.

List of Publications

16. **F. Foroughnia**, V. Macchiarulo and G. Giardina. 'Multi-level earthquake damage assessment using InSAR-derived displacement'. In: *International Journal of Disaster Risk Reduction* (2026), p. 106333. DOI: 10.1016/j.ijdrr.2026.106333

15. **F. Foroughnia**, V. Macchiarulo, P. Milillo, M. R. Whitworth, K. Gavin and G. Giardina. 'InSAR-based assessment of post-earthquake building reconstruction: The Nepal case study'. In: *International Journal of Applied Earth Observation and Geoinformation* 144 (2025), p. 104883. DOI: 10.1016/j.jag.2025.104883

14. **F. Foroughnia**, V. Macchiarulo, L. Berg, M. DeJong, P. Milillo, K. W. Hudnut, K. Gavin and G. Giardina. 'Quantitative assessment of earthquake-induced building damage at regional scale using LiDAR data'. In: *International Journal of Disaster Risk Reduction* 106 (2024), p. 104403. DOI: 10.1016/j.ijdrr.2024.104403

13. G. Giardina, V. Macchiarulo**, F. Foroughnia**, J. N. Jones, M. R. Whitworth, B. Voelker, P. Milillo, C. Penney, K. Adams and T. Kijewski-Correa. 'Combining remote sensing techniques and field surveys for post-earthquake reconnaissance missions'. In: *Bulletin of Earthquake Engineering* (2023), pp. 1–25. DOI: 10.1007/s10518-023-01716-9

12. **F. Foroughnia**, V. Macchiarulo, L. Berg, M. DeJong, P. Milillo, K. W. Hudnut, K. Gavin and G. Giardina. 'Rapid assessment of earthquake-induced building damage using remote sensing LiDAR data'. In: *EGU General Assembly Conference Abstracts*. 2023, EGU–3464

11. V. Macchiarulo**, F. Foroughnia**, P. Milillo, M. R. Whitworth, C. Penney, K. Adams, T. Kijewski-Correa and G. Giardina. 'City-scale damage assessment using very-high-resolution SAR satellite imagery and building survey data for the 2021 Haiti earthquake'. In: *SECED 2023 Conference-Earthquake Engineering and Dynamics for a Sustainable Future*. 2023

10. S. Mehravar, S. V. Razavi-Termeh, A. Moghimi, B. Ranjgar**, F. Foroughnia** and M. Amani. 'Flood susceptibility mapping using multi-temporal SAR imagery and novel integration of nature-inspired algorithms into support vector regression'. In: *Journal of Hydrology* 617 (2023), p. 129100. DOI: 10.1016/j.jhydrol.2023.129100

9. M. R. Whitworth, G. Giardina, C. Penney, L. Di Sarno, K. Adams, T. Kijewski-Correa, J. Black**, F. Foroughnia**, V. Macchiarulo, P. Milillo *et al.* 'Lessons for remote post-earthquake reconnaissance from the 14 August 2021 Haiti earthquake'. In: *Frontiers in Built Environment* (2022), p. 53. DOI: 10.3389/fbuil.2022.873212

8. M. Whitworth, G. Giardina, C. Penney, L. Di Sarno, K. Adams, T. Kijewski-Correa, J. Macabuag**, F. Foroughnia**, V. Macchiarulo, M. Ojaghi *et al.* 'Remote reconnaissance mission to the 14th August 2021 Haiti earthquake; remote sensing and building damage assessments'. In: *EGU General Assembly Conference Abstracts*. 2022, EGU22–10192

7. **F. Foroughnia**, S. M. Alfieri, M. Menenti and R. Lindenbergh. 'Evaluation of SAR and optical data for flood delineation using supervised and unsupervised classification'. In: *Remote Sensing* 14.15 (2022), p. 3718. DOI: 10.3390/rs14153718

6. F. Tarighat**, F. Foroughnia** and D. Perissin. 'Monitoring of power towers' movement using persistent scatterer SAR interferometry in south southwest of Tehran'. In: *Remote Sensing* 13.3 (2021), p. 407. DOI: 10.3390/rs13030407

5. B. Ranjgar, S. V. Razavi-Termeh**, F. Foroughnia**, A. Sadeghi-Niaraki and D. Perissin. 'Land subsidence susceptibility mapping using persistent scatterer SAR interferometry technique and optimized hybrid machine learning algorithms'. In: *Remote Sensing* 13.7 (2021), p. 1326. DOI: 10.3390/rs13071326

4. M. Amani, V. Poncos, B. Brisco**, F. Foroughnia**, E. R. DeLancey and S. Ranjbar. 'InSAR coherence analysis for wetlands in Alberta, Canada using time-series Sentinel-1 data'. In: *Remote Sensing* 13.16 (2021), p. 3315. DOI: 10.3390/rs13163315

3. S. M. Alfieri**, F. Foroughnia**, A. Van Natijne, A. Mousivand, R. Lindenbergh, F. Porcu, T. Zieher, B. Pulvirulenti, J. Yang and M. Menenti. 'Documenting impacts of hydro-meteorological events using Earth Observation'. In: *2021 IEEE International Geoscience and Remote Sensing Symposium IGARSS*. IEEE. 2021, pp. 934–937

2. S. M. Alfieri**, F. Foroughnia**, B. Pulvirenti, P. Ruggieri, M. Aguzzi, R. Linderberg, N. De Nigris, M. Morelli, F. Tavaroli, S. Unguentoli *et al.* 'Supporting co-development phase of nature-based solution by combined use of Earth Observation and modeling'. In: *EGU General Assembly Conference Abstracts*. 2021, EGU21–14269

1. **F. Foroughnia**, S. Nemati, Y. Maghsoudi and D. Perissin. 'An iterative PS-InSAR method for the analysis of large spatio-temporal baseline data stacks for land subsidence estimation'. In: *International Journal of Applied Earth Observation and Geoinformation* 74 (2019), pp. 248–258. DOI: 10.1016/j.jag.2018.09.018

CURRICULUM VITÆ

Fatemeh FOROUGHNIA

2011–2015	B.Sc. in Geomatics Engineering K.N.Toosi University of Technology, Tehran, Iran
2015–2018	M.Sc. in Remote Sensing K.N.Toosi University of Technology, Tehran, Iran *Thesis:* PS-InSAR Time Series Analysis using ENVISAT-ASAR and Sentinel-1 Data Stacks for Subsidence Estimation *Supervisor:* Dr. Y. Maghsoudi Mehrani
2020–2021	Researcher in Remote Sensing Delft University of Technology, Delft, The Netherlands
2021–2025	Ph.D. Candidate in Geoscience and Engineering Delft University of Technology, Delft, The Netherlands *Thesis:* Post-Earthquake Assessments of Building Damage and Reconstruction Using Remote Sensing *Promotor:* Dr. G. Giardina *Promotor:* Prof. dr. K.G. Gavin
2025–Present	Data Scientist Satelligence, Utrecht, The Netherlands


TUDelft